



Kirmanj AZIZ, MSc

**Surface Tension Measurements of Liquid Metals and Alloys  
by Oscillating Drop Technique in combination with an  
Electromagnetic Levitation Device**

**DOCTORAL THESIS**

to achieve the university degree of  
Doktor der technischen Wissenschaften

submitted to

**Graz University of Technology**

Supervisor

Ao.Univ.-Prof. Dipl-Ing. Dr.techn. Gernot Pottlacher

Institute of Experimental Physics

## **AFFIDAVIT**

I declare that I have authored this thesis independently, that I have not used other than the declared sources/resources, and that I have explicitly indicated all material which has been quoted either literally or by content from the sources used. The text document uploaded to TUGRAZonline is identical to the present doctoral thesis.

---

Date

---

Signature

## Abstract

From a scientific as well as a technological standpoint, surface tension and its temperature dependence is a matter of particular interest. The temperature gradient of surface tension is the driving force for the Marangoni flow and an important quantity for wetting phenomena and for casting and welding processes as well.

As existing models for the calculation of surface tension are very limited and not generally valid, an experimental determination of this quantity is necessary. The accurate measurement of surface tension is not simple, since surface tension is determined by the microscopic structure of the surface and therefore is very sensitive to impurities. Furthermore, liquid metals at high temperatures are very reactive, which makes accurate measurements even more difficult.

In this work, the surface tension of liquid metals and alloys is measured by an oscillating drop technique combined with electromagnetic levitation [1–5]. Metallic materials are levitated inside a levitation coil by means of an inhomogeneous radio frequency electromagnetic field. Ohmic losses of eddy currents heat up the specimen into the liquid phase. The molten sample rotates and oscillates around the equilibrium shape. The oscillations used for the surface tension measurement are recorded by a high-speed camera at 600 fps. The specimens' temperature is measured by a fast near-infrared pyrometer.

The electromagnetic levitation setup provides both a container-less as well as a contact-free measurement. Hence contamination of specimen during measurement is dramatically reduced. Furthermore, undercooled liquid metals and alloys can be investigated as well.

## Zusammenfassung

Die Oberflächenspannung und ihre Temperaturabhängigkeit ist sowohl in der Wissenschaft als auch in der Industrie von großer Bedeutung. Der Temperaturgradient ist die Ursache für die Marangoni Strömung und spielt eine wichtige Rolle bei Gieß- und Schweißprozessen sowie bei Benetzungspänomenen.

Die vorhandenen Modelle für die Berechnung der Oberflächenspannung besitzen nur sehr eingeschränkt Gültigkeit, weshalb die experimentelle Bestimmung dieser Größe umso wichtiger ist. Die Tatsache, dass die Oberflächenspannung von der Mikrostruktur der Oberfläche bestimmt wird, macht die Messung sehr empfindlich gegenüber kleinste Verschmutzungen. Darüber hinaus sind flüssige Metalle bei hohen Temperaturen sehr reaktiv, was die genaue Bestimmung der Oberflächenspannung weiter erschwert.

In dieser Arbeit wird die Oberflächenspannung von flüssigen Metallen und Legierungen mittels der Oszillierender-Tropfen-Technik in Kombination mit einer elektromagnetischen Levitationsapparatur bestimmt [1–5]. Innerhalb einer eigens entworfenen Spule wird ein hochfrequentes, inhomogenes elektromagnetisches Wechselfeld erzeugt, womit leitende Materialien in der Schwebe gehalten und gleichzeitig erhitzt und aufgeschmolzen werden. Damit wird ein berührungsloses Messungsverfahren gewährleistet. Die Oszillationen werden mittels einer Hochgeschwindigkeitskamera mit 600 fps aufgezeichnet. Die Messung der Probestemperatur erfolgt mit Hilfe eines schnellen Nahinfrarot-Pyrometers.

Die elektromagnetische Levitationsapparatur bietet eine berührungslose Messmethode, wodurch die Kontamination der flüssigen Probe dramatisch gesenkt werden kann. Ferner ist mit diesem Messverfahren die Untersuchung von unterkühlten Metallen und Legierungen auch möglich.

---

# Contents

---

<b>Preface</b>	<b>1</b>
<b>1 Introduction</b>	<b>2</b>
1.1 Surface tension measurement techniques for liquid metals and alloys .	2
1.1.1 Drop shape technique . . . . .	2
1.1.2 Maximum bubble pressure technique . . . . .	4
1.1.3 Oscillating drop technique . . . . .	5
<b>2 Experimental</b>	<b>8</b>
2.1 Experimental setup . . . . .	9
2.1.1 Experimental chamber . . . . .	10
2.1.2 Radio frequency generator . . . . .	10
2.1.3 Vacuum pumps . . . . .	10
2.1.4 Pressure gauges . . . . .	11
2.1.5 Levitation coil . . . . .	11
2.1.6 Cooling system . . . . .	12
2.2 Experimental procedure . . . . .	13
2.2.1 Specimen preparation . . . . .	13
2.2.2 Atmosphere . . . . .	13
2.2.3 Electromagnetic levitation . . . . .	14
2.3 Measurement technique . . . . .	15
2.3.1 Hardware used for temperature and surface tension measure- ment . . . . .	15
2.3.1.1 Pyrometer . . . . .	15
2.3.1.2 Vision system . . . . .	16

2.3.2	Software used for temperature and surface tension measurement	18
2.3.2.1	Temperature measurement software	18
2.3.2.2	Surface tension measurement software	18
2.3.3	Temperature measurement	19
2.3.4	Determination of the oscillation frequencies	20
2.3.5	Specimen geometry	20
2.3.6	Assignment of the oscillation frequencies $\nu_{2,m}$	23
<b>3</b>	<b>Uncertainties</b>	<b>25</b>
3.1	Uncertainty due to oscillation frequencies, mass, density of the specimen	25
3.2	Uncertainty due to temperature	27
<b>4</b>	<b>Discussion</b>	<b>29</b>
4.1	Determination of surface tension	29
4.1.1	Determination of the specimens' mass	29
4.1.2	Determination of the oscillation frequencies $\nu_{2,m}$	31
4.2	Investigation of alloys	31
4.3	Alternative evaluation	32
4.4	Surface tension of nickel and its uncertainty	37
<b>5</b>	<b>Outlook</b>	<b>39</b>
5.1	Optimizations	39
5.2	Oxygen detection and manipulating	39
5.3	Emissivity measurement	40
<b>6</b>	<b>Publications</b>	<b>42</b>
6.1	Measurement of surface tension of Cu–5Sn by an oscillating drop technique	43
6.2	Measurement of surface tension of liquid nickel by the oscillating drop technique	52
6.3	Measurement of surface tension of liquid copper by means of electromagnetic levitation	60
6.4	Thermophysical characteristics of liquid metals and alloys at TU Graz: a status report	69
6.5	Investigation of liquid metallic elements and alloys by means of containerless techniques	88
	<b>Bibliography</b>	<b>95</b>
	<b>List of Figures</b>	<b>96</b>
	<b>List of Tables</b>	<b>97</b>

## Preface

This work is designed as a cumulative thesis, which means that the main scientific results are presented in the form they were published in peer-reviewed journals. The publications [1–5] are arranged in Chapter 6. Each paper is annotated with a detailed explanation concerning the content and the contribution of the authors.

Chapter 1 introduces the maximum bubble pressure technique, the drop shape technique, and the oscillating drop technique. These are common methods which allow to measure the surface tension of liquid metals and alloys.

In Chapter 2, the experimental setup which was built for this work is described in detail. Furthermore, the measuring procedure is discussed here as well.

Chapter 3 discusses the measurement uncertainties of surface tension associated with the oscillating drop technique.

Chapter 4 provides a detailed discussion on the results of the publications carried out in this work.

Last but not least, Chapter 5 gives an outlook suggesting future steps.

---

# 1 Introduction

---

## 1.1 Surface tension measurement techniques for liquid metals and alloys

Even if there are several methods to determine surface tension experimentally, such as capillary rise, drop weight, drop shape, Du Noüy ring, maximum bubble pressure, Wilhelmy plate, and oscillating drop method, only a few of them are suitable for accurate surface tension measurement of liquid metals at high temperatures. Liquid metals are very reactive and surface tension is very sensitive to impurities. In particular, the presence of surface active elements, such as oxygen, leads to contamination of the sample. In this chapter, a short introduction to the most common measurement techniques for the determination of surface tension of liquid metals and alloys will be given. The techniques which will be discussed are the maximum bubble pressure technique, the drop shape technique, and the oscillating drop technique.

### 1.1.1 Drop shape technique

The drop shape technique (Figure 1.1) includes the sessile drop [6, 7] and the pendant drop technique [8–11]. Even if the drop shape technique is not a container-less method, it is a popular procedure to determine surface tension.

The basic theory underlying this technique is the Young-Laplace equation Eq. (1.1), which describes the relationship between surface tension  $\gamma$ , pressure difference  $\Delta p$  across the interface, and the shape of the surface with radii of curvature  $r_1$  and  $r_2$ .

$$\Delta p = \gamma \left( \frac{1}{r_1} + \frac{1}{r_2} \right). \quad (1.1)$$

In the case of an aspherical droplet as can be found in the sessile drop and pendant

drop technique, the Young-Laplace equation can be expressed as [12]

$$\rho g z + C = \gamma \left( \frac{1}{r_1} + \frac{1}{r_2} \right), \quad (1.2)$$

where  $\rho$  is the density,  $g$  the gravitational acceleration, and  $z$  the vertical coordinate (Figure 1.1a).

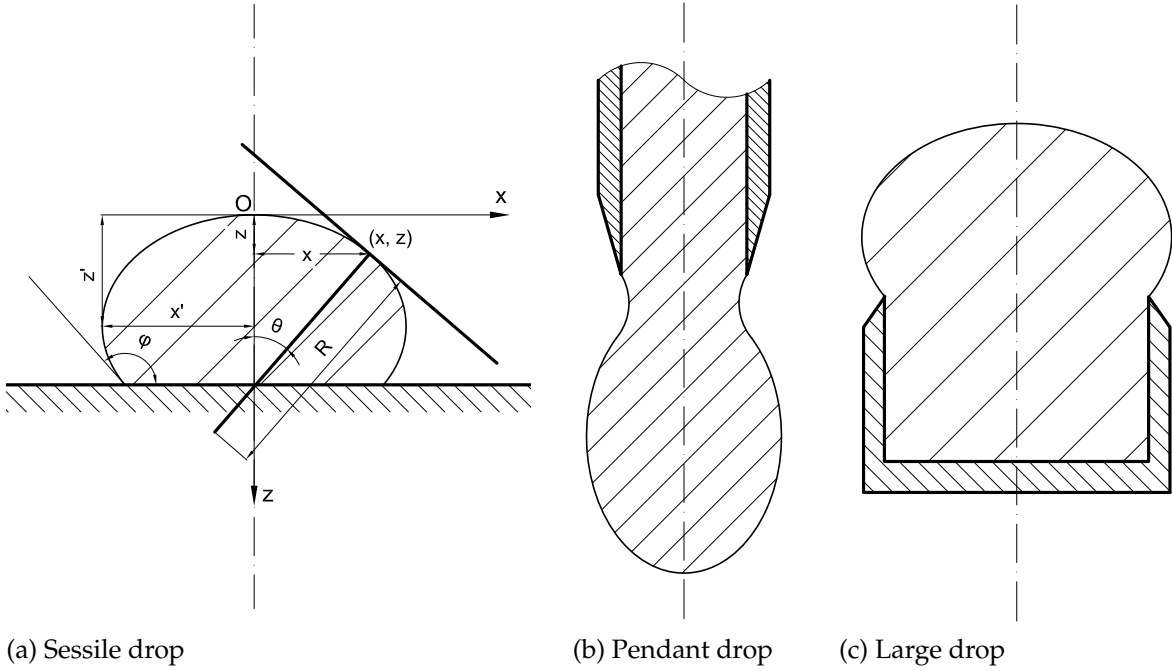


Figure 1.1: An illustration of a sessile drop (a), a pendant drop (b), and a large drop (c).

Assuming rotational symmetry around the  $z$ -axis, the two radii of curvature at the origin/apex ( $z = 0$ ) are equal ( $r_1 = r_2 := b$ ) and the constant  $C$  becomes

$$C = \frac{2\gamma}{b}. \quad (1.3)$$

With  $R$  being the meridional radius of curvature at the point  $\begin{pmatrix} x \\ y \end{pmatrix}$ , the radii of curvature are

$$r_1 = R, \quad (1.4a)$$

$$r_2 = \frac{x}{\sin\theta}. \quad (1.4b)$$

Therefore, Eq. (1.2) becomes

$$\frac{b}{R} + \frac{\sin\theta}{x} = 2 + \beta \frac{z}{b}, \quad (1.5)$$

with

$$\beta = \frac{\rho g b^2}{\gamma}. \quad (1.6)$$

By measuring the distances  $x'$  and  $z'$  (see Figure 1.1a),  $\beta$  can be determined from the tables provided by Bashforth and Adams [12] and the surface tension can be calculated from Eq. (1.6).

In order to obtain accurate results, it is important to ensure that no contamination of the specimen by the substrate occurs during the experiment, and a rotational symmetry around the  $z$ -axis is given. To achieve better results for wetting systems, the large drop technique (a variation of the sessile drop technique) is recommended (Figure 1.1c). Another advantage of the large drop technique is a better rotational symmetry of the specimen.

Recently, a new procedure was developed, which combines the pendant and sessile drop technique [13, 14]. The main advantages of this enhanced method are a short contact time and a better rotational symmetry, which allow to keep contamination low. As a result, this technique is extremely effective to investigate high reactive metals, such as titanium, at high temperatures up to 2400 K.

### 1.1.2 Maximum bubble pressure technique

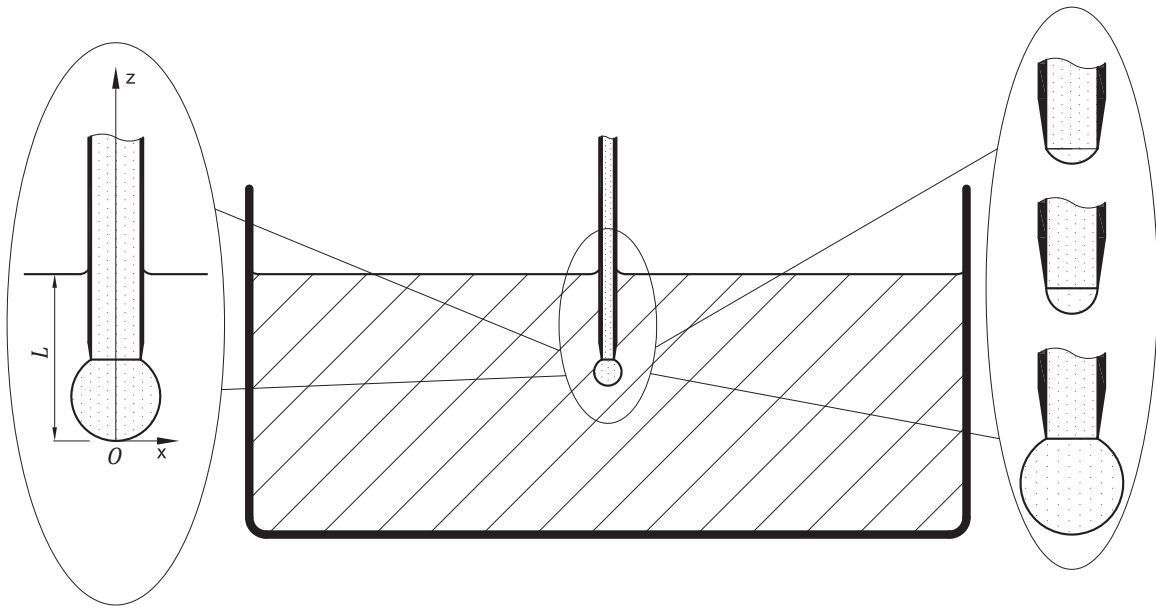


Figure 1.2: An illustration of the maximum bubble pressure technique.

Figure 1.2 illustrates the maximum bubble pressure technique. A capillary tube of known radius is immersed in the fluid used in the experiment. By increasing the gas pressure in the tube, a bubble is produced. The pressure inside the tube ( $p_t$ ) is the

sum of the pressures originating from surface forces ( $p_s$ ) and the hydrostatic pressure ( $p_h$ ):

$$p_t = p_s + p_h = (2\gamma)/b + \Delta\rho gL, \quad (1.7)$$

where  $\gamma$  is the surface tension,  $b$  is radius of curvature of the bubble at the Origin ( $O$ ),  $\Delta\rho$  is the density difference between the gas and the liquid,  $g$  is the gravitational force and  $L$  is the immersion depth of the tube including the bubble (Figure 1.2).

When the bubble becomes hemispherical, its radius is at a minimum and as a result, the pressure measured inside the tub is at a maximum. At this point, the radius of the bubble is equal to the radius  $r$  of the tube. Consequently, the radius of curvature  $b$  can be set equal to  $r$  in Eq. (1.7). As in the case of the sessile and pendant drop technique, surface tension can be determined using the tables provided by Bashforth and Adams.

A major advantage of the maximum bubble pressure technique is that a new bubble, and therefore a new uncontaminated surface is created for each measurement.

### 1.1.3 Oscillating drop technique

A more recent method to determine surface tension is the oscillating drop technique in combination with a levitation device, such as electromagnetic levitation, electrostatic levitation, microgravity levitation, aerodynamic levitation or acoustic levitation. During levitation of the specimen, oscillations around the equilibrium shape are observed in the liquid phase. Every distortion of the specimen can be described mathematically by the sum of the corresponding spherical harmonics. The radius  $R$  of the oscillating specimen is given by

$$R(\vartheta, \varphi, t) = \sum_l \sum_{m=-l}^{m=l} a_{l,m}(t) \cdot Y_l^m(\vartheta, \varphi), \quad (1.8)$$

where  $\vartheta$  and  $\varphi$  are the polar and azimuth angle,  $a_{l,m}$  is the time dependent amplitude of disturbance and  $Y_l^m$  is the real spherical harmonics defined by the associated Legendre polynomials [15]:

$$Y_l^m(\vartheta, \varphi) = P_l^m(\cos \vartheta) \cos(m\varphi), \quad \text{if } m \geq 0 \quad (1.9a)$$

$$Y_l^m(\vartheta, \varphi) = P_l^{-|m|}(\cos \vartheta) \sin(-|m|\varphi), \quad \text{if } m < 0 \quad (1.9b)$$

with  $l \geq 0$  and  $-l \leq m \leq l$ .

For small specimens as the ones used in levitation experiments, surface tension is the restoring force holding the specimen together and consequently the origin of the oscillations. Therefore, a relation between the oscillation frequencies and the surface tension is expected. This relation for non-rotating, spherical specimens was shown by Lord Rayleigh in 1879 [16]

$$v_l^2 = \frac{l(l+2)(l-1)}{3\pi} \frac{\gamma}{M}, \quad (1.10)$$

where  $\nu$  is the oscillation frequency,  $l$  is the index of the spherical harmonics,  $\gamma$  is the surface tension and  $M$  is the mass of the specimen. The oscillation frequency  $\nu_2$  is the fundamental frequency. It is known as Rayleigh frequency  $\nu_R$ . In this case, the surface tension for non-rotating, spherical specimens is determined by measuring the Rayleigh frequency and the mass of the specimen with the formula

$$\gamma = \frac{3}{8}\pi \cdot M \cdot \nu_R^2. \quad (1.11)$$

This formula is only valid for microgravity experiments performed in space or in reduced gravity aircraft. In the case of terrestrial levitation experiments, gravitational force acts on the specimen, leading to distortion of the otherwise spherical equilibrium shape. In general, the specimen rotates. As a consequence, the degenerated five-folded Rayleigh frequency  $\nu_R$  splits in up to five separate frequencies  $\nu_{2,0}$ ,  $\nu_{2,\pm 1}$  and  $\nu_{2,\pm 2}$ .

To achieve same results for terrestrial levitation experiments and for experiments in microgravity, the following correction [17] was suggested for the Rayleigh frequency by Cummings and Blackburn:

$$\nu_R^2 = \nu_2^2 - \nu_\tau^2 \left( 1.9 + 1.2 \frac{z_0^2}{R^2} \right), \quad (1.12)$$

with

$$z_0 = \frac{g}{2(2\pi\nu_\tau)^2}, \quad (1.13a)$$

$$\nu_\tau^2 = \frac{1}{3} \sum_{m=-1}^1 \nu_{1,m}^2, \quad (1.13b)$$

$$\nu_2^2 = \frac{1}{5} \sum_{m=-2}^2 \nu_{2,m}^2, \quad (1.13c)$$

where  $R$  is the radius of the specimen,  $g$  is the gravitational acceleration, and  $\nu_\tau^2$  is the mean translational squared frequency. The radius of the specimen is calculated from the samples' mass  $M$  and density  $\rho$ .

$$R = \sqrt[3]{\frac{3M}{4\pi\rho}}. \quad (1.14)$$

Substituting the Rayleigh frequency in Eq. (1.11) by the corrected frequency Eq. (1.12) yields to the surface tension formula for terrestrial experiments

$$\gamma = \frac{3}{8}\pi M \left( \nu_2^2 - \nu_\tau^2 \left( 1.9 + 1.2 \frac{z_0^2}{R^2} \right) \right). \quad (1.15)$$

By determining the mass  $M$ , the oscillation frequencies  $\nu_{1,m}$  and  $\nu_{2,m}$ , and the radius  $R$  of the specimen, the surface tension under terrestrial conditions can be calculated

---

from Eq. (1.15). The main advantage of the oscillating drop technique is that it can be used in combination with container-less levitation devices. In this way, the contamination of the specimen is kept to a minimum and surface tension of undercooled liquid metals can be investigated as well.

---

## 2 Experimental

---

The thermophysics and metalphysics group at Graz University of Technology has been investigating metals and alloys in the solid and liquid phase for the last thirty years. During this period, it was possible to determine several thermophysical properties with the present experimental facilities (pulse-heating,  $\mu$ s-DOAP, DSC, DTA, four-point-probe). A short overview is given in publication [4].

Unfortunately, we were not able to measure surface tension with the experimental facilities mentioned before. For this reason, we started to evaluate how to expand our measurement capabilities. As we were looking for a container-less method, we decided to setup an experiment based on the oscillating drop technique. An electromagnetic levitation setup was suitable for our project for several reasons. The major advantages of this device compared to other levitation devices are that every conducting material can be levitated, the experiment can be carried out both under barometric pressure and at high vacuum condition, and last but not least the simplicity and ease of use of the experimental setup.

Four years ago I started to build an electromagnetic levitation setup within the project P23838-N20 (founded by Austrian Science Fund (FWF)). A suitable experimental chamber (see chapter 2.1.1) and an up-to-date vision system (see chapter 2.3) was built from scratch within this project.

This additional experimental facility allows us not only to measure surface tension but also to determine density. The results have been published during the last few years [1–3, 18].

## 2.1 Experimental setup

Figure 2.1 shows the electromagnetic levitation setup built within this work at the institute of experimental physics (Graz University of Technology, NAWI Graz).

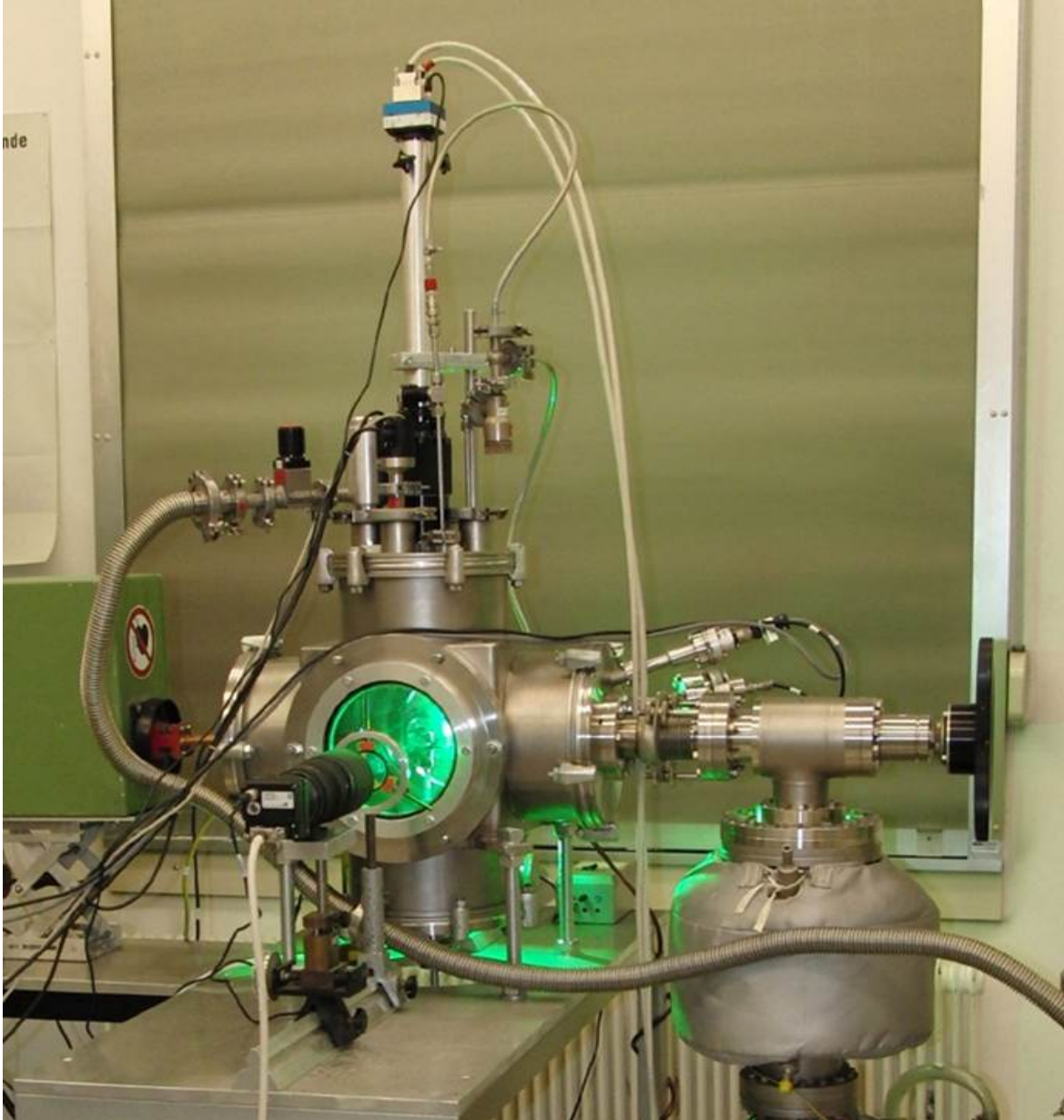


Figure 2.1: The electromagnetic levitation setup built within this work at Graz University of Technology, NAWI Graz.

An illustration of the setup is given in Figure 2.2. The main parts of the electromagnetic levitation experiment are a vision system, an experimental chamber, a self-designed levitation coil, and a radio frequency (high frequency) generator.

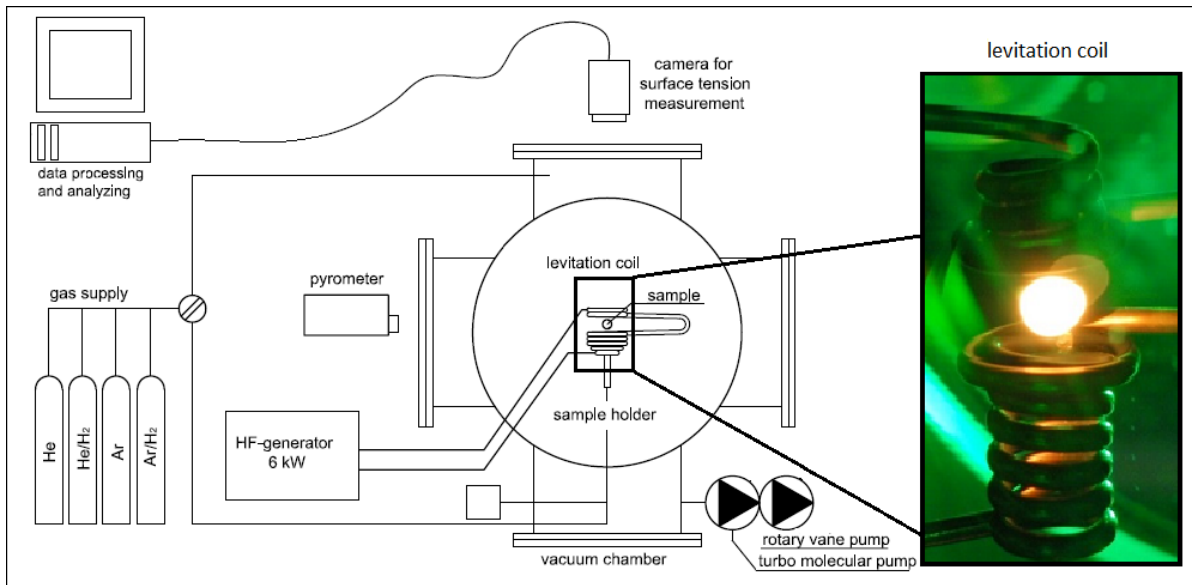


Figure 2.2: An illustration of the electromagnetic levitation setup. [3]

### 2.1.1 Experimental chamber

Basically, the experimental chamber is a specifically adapted vacuum chamber. Big optical windows are built in for the pyrometer and vision system (see chapter 2.3). More than ten vacuum flanges allow attaching vacuum pumps, gas and electrical supplies, pressure gauges, and a linear motion feedthrough.

### 2.1.2 Radio frequency generator

The radio frequency generator (*IG 5/200HY*, Trumpf Hüttinger GmbH + Co. KG, Freiburg, Germany) was used within this work. It has a power output of 6 kW and with our configuration it operates at a frequency of 400 kHz. An alternating electric current with  $I_{rms} = 350$  A flows through the levitation coil.

### 2.1.3 Vacuum pumps

A rotary vane pump (*Pfeiffer Balzers Duo 0016B*, Pfeiffer Vacuum GmbH, Asslar, Germany) and a turbomolecular pump (*Pfeiffer Balzers TPU 330*, Pfeiffer Vacuum GmbH, Asslar, Germany) are used to produce vacuum with a pressure of  $10^{-6}$  mbar inside the experimental chamber. First, the rotary vane pump produces a pressure below  $10^{-2}$  mbar. Then, the turbomolecular pump is turned on to reach a pressure of  $10^{-6}$  mbar. During the experiment, the turbomolecular pump is turned off and the experimental chamber is filled with inert gas to provide a clean atmosphere (see chapter 2.2.2) with a pressure between 750 mbar and 1500 mbar. At this point, the rotary vane pump is still turned on and is connected to the experimental chamber through a two-port solenoid valve. If the pressure inside the experimental chamber

is higher than the set pressure, the solenoid valve is opened and the pressure starts to decrease. When the set pressure is reached, the solenoid valve is closed again. In this way, the pressure is maintained constant.

### 2.1.4 Pressure gauges

Different pressure gauges are used to measure the complete pressure range from  $10^{-6}$  mbar to 2000 mbar. A pirani gauge (*Balzars TPR-016*, Pfeiffer Vacuum GmbH, Asslar, Germany) measures pressures in the range of  $10^{-4}$  mbar to 1 mbar. A penning cold cathode vacuum gauge (*Balzars IKR-020*, Pfeiffer Vacuum GmbH, Asslar, Germany) is used to measure pressures below  $10^{-4}$  mbar. The pressure gauge (*Leybold DI 2000*, Oerlikon Leybold Vacuum GmbH, Cologne, Germany) measures pressures between 1 and 2000 mbar, and is used to maintain the set pressure of the Atmosphere inside the experimental chamber.

### 2.1.5 Levitation coil

The levitation coil is located inside the experimental chamber. It is self-designed from a copper tube with an inner diameter of 1.5 mm and an outer diameter of 3 mm. The coil is water-cooled to prevent it from melting. The top part of the levitation coil is reverse wound to the bottom part and generates the enclosing electromagnetic field as shown in Figure 2.3.

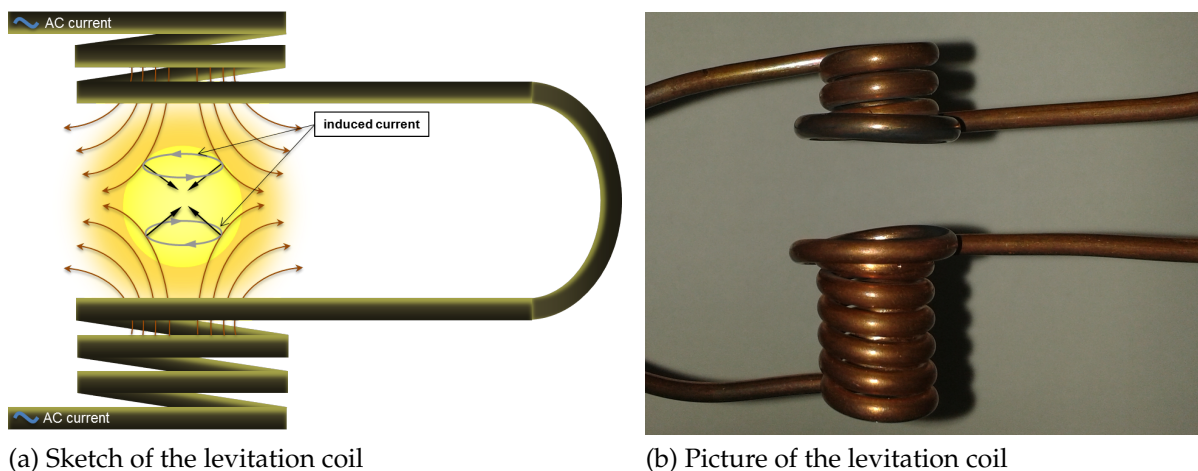


Figure 2.3: (a) shows a sketch of the levitation coil, the AC and induced eddy currents, and the magnetic field lines [1]. (b) shows the levitation coil used in our experiments.

Figure 2.4 shows a fabrication drawing of the levitation coil used in our experiments. First, the top- and bottom part of the levitation coil are wound separately around an iron rod with a diameter of 10 mm, as shown in Figure 2.4a. Then, the

top part is folded upon the bottom part to get the resulting levitation coil (see Figure 2.4b). The bottom part consists of seven loops whereas the top part consists of four loops.

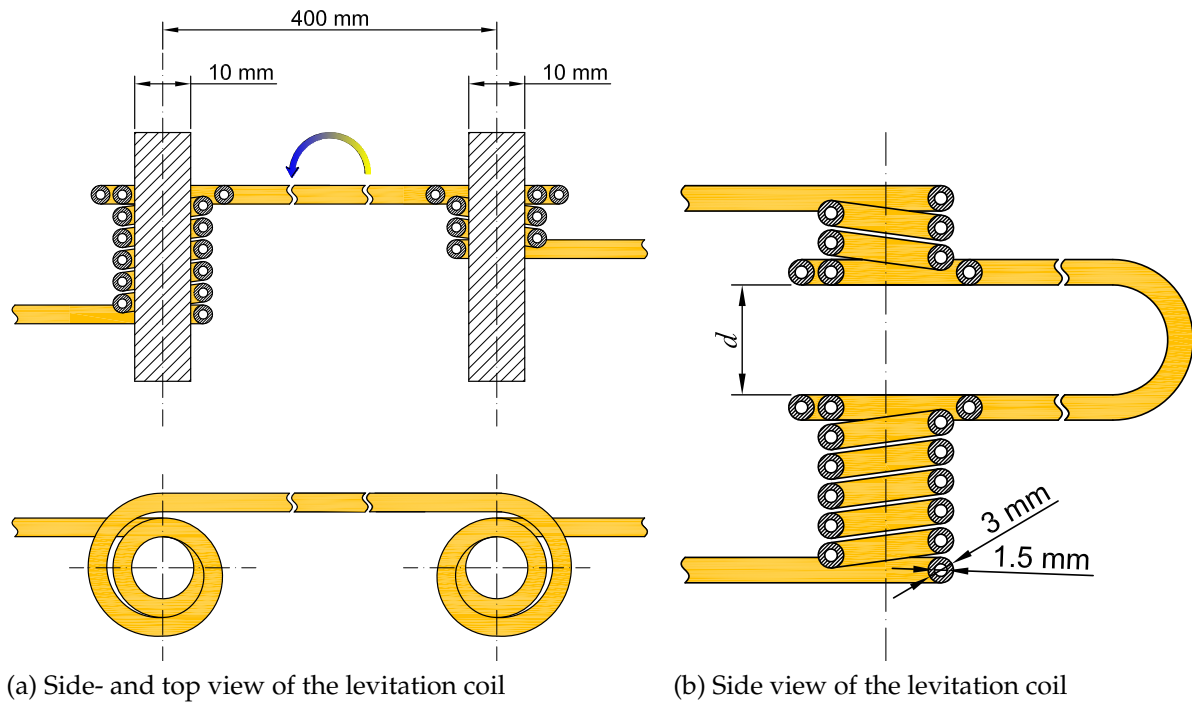


Figure 2.4: Fabrication drawing of the levitation coil used (Figure 2.3b). (a) shows the side- and top view of the levitation coil before it is folded. (b) shows the side view of the levitation coil after it is folded.

For each material, the levitation coil is adapted to levitate the specimen stably. Adaption means here to adjust the distance  $d$  between the top- and bottom part of the levitation coil. Reducing the distance  $d$  provides better heating of the specimen. On the other hand, the electromagnetic pressure exerted by the enclosing electromagnetic field increases and leads to higher deformation of the specimen. This may cause a less accurate measurement or even an useless measurement. An optimized levitation coil is essential for accurate measurements.

### 2.1.6 Cooling system

Both the radio frequency generator and the levitation coil are water-cooled. Whereas a cooling system (*Kühlmobil 141*, Van der Heijden-Labortechnik GmbH, Dörentrup, Germany) is used to cool down the radio frequency generator below  $20^{\circ}\text{C}$ , the levitation is cooled directly by tap water with a flow rate of  $0.8\text{ L min}^{-1}$ .

## 2.2 Experimental procedure

### 2.2.1 Specimen preparation

First of all, a specimen with the right size or weight. Depending on the material of the specimen and the dimensions of the levitation coil, there exists a certain size range for specimens to levitate stably.

Pure metals are order from *Alfa Aesar GmbH & Co KG* (Karlsruhe, Germany) and *Advent Research Materials Ltd* (Oxford, England). In the case of Cu-5Sn, the alloy was provided by *Österreichisches Gießerei-Institut* (Leoben, Austria).

Table 2.1: The purity of specimens measured in this work.

Material	Purity [%]	Manufacturer [ppmv]
Aluminium	99.999 %	<i>Advent Research Materials Ltd</i>
Copper	99.9999 %	<i>Alfa Aesar GmbH &amp; Co KG</i>
Nickel	99.995 %	<i>Alfa Aesar GmbH &amp; Co KG</i>
Cu-5Sn	Cu + 4.63 wt% Sn + 0.03 wt% Zn	<i>Österreichisches Gießerei-Institut</i>

Then surface of the specimen is cleaned with pure acetone in an ultrasonic bath. After cleaning, it is weighed and placed on the sample holder inside the vacuum chamber by using tweezers. The mass of the specimen is measured with a precision balance (*AB-104-S-A*, Mettler-Toledo GmbH, Gießen, Germany). The accuracy of the balance is 0.1 mg. The specimen is also weighed after the experiment to verify that no significant evaporation occurred.

### 2.2.2 Atmosphere

Before starting the levitation experiment, the vacuum chamber is evacuated to  $10^{-6}$  mbar and subsequently filled with inert gas such as helium, argon, ARCAL 10, and/or a custom gas mixture to provide a clean environment.

Depending on the investigated material, up to 4 % hydrogen is mixed with helium or argon to get rid of solved or adsorbed oxygen. Especially for nickel and copper, the deoxidization is very effective as the equilibrium constant is much higher than 1 ( $K_c \gg 1$ ) for the following reactions:



Table 2.2 shows the composition and impurities of the used gases. Furthermore, a gas purification system (Oxisorb<sup>©</sup>, Messer Group GmbH, Krefeld, Germany) was

used to remove oxygen from the gas flow to the final purity of less than 5 ppb (as specified by the manufacturer).

Table 2.2: Inert gases used to provide a clean environment.

Label	Composition [Vol.%]	Impurities [ppmv]
Helium N60	$\geq 99.9999$	$N_2 < 0.5$ $O_2 < 0.5$ $H_2O < 0.5$ Hydrocarbon $< 0.5$ $Ne < 0.5$ $H_2 < 0.5$
Argon N50	$\geq 99.999$	$N_2 \leq 5.0$ $O_2 \leq 2.0$ $H_2O \leq 3.0$ Hydrocarbon $\leq 0.5$
ARCAL 10	Ar + 2.4 Vol.% $H_2$	$N_2 \leq 80$ $O_2 \leq 20$ $H_2O \leq 40$
Custom Gas Mixture	He + 4 Vol.% $H_2$	$N_2 \leq 20$ $O_2 \leq 5.0$ $H_2O \leq 5.0$ Hydrocarbon $\leq 1.0$ $Ne \leq 10$

### 2.2.3 Electromagnetic levitation

The core part of the electromagnetic levitation device is the levitation coil, which is described in chapter 2.1.5. First, the conducting specimen is positioned inside the levitation coil using a sample holder (Figure 2.5). The sample holder is a tube made of  $Al_2O_3$ , with an inner diameter of 5 mm and an outer diameter of 8 mm.

By turning on the radio frequency generator, an AC current of 350 A with a frequency of 400 kHz flows through the water-cooled levitation coil, building up a high frequency electromagnetic field inside the levitation coil. Due to the interaction between induced eddy currents and the alternating electromagnetic field, the specimen starts to levitate. At the same time, ohmic and hysteresis losses heat up the specimen. The sample holder is lowered as soon as the specimen starts to levitate (see Figure 2.5).

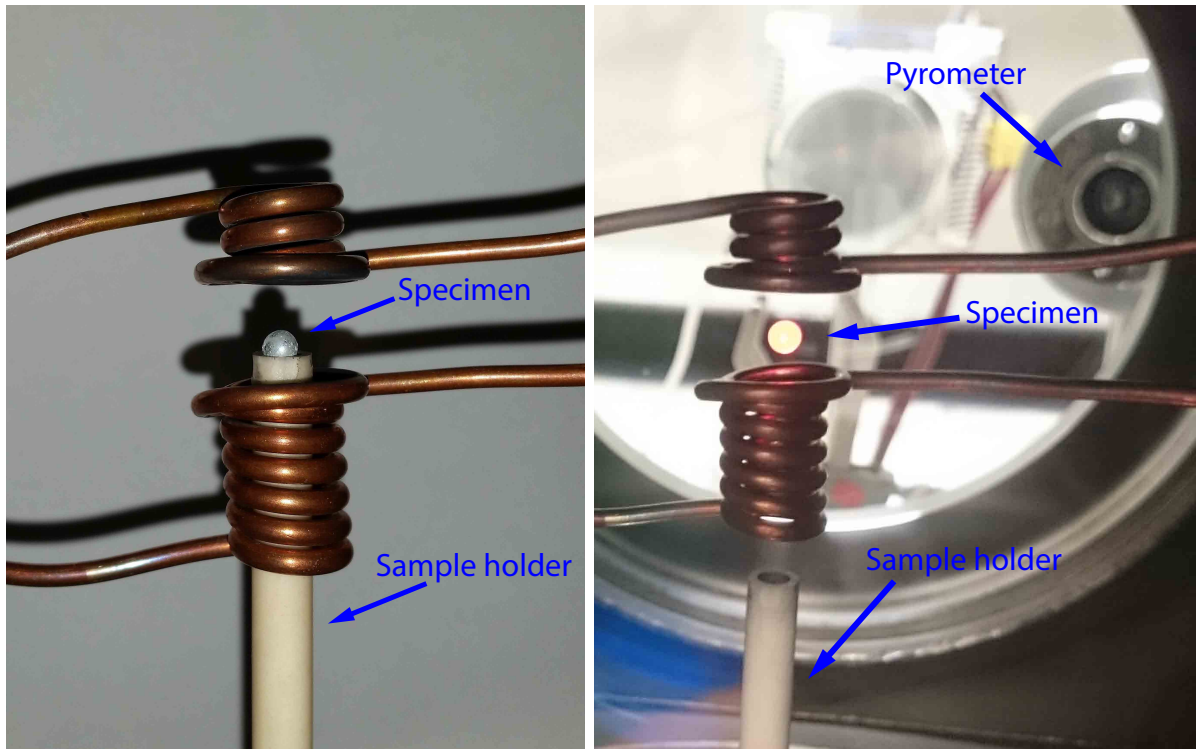


Figure 2.5: Shows the levitation coil, the sample holder and a aluminium specimen before (left) and during (right) levitation.

The sample holder ( $\text{Al}_2\text{O}_3$ -tube) is connected to the gas supply system, as illustrated in Figure 2.2. Gas flowing through the sample holder can cool the specimen from below. In this way the temperature of the specimen can be controlled.

## 2.3 Measurement technique

Contact-free measurement techniques are used to determine the relation between surface tension and temperature.

### 2.3.1 Hardware used for temperature and surface tension measurement

#### 2.3.1.1 Pyrometer

The temperature of the specimen is measured using a pyrometer (*IMPAC IGA 6 ADVANCED*, LumaSense Technologies GmbH, Frankfurt/Main, Germany). Table 2.3 shows the specifications of the pyrometer.

Table 2.3: Specifications of the **PYROMETER IMPAC IGA 6 ADVANCED**.

Temperature Ranges (MB 25)	250 °C – 2500 °C
Spectral Ranges	1.45 μm – 1.8 μm
Resolution	0.1 °C at interface 1 °C at display
Emissivity $\epsilon$	0.05 to 1.000 in steps of $10^{-3}$
Response Time $t_{90}$	120 μs – 10 s
Measurement Uncertainty ( $\epsilon = 1$ , $t_{90} = 1$ s, $T_{Ambt.} = 25$ °C)	<1500 °C: 0.3 % of reading in °C + 2 °C >1500 °C: 0.6 % of reading in °C
Repeatability ( $\epsilon = 1$ , $t_{90} = 1$ s, $T_{Ambt.} = 25$ °C)	0.15 % of reading in °C + 1 °C
Spot diameter ( $M$ )	$M = 0.003 \cdot D$ ( $D$ ... measuring distance)
The optics can be adjusted at all measuring distances $D$ between 210 mm and 5 m.	

### 2.3.1.2 Vision system

Furthermore a vision system was built within this work to allow the determination of oscillation frequencies for surface tension measurements. The vision system consists of:

- a high-speed-camera (*EoSens*<sup>®</sup> CL, Mikrotron GmbH, Unterschleissheim, Germany),
- a macro lens (*AF Micro-Nikkor ED 200 mm f/4 D IF*, Nikon Corporation, Tokio, Japan),
- a frame grabber (*Matrox Radiant eCL*, Matrox Electronic Systems Ltd., Dorval, Canada),
- and an image processing unit (PC with *MS Windows 7* as operating system).

Oscillations of the specimen for surface tension measurements are recorded by a high-speed camera. A macro lens is mounted to the high-speed camera. A frame grabber is used for data acquisition. It is connected via a Full Camera Link<sup>®</sup> configuration to the high-speed camera. The frame grabber is mounted to an x8 PCIe<sup>®</sup> slot of the image processing unit. The x8 PCIe<sup>®</sup> host interface provides the necessary throughput to ensure the continuous flow of images from the *Matrox Radiant eCL* to the RAM of an image processing unit. For every temperature point, 4100 images are recorded. Once the recording is completed, the images are saved from the RAM to a solid-state drive (SSD) for later evaluation.

Table 2.4: Specifications of the **HIGH-SPEED CAMERA Mikrotron EoSens<sup>®</sup> CL**.

Resolution	1280 × 1024
Interface	Full Camera Link <sup>©</sup>
Max. framerate (8 bit)	506 fps (full resolution)
Sensor	CMOS global shutter
Sensor format	1"
Pixel size	(14 × 14)μm
Speed raise will reached by	lines and columns
Color depth	10 bit
Dynamic range	57 dB (up to 90 dB)
Shutter time range	2 μs – 1 s
Shutter time (steps)	2 μs

Table 2.5: Specifications of the **CAMERA LENS AF Micro-Nikkor ED 200 mm f/4 D IF**.

Mount	F-Mount (Nikon bayonet mount)
Focal length	200 mm
Reproduction ratio	1:10 to 1:1 (life size)
Aperture scale	f/4 to f/32

Table 2.6: Specifications of the **FRAMEGRABBER Matrox Radiant eCL**.

Host bus interface	PCIe <sup>©</sup> 2.0 x8
Camera interface	Perform deterministic image acquisition by way of the jitter-free <b>Camera Link 2.0 interface</b>
Memory	1 GB of DDR3 SDRAM
Cameras supported	Supports most high-performance Camera Link cameras up to 85 MHz (frame and line scan sources)
Number of cameras	2 × Full/80-bit Camera Link cameras

## 2.3.2 Software used for temperature and surface tension measurement

### 2.3.2.1 Temperature measurement software

For temperature measurements, the software *InfraWin* (version 5.0.1.52) is used. This software is provided by LumaSense Technologies GmbH, the manufacturer of the pyrometer used. It is available for download on their homepage. *InfraWin* allows to display the current temperature, and to record the temperature profile during the experiment.

### 2.3.2.2 Surface tension measurement software

In the case of surface tension measurement, two software programs *ImageAcquisition* and *EvalSurfaceTension* have been written by me using the programming language *Microsoft Visual C#*.

*ImageAcquisition* is grabbing images recorded by the high-speed camera and saves them as a 8-bit greyscale images for later evaluation. An uncompressed BMP file format is used.

The second software *EvalSurfaceTension* was written for image processing. It determines the center of mass **CM**, and the radii  $R_x$  and  $R_y$  from the recorded pictures, as shown in Figure 2.6.

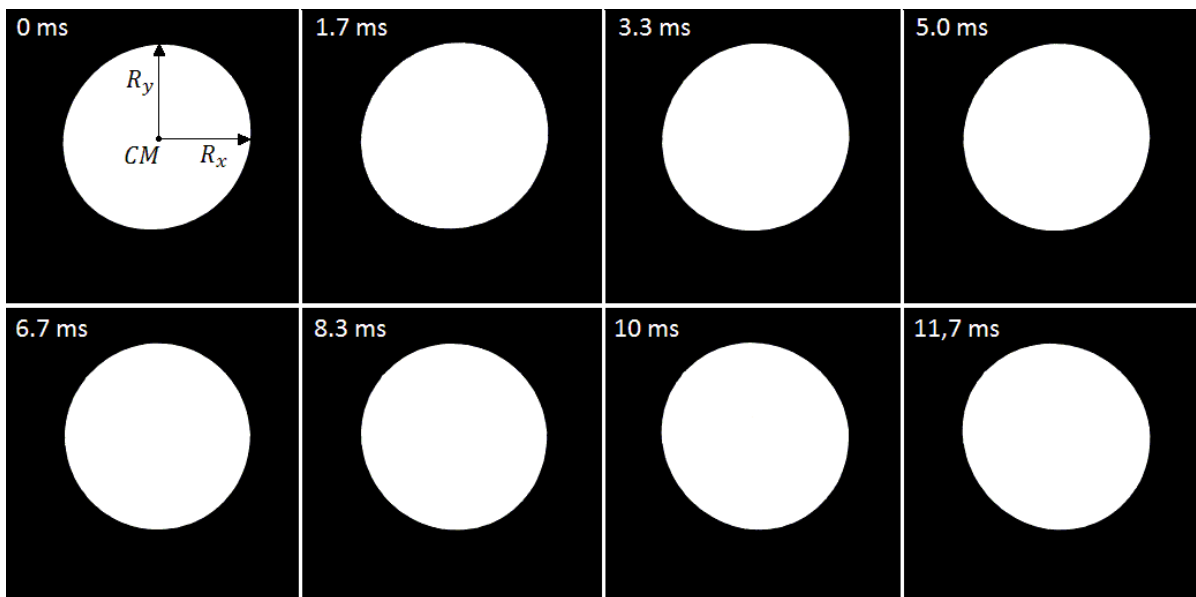


Figure 2.6: Pictures of a levitating nickel specimen taken with a high-speed camera (600 fps). **CM** is the center of mass. The radii  $R_x$  and  $R_y$  are orthogonal to each other. [2]

A threshold value between 5 and 200 is used to distinguish between the specimen and the background. For each picture, the pixel values  $I_{x,y}$  is evaluated.  $I_{x,y}$  corre-

sponds to the brightness of the pixel, with values between 0 (black) and 255 (white). The indices  $x$  and  $y$  are the Cartesian coordinates of the pixels. The bottom left corner has the coordinates  $\begin{pmatrix} 0 \\ 0 \end{pmatrix}$ .

If a pixel value is higher than a set threshold, it is part of the sample ( $\mathbf{S}_i = \begin{pmatrix} x_i \\ y_i \end{pmatrix}$ ). Otherwise the pixel is part of the background. Hence, the center of mass is calculated by the following formula:

$$\mathbf{CM} = \begin{pmatrix} \bar{x} \\ \bar{y} \end{pmatrix} = \frac{1}{N} \sum_{i=0}^N \begin{pmatrix} x_i \\ y_i \end{pmatrix}. \quad (2.2)$$

In order to determine the radius  $R_x$ , the pixels  $\mathbf{R}_i^{(x)}$  are evaluated.

$$\mathbf{R}_i^{(x)} = \begin{pmatrix} \bar{x} \\ \bar{y} \end{pmatrix} + i \begin{pmatrix} 1 \\ 0 \end{pmatrix}, \quad (2.3)$$

with  $i = 0 \dots (h - \bar{x})$  and  $h$  being the horizontal resolution of the recorded pictures. The pixels  $R_i$  are evaluated starting with  $i = 0$ . The pixel  $R_0 = \begin{pmatrix} \bar{x} \\ \bar{y} \end{pmatrix}$  is always part of the specimen and  $I_{\bar{x},\bar{y}}$  is therefor higher than the set threshold. The index  $i$  is incremented gradually by 1 (recursive definition:  $i = i + 1$ ), until the value of  $R_i$  falls below the set threshold. The radius  $R_x$  is now determined and its length in pixel is  $R_x = i - 1$ .

Analogously, the radius  $R_y$  is calculated by evaluating the pixels

$$\mathbf{R}_j^{(y)} = \begin{pmatrix} \bar{x} \\ \bar{y} \end{pmatrix} + j \begin{pmatrix} 0 \\ 1 \end{pmatrix}, \quad (2.4)$$

with  $j = 0 \dots (v - \bar{y})$  and  $v$  being the vertical resolution of the recorded pictures.

It is obvious that the length of  $R_x$  and  $R_y$  depends on the brightness of the specimen and the set threshold. For the determination of surface tension, the exact length of  $R_x$  and  $R_y$  is not needed, as only the relative change of  $R_x$  and  $R_y$  is relevant.

### 2.3.3 Temperature measurement

The temperature of the specimen is measured by means of a pyrometer in the spectral range of 1.45  $\mu\text{m}$ -1.8  $\mu\text{m}$ . This device provides a contact-free measurement technique. The position of the pyrometer is illustrated in Figure 2.2. The measuring distance is about 250 mm. The spot diameter for this distance is 0.75 mm, as can be calculated from the formula given in Table 2.3.

The only disadvantage of pyrometers is the need for spectral emissivity values of the specimen to determine its true temperature. If the spectral emissivity is unknown, the liquidus temperature is either taken from literature or measured by differential thermal analysis (DTA), and then assigned to the melting plateau in the pyrometer signal. The Temperature of the specimen above the liquidus temperature is determined with the assumption of a constant emissivity in the liquid phase.

### 2.3.4 Determination of the oscillation frequencies

In order to calculate the surface tension using the oscillating drop technique, the translation frequencies  $\nu_{1,m}$  and oscillation frequencies  $\nu_{2,m}$  have to be determined. As shown in Figure 2.2, a high-speed camera is positioned on top of the vacuum chamber, recording the top view projection of the specimen. Up to 600 fps (frames per second) are recorded at a resolution of  $(1024 \times 1024)$  pixel.

The translation frequencies  $\nu_{1,m}$  for the correction term in Eq. (1.15) are obtained from the Fourier transform of the center of mass, whereas the oscillation frequencies  $\nu_{2,m}$  are obtained from the Fourier transform of the radii  $R_x$  and/or  $R_y$ .

The frequencies  $\nu_{2,\pm 1}$  and  $\nu_{2,\pm 2}$  depend on the rotation frequency  $\Omega$  as well as on the index  $m$  and split symmetrically [19]

$$\nu_{2,\pm m}(\Omega) = \overline{\nu_{2,|m|}} \pm |m|\Omega. \quad (2.5)$$

In the case of non-rotating specimens ( $\Omega = 0$ ), only three oscillation frequencies for  $l = 2$  appear. The frequencies  $\nu_{2,+1}$  and  $\nu_{2,-1}$  as well as  $\nu_{2,+2}$  and  $\nu_{2,-2}$  are degenerated. Eq. (1.13c) becomes

$$\nu_2^2 = \frac{1}{5}(\nu_{2,0}^2 + 2 \cdot \overline{\nu_{2,1}^2} + 2 \cdot \overline{\nu_{2,2}^2}), \quad (2.6)$$

where  $\overline{\nu_{2,1}}$  and  $\overline{\nu_{2,2}}$  are defined as

$$\overline{\nu_{2,1}} := \frac{1}{2}(\nu_{2,+1} + \nu_{2,-1}), \quad (2.7a)$$

$$\overline{\nu_{2,2}} := \frac{1}{2}(\nu_{2,+2} + \nu_{2,-2}), \quad (2.7b)$$

and therefore the non-degenerated frequency  $\nu_{2,0}$  needs to be assigned in order to calculate  $\nu_2^2$  [17].

In general, specimens rotate under terrestrial conditions. In the case of rotating specimens, five peaks are visible. However, this is not always the case. The Fourier transform of  $R_x$  for Cu-5Sn delivered only four frequencies. By assigning the oscillation frequencies, it can be shown that one of the oscillating frequencies  $\nu_{2,\pm 1}$  overlaps with one of the oscillating frequencies  $\nu_{2,\pm 2}$ .

The Fourier transform of two orthogonal radii  $R_x$  and  $R_y$  for aluminium is shown in Figure 2.7. The oscillation modes with  $l = 2$  and  $m = \pm 1$  are not clearly visible, whereas the oscillation modes with  $l = 2$  and  $m = \pm 2$  appear distinctly. In chapter 2.3.6, it will be discussed how to assign the oscillation modes with  $l = 2$  and clearly find and distinguish them.

### 2.3.5 Specimen geometry

The radius  $R_{l,m}$  for a designated oscillation mode  $l$  and  $m$  is described by:

$$R_{l,m}(\vartheta, \varphi, t) = a_0 + a_{l,m}(t)P_l^m(\cos \vartheta) \cos(m\varphi), \quad \text{if } m \geq 0 \quad (2.8a)$$

$$R_{l,m}(\vartheta, \varphi, t) = a_0 + a_{l,m}(t)P_l^{-|m|}(\cos \vartheta) \sin(-|m|\varphi). \quad \text{if } m < 0 \quad (2.8b)$$

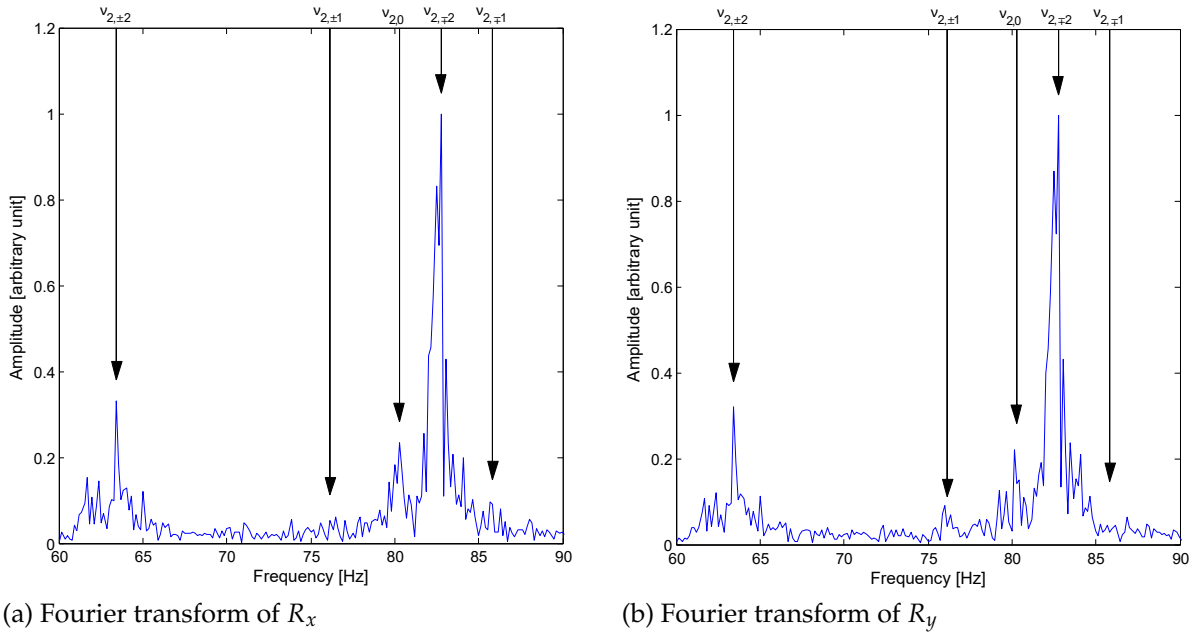


Figure 2.7: Spectrum of the oscillation frequencies with  $l = 2$  for aluminium obtained by the Fourier transform of  $R_x$  (a) and  $R_y$  (b).

The oscillation mode with  $l = 0$  and  $m = 0$  corresponds to an expansion and a contraction of the sample. As a consequence, this mode is also called the breathing mode. As we are dealing with liquid specimen, neither an expansion nor a contraction occurs. The radius  $R_{0,0}$  for the oscillation mode  $l = 0$  and  $m = 0$  is constant and therefore suppressed.

$$R_{0,0}(\vartheta, \varphi, t) = a_0. \quad (2.9)$$

Figure 2.8 shows an asymmetric deformation of the specimen which is linked to the oscillation mode with  $l = 1$  and  $m = 0$ . Analogously, the oscillation modes  $l = 1$

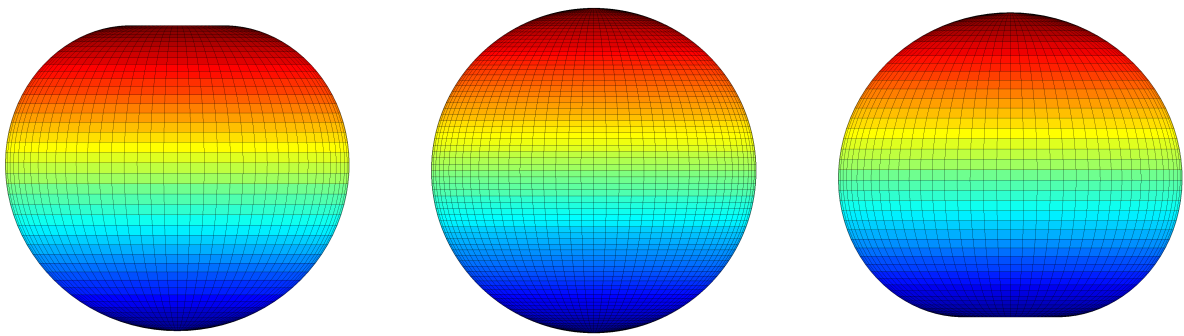


Figure 2.8: Oscillation modes with  $l = 1$  and  $m = 0$ .

and  $m = \pm 1$  correspond to asymmetric deformations of the specimen in the other

two spatial dimensions. The oscillation modes with  $l = 1$  are described by:

$$R_{1,0}(\vartheta, \varphi, t) = a_0 + a_{1,0}(t) \cos \vartheta, \quad (2.10a)$$

$$R_{1,+1}(\vartheta, \varphi, t) = a_0 + a_{1,+1}(t) \sin \vartheta \cos \varphi, \quad (2.10b)$$

$$R_{1,-1}(\vartheta, \varphi, t) = a_0 + a_{1,-1}(t) \sin \vartheta \sin \varphi. \quad (2.10c)$$

For small amplitudes, no asymmetric deformations are observed as shown in Figure 2.8, but a translation of the sample can be seen instead.

The oscillation modes with  $l = 2$  and  $m = 0, 1, 2$  are shown in Figure 2.9. The radii of the five oscillation modes with  $l = 2$  and  $m = 0, \pm 1, \pm 2$  are defined according to Eq. (2.8) as:

$$R_{2,0}(\vartheta, \varphi, t) = a_0 + \frac{1}{2}a_{2,0}(t)(3 \cos^2 \vartheta - 1), \quad (2.11a)$$

$$R_{2,+1}(\vartheta, \varphi, t) = a_0 + 3a_{2,+1}(t) \sin \vartheta \cos \vartheta \cos \varphi, \quad (2.11b)$$

$$R_{2,-1}(\vartheta, \varphi, t) = a_0 + 3a_{2,-1}(t) \sin \vartheta \cos \vartheta \sin \varphi, \quad (2.11c)$$

$$R_{2,+2}(\vartheta, \varphi, t) = a_0 + 3a_{2,+2}(t) \sin^2 \vartheta \cos(2\varphi), \quad (2.11d)$$

$$R_{2,-2}(\vartheta, \varphi, t) = a_0 + 3a_{2,-2}(t) \sin^2 \vartheta \sin(2\varphi). \quad (2.11e)$$

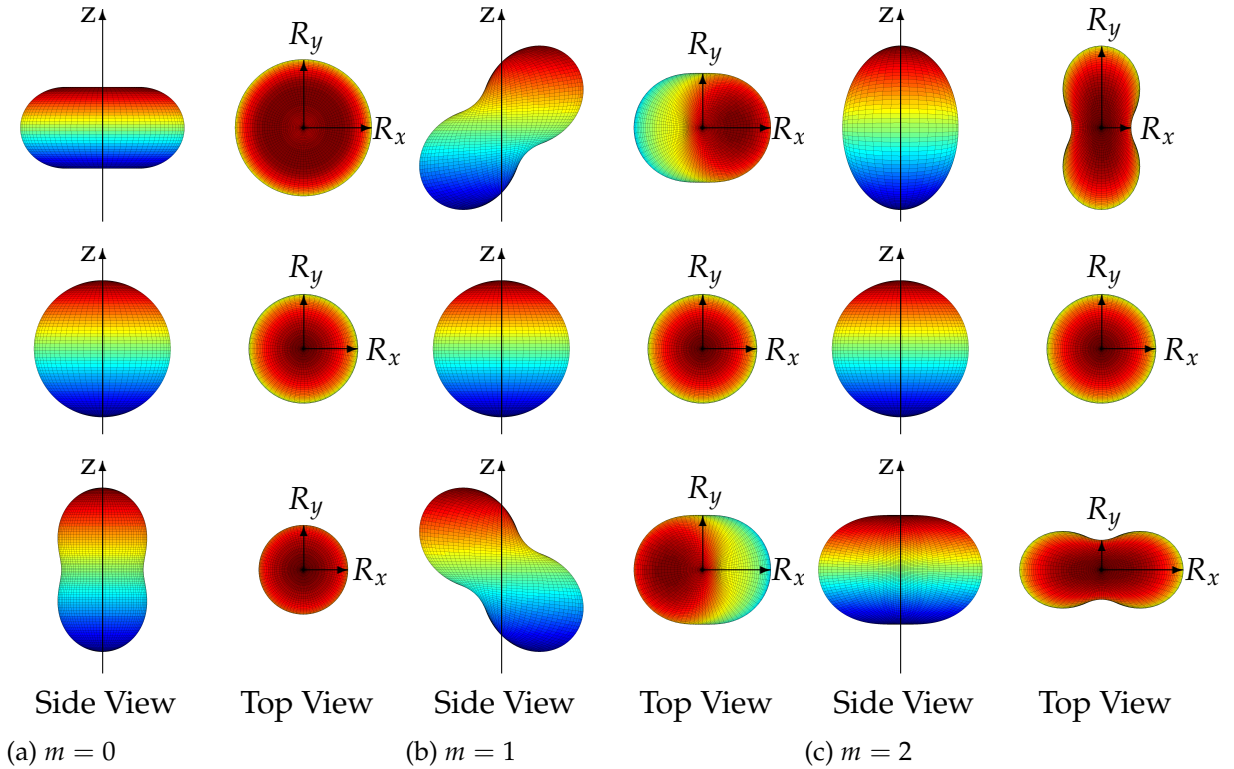


Figure 2.9: Oscillation modes with  $l = 2$  and (a)  $m = 0$ , (b)  $m = 1$ , (c)  $m = 2$ .

### 2.3.6 Assignment of the oscillation frequencies $\nu_{2,m}$

By performing the Fourier transform of the radii  $R_x$  and  $R_y$ , the oscillation frequencies with  $l = 2$  are obtained as shown in Figure 2.7 and in the publications [3], [2], and [1], but cannot be assigned. To designate the oscillation modes  $m = 0, \pm 1, \pm 2$ , the specimen geometry for the oscillation modes with  $l = 2$  is used, as shown in Figure 2.9 and described mathematically in Eq. (2.11). As mentioned, a high-speed camera positioned on top of the vacuum chamber records a top view projection of the specimen (Figure 2.6). By evaluating two additional values  $R^+$  and  $R^-$  defined as:

$$R^\pm = R_x \pm R_y, \quad (2.12)$$

the oscillation modes  $m = 0, m = \pm 1$ , and  $m = \pm 2$  can be designated.

The radius of the oscillation mode  $l = 2$  and  $m = 0$  has no  $\varphi$ -dependency (see Eq. (2.11a)), which means that it is rotationally symmetric around the z-axis. The top view projection of the specimens' shape shows a disc as can be seen in Figure 2.9a. Consequently,  $R^-$  is equal to zero and therefore the Fourier transform of  $R^-$  does not show the oscillation frequency  $\nu_{2,0}$ . The Fourier transform of  $R^-$  for aluminium is shown in Figure 2.10a. The disappearing peak can be assigned as the oscillation frequency  $\nu_{2,0}$  (highlighted with the color magenta in Figure 2.10a).

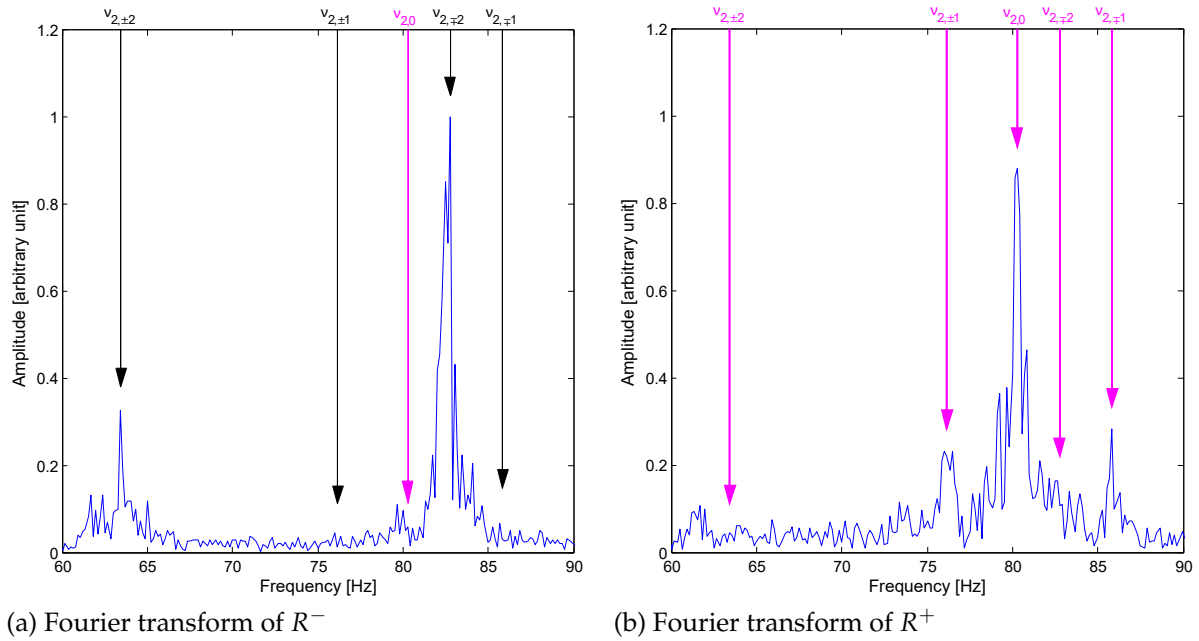


Figure 2.10: The Fourier transform of (a)  $R^-$  showing the frequencies  $\nu_{2,\pm 1}$  and  $\nu_{2,\pm 2}$ , and (b)  $R^+$  showing the frequencies  $\nu_{2,0}$  and  $\nu_{2,\pm 1}$ .

Figure 2.9c does not show clearly that  $R^+$  is constant for the oscillation mode  $l = 2$  and  $m = \pm 2$ . The top view projection of the oscillation mode  $l = 2$  and  $m = \pm 2$ ,

derived from Eq. (2.11d) and (2.11e), are

$$R_{xy,2,+2}(\varphi, t) = R_{2,+2}\left(\frac{\pi}{2}, \varphi, t\right) = a_0 + 3a_{2,0}(t) \cos 2\varphi, \quad (2.13a)$$

$$R_{xy,2,-2}(\varphi, t) = R_{2,-2}\left(\frac{\pi}{2}, \varphi, t\right) = a_0 + 3a_{2,0}(t) \sin 2\varphi. \quad (2.13b)$$

From Eq. 2.13a, the sum of the two orthogonal radii is

$$\begin{aligned} R^+ &= R_{xy,2,+2}(\varphi, t) + R_{xy,2,+2}(\varphi + \pi/2, t) \\ &= a_0 + 3a_{2,0}(t) \cos(2\varphi) + a_0 + 3a_{2,0}(t) \cos(2\varphi + \pi) \\ &= 2a_0 + 3a_{2,0}(t) \cos(2\varphi) - 3a_{2,0}(t) \cos(2\varphi) = 2a_0 = \text{constant}. \end{aligned} \quad (2.14)$$

Analogously,  $R^+$  is also constant for  $R_{xy,2,-2}$ , as

$$\sin(2\varphi + \pi) = -\sin(2\varphi). \quad (2.15)$$

Hence, in the Fourier transform of  $R^+$  (Figure 2.10b) only the frequencies  $\nu_{2,0}$  and  $\nu_{2,\pm 1}$  appear and the frequencies  $\nu_{2,\pm 2}$  are suppressed. With this additional spectrum shown in Figure 2.10b, the frequencies  $\nu_{2,\pm 1}$  and  $\nu_{2,\pm 2}$  can be assigned as well.

In the case of aluminium, the Fourier transform of  $R^+$  is not only important for the designation of the frequencies, but also shows the frequencies  $\nu_{2,\pm 1}$  clearly, which are not clearly visible in the Fourier transform of  $R_x$  and  $R_y$ .

---

## 3 Uncertainties

---

### 3.1 Uncertainty due to oscillation frequencies, mass, density of the specimen

Table 3.1 and Table 3.2 show the uncertainty budget for surface tension calculated with the software *GUM Workbench*<sup>®</sup> *version 2.4* [20]. The statistical and mathematical analysis used in *GUM Workbench*<sup>®</sup> is based on the Guide to the Expression of Uncertainty in Measurement (GUM) [21]. Eq. (1.15) was used as the model equation.

Uncertainty Contribution = Sensitivity Coefficient  $\times$  Standard Uncertainty

$$\Delta\gamma(x_i) = \frac{\partial\gamma(x_1, x_2, \dots, x_i, \dots, x_n)}{\partial x_i} \cdot \Delta x_i. \quad (3.1)$$

All sensitivity coefficients are shown without units. The correct unit is the unit of the result quantity divided by the unit of the input quantity. The "Index" column in Table 3.1 and 3.2 indicates the percentage of the variance that stems from the given input quantity in the budget.

The quantities contributing most to the uncertainty of surface tension are highlighted in Table 3.1 and Table 3.2. An accurate determination of the frequencies  $\nu_{1,m}$  and density  $\rho$  is not important, they add up together to a relative contribution of 1.1 %. The oscillation frequencies  $\nu_{2,m}$  contribute most to the total uncertainty.

The expanded uncertainty (coverage factor = 2) for the surface tension of Cu–5Sn is  $22 \text{ mN m}^{-1}$ , considering only uncertainties due to  $\nu_{1,m}$ ,  $\nu_{2,m}$ ,  $M$ , and  $\rho$ .

Analogously, the expanded uncertainty for nickel was calculated. Table 3.2 shows that in the case of nickel, the oscillation frequencies  $\nu_{2,m}$  contribute most to the total uncertainty as well.

The density of nickel and Cu–5Sn was measured in our workgroup with the levitation and pulse heating technique. The results for nickel are published in [18]. These

Table 3.1: Uncertainty contribution of  $\nu_{1,m}$ ,  $\nu_{2,m}$ ,  $M$ , and  $\rho$  to the uncertainty of surface tension for Cu-5Sn at the temperature of 1388 K.

Quantity	Value	Standard Uncertainty	Sensitivity Coefficient	Uncertainty Contribution	Index
$\nu_{1,0}$	4.98 Hz	0.06 Hz	$8.5 \cdot 10^{-3}$	$0.51 \text{ mN m}^{-1}$	0.2 %
$\nu_{1,-1}$	4.39 Hz	0.06 Hz	$7.5 \cdot 10^{-3}$	$0.45 \text{ mN m}^{-1}$	0.2 %
$\nu_{1,+1}$	4.69 Hz	0.06 Hz	$8.0 \cdot 10^{-3}$	$0.48 \text{ mN m}^{-1}$	0.2 %
$\nu_{2,0}$	51.4 Hz	0.5 Hz	$9.9 \cdot 10^{-3}$	$4.9 \text{ mN m}^{-1}$	19.5 %
$\nu_{2,\pm 1}$	47.3 Hz	0.5 Hz	$9.1 \cdot 10^{-3}$	$4.5 \text{ mN m}^{-1}$	16.5 %
$\nu_{2,\mp 1}$	56.1 Hz	0.5 Hz	$1.1 \cdot 10^{-2}$	$5.4 \text{ mN m}^{-1}$	23.1 %
$\nu_{2,\pm 2}$	37.3 Hz	0.5 Hz	$7.2 \cdot 10^{-3}$	$3.6 \text{ mN m}^{-1}$	10.2 %
$\nu_{2,\mp 2}$	56.1 Hz	0.5 Hz	$1.1 \cdot 10^{-2}$	$5.4 \text{ mN m}^{-1}$	23.1 %
$M$	407 mg	1 mg	$2.9 \cdot 10^3$	$2.9 \text{ mN m}^{-1}$	6.5 %
$\rho$	$8000 \text{ kg m}^{-3}$	$120 \text{ kg m}^{-3}$	$-6.4 \cdot 10^{-6}$	$-0.76 \text{ mN m}^{-1}$	0.5 %
$\gamma(1388 \text{ K}) = (1109 \pm 22) \text{ mN m}^{-1}$ (expanded uncertainty, coverage factor = 2)					

measured values were used for the calculation of surface tension presented in this work.

In the temperature range from melting to 2000 K, the density of nickel decreases from  $7850 \text{ kg m}^{-3}$  to  $7550 \text{ kg m}^{-3}$ . Further, the density of nickel at room temperature is  $8900 \text{ kg m}^{-3}$  [22]. Table 3.3 shows that even using the density value at room temperature for surface tension calculation leads only to a variance of about 0.36 %. Therefore, using only the density value at liquidus for the calculation of surface tension over the entire measurement range (1700 K - 2000 K) is acceptable.

The uncertainty of the specimens mass  $M$  (shown in Table 3.1 and 3.2) stems from mass evaporation. The specimen is weighed before as well as after each experiment. As the measurements in the study have been carried out under barometric pressure, no significant evaporation could be observed. In the case of Cu-5Sn and nickel, mass evaporation was 0.25 % and 0.16 %. Table 3.1 and Table 3.2 show that uncertainties in mass are almost negligible.

However, electrostatic levitation for instance operate under high vacuum condition. Therefore the prediction of mass evaporation becomes important [23].

Table 3.2: Uncertainty contribution of  $\nu_{1,m}$ ,  $\nu_{2,m}$ ,  $M$ , and  $\rho$  to the uncertainty of surface tension for nickel at the temperature of 1758 K.

Quantity	Value	Standard Uncertainty	Sensitivity Coefficient	Uncertainty Contribution	Index
$\nu_{1,0}$	5.42 Hz	0.06 Hz	$-2.7 \cdot 10^{-3}$	$-0.16 \text{ mN m}^{-1}$	0.0 %
$\nu_{1,-1}$	5.86 Hz	0.06 Hz	$-3.0 \cdot 10^{-3}$	$-0.18 \text{ mN m}^{-1}$	0.0 %
$\nu_{1,+1}$	6.3 Hz	0.06 Hz	$-3.2 \cdot 10^{-3}$	$-0.19 \text{ mN m}^{-1}$	0.0 %
$\nu_{2,0}$	44.53 Hz	0.5 Hz	$2.6 \cdot 10^{-2}$	$13 \text{ mN m}^{-1}$	26.8 %
$\nu_{2,\pm 1}$	35.6 Hz	0.5 Hz	$2.1 \cdot 10^{-2}$	$10 \text{ mN m}^{-1}$	17.1 %
$\nu_{2,\mp 1}$	41.25 Hz	0.5 Hz	$2.4 \cdot 10^{-2}$	$12 \text{ mN m}^{-1}$	23.0 %
$\nu_{2,\pm 2}$	27.4 Hz	0.5 Hz	$1.6 \cdot 10^{-2}$	$8 \text{ mN m}^{-1}$	10.2 %
$\nu_{2,\mp 2}$	39.55 Hz	0.5 Hz	$2.3 \cdot 10^{-2}$	$12 \text{ mN m}^{-1}$	21.1 %
$M$	1241 mg	2 mg	$1.6 \cdot 10^3$	$3.2 \text{ mN m}^{-1}$	1.7 %
$\rho$	$7800 \text{ kg/m}^3$	$120 \text{ kg/m}^3$	$-5.9 \cdot 10^{-6}$	$-0.71 \text{ mN m}^{-1}$	0.1 %

$\gamma(1758 \text{ K}) = (1960 \pm 50) \text{ mN m}^{-1}$  (expanded uncertainty, coverage factor = 2)

Table 3.3: The surface tension of nickel at the temperature of 1758 K for different density values and its variance from the correct value.

Temperature [K]	Density [ $\text{kg m}^{-3}$ ]	Surface tension at 1758 K [ $\text{mN m}^{-1}$ ]	Variance from correct value ( $1960 \text{ mN m}^{-1}$ )
1758	7800	1960	$0 \text{ mN m}^{-1}$
liquidus	7850	1959	$1 \text{ mN m}^{-1} \hat{=} 0.05 \%$
2000	7550	1961	$1 \text{ mN m}^{-1} \hat{=} 0.05 \%$
room temperature	8900	1953	$7 \text{ mN m}^{-1} \hat{=} 0.36 \%$

### 3.2 Uncertainty due to temperature

The measurement uncertainty of temperature  $\Delta T$  is estimated to be about 10 K. It originates from inaccurate determination of the liquidus temperature and the temperature dependence of emissivity. Nevertheless, the uncertainty of temperature is in most cases negligible due to the small slope of the surface tension versus temperature,

as can be seen Table 3.4. The relative uncertainty is calculated by

$$\Delta\gamma = \frac{\partial\gamma}{\partial T}\Delta T. \quad (3.2)$$

Table 3.4: Relative uncertainty  $\frac{\Delta\gamma}{\gamma}$  for the surface tension of copper, nickel, aluminium, and Cu-5Sn due to inaccurate temperature measurement ( $\Delta T = 10$  K).

<b>Material</b>	$\frac{\partial\gamma}{\partial T}$ [mN · m <sup>-1</sup> · K <sup>-1</sup> ]	<b>Relative Uncertainty</b> $\frac{\Delta\gamma}{\gamma}$
Cu	0.21	0.2 %
Ni	0.35	0.2 %
Al	0.11	0.1 %
Cu-5Sn	0.052	0.05 %

---

## 4 Discussion

---

In this study, the surface tension was measured by means of the oscillating drop technique. A main objective of this work was to verify how accurate surface tension can be measured by the oscillating drop technique and how precise surface tension measurements are in general. For this reason, metals as copper and nickel were investigated and compared to data from literature. Copper and nickel were chosen because plenty of reference data were available for these two metals and a detailed comparison could be carried out [2, 3]. Furthermore, alloys such as Cu–5Sn and Cu–5Sn–1Zn were investigated. The results and difficulties when measuring alloys will be also discussed within this chapter.

### 4.1 Determination of surface tension

Surface tension under terrestrial conditions is calculated from Eq. (1.15) by determining the oscillation frequencies  $\nu_{1,m}$  and  $\nu_{2,m}$ , the mass  $M$ , and the radius  $R$  of the specimen. The translation frequencies  $\nu_{1,m}$  and the radius  $R$  are used for the correction term and do not contribute much to the measurement uncertainty.

#### 4.1.1 Determination of the specimens' mass

The mass of the specimen is measured with a precision balance (*AB-104-S-A*, Mettler-Toledo GmbH, Gießen, Germany). With an accuracy of 0.1 mg, the uncertainty of the mass measurement does not contribute to the total uncertainty of surface tension. However, mass evaporation may have a big influence on the total uncertainty. For this reason, the mass is measured before as well as after each experiment to ensure that no evaporation occurred. If evaporation occurs, loss in mass has to be taken into account for the determination of surface tension or at least the uncertainty due to

mass evaporation has to be estimated. The experiments are carried out under a pressure between 700 mbar and 1500 mbar. For copper and nickel, no notable evaporation is observed in the measured temperature ranges.

However the investigation of Cu–5Sn–1Zn was not possible, because extremely high evaporation occurred during the experiment. In advance, we assumed to get difficulties, as the boiling point of zinc (1180 K) is lower than the liquidus temperature of the alloy Cu–5Sn–1Zn (1318 K). As a matter of fact, the alloy Cu–5Sn–1Zn started to evaporate in the solid phase. After a few minutes in the liquid phase the evaporation ended. A chemical analysis showed a mass content of 4.77 wt% Sn and 0.98 wt% Zn before levitation, and 4.63 wt% Sn and 0.03 wt% Zn after the experiment [1]. In other words, zinc was evaporated completely and the remaining alloy was Cu–5Sn. Anyhow, the surface tension of Cu–5Sn is also of peculiar interest and was measured within the publication [1].

In Figure 4.1, the vapor pressure of copper, tin, and zinc are shown. The dashed line marks the pressure inside the experimental chamber. The vapor pressure of zinc is a few orders of magnitude higher than the vapor pressure of copper and tin. At the liquidus temperature it is 1.8 bar, which is higher than the pressure inside the experimental chamber. In order to prevent the evaporation of zinc, a pressure higher than 10 bar should be built up inside the experimental chamber, which is not possible with the present setup.

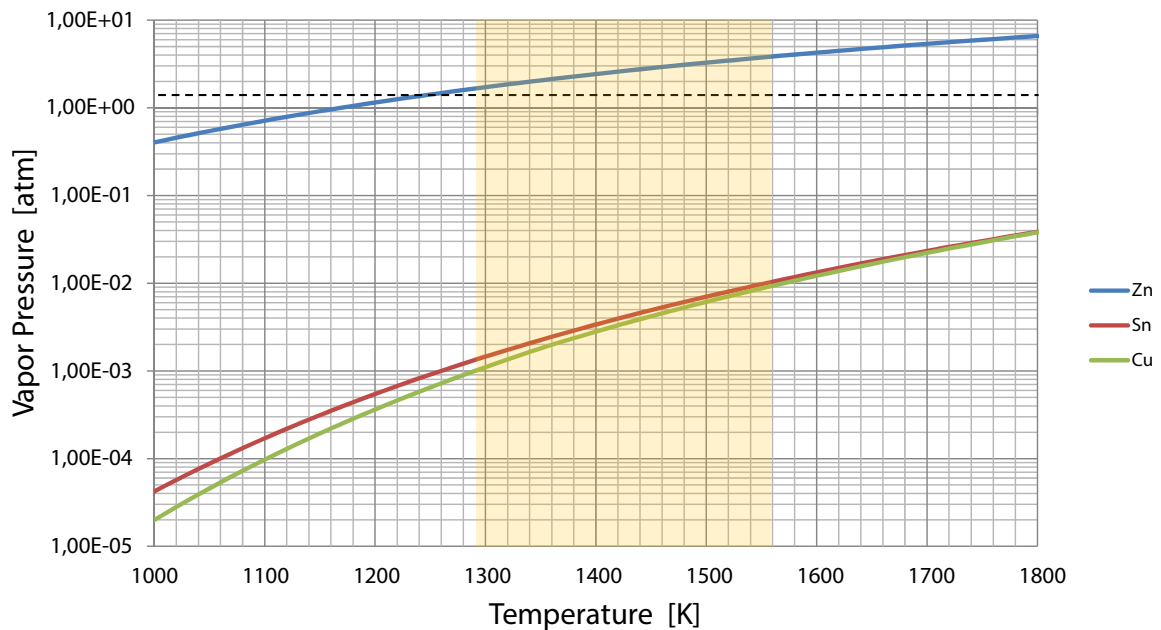


Figure 4.1: Vapor pressure of copper, tin, zinc. The dashed line marks the pressure inside the experimental chamber, which is 1.4 bar. Data taken from [24].

### 4.1.2 Determination of the oscillation frequencies $\nu_{2,m}$

As the oscillation frequencies  $\nu_{2,m}$  contribute most to the measurement uncertainty, a precise determination of these frequencies is very important. In the case of aluminium the Fourier transform of  $R_x$  and  $R_y$  does not clearly show the frequencies  $\nu_{2,\pm 1}$  (see Figure 2.7). Therefore, the Fourier transform of  $R^+$  was performed in order to designate the frequencies  $\nu_{2,\pm 1}$  better (see Figure 2.10b). Furthermore, the area  $A$  of the top view projection of the sample was determined. The Fourier transform of this additional quantity  $A$  should also show the oscillation frequencies. As a matter of fact, the oscillation frequencies  $\nu_0$  and  $\nu_{\pm 1}$  appear clearly, whereas the oscillation frequencies  $\nu_{\pm 2}$  are suppressed. Figure 4.2 shows the Fourier transform of  $A$  for aluminium, which allows better determination of the frequencies  $\nu_{\pm 1}$ .

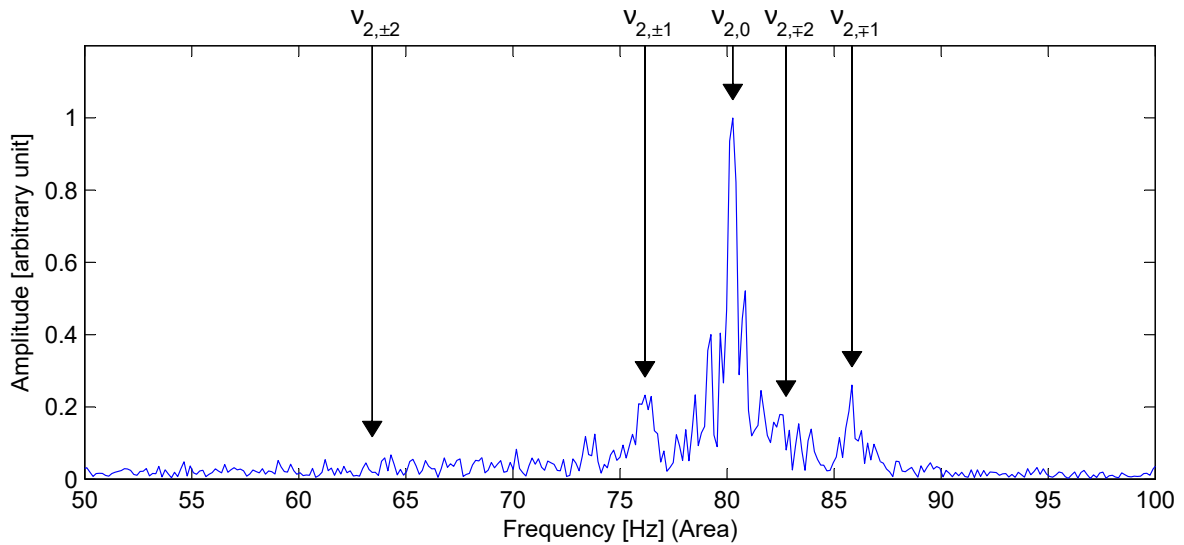


Figure 4.2: Spectrum of the oscillation frequencies with  $l = 2$  for aluminium obtained by the Fourier transform of the area  $A$ .

## 4.2 Investigation of alloys

Investigating alloys, it should be reconsidered if segregation occurs during levitation. Large differences in surface tension, atom radius, and electron configuration between the individual substances can lead to segregation. A higher concentration of substances with lower surface tension values are expected on the surface of the sample. In the case of the alloy Cu–5Sn, a high concentration of copper is expected in the center of the sample and a lower concentration at its surface, as surface tension of copper is significantly higher than the surface tension of tin (approximately three times higher).

Fortunately, mixing occurs caused by the turbulent flow of the Cu–5Sn melt, due to the eddy currents. Within the measurement uncertainties, no segregation can be

observed inside the sample, as shown in Figure 4.3.

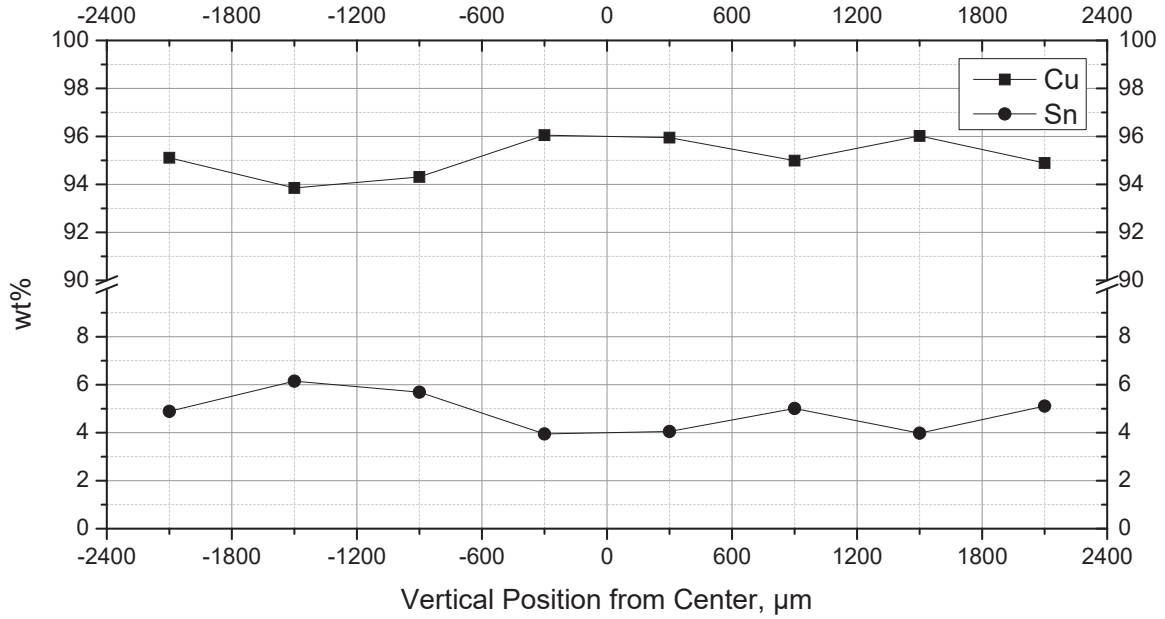


Figure 4.3: Distribution of the chemical composition of copper and tin as a function of radius inside a sample [1].

When investigating alloys, if evaporation is observed, it should be ensured whether or not the composition of the alloy has changed.

### 4.3 Alternative evaluation

In chapter 1.1.3, the determination of surface tension by means of the oscillating drop technique was quoted. In the present chapter, an alternative evaluation method will be discussed. In the case of rotating specimens under terrestrial conditions, the five-folded Rayleigh frequency  $\nu_R$  splits into five separate frequencies  $\nu_{2,0}$ ,  $\nu_{2,\pm 1}$ , and  $\nu_{2,\pm 2}$ . As the frequencies  $\nu_{2,\pm 1}$  and  $\nu_{2,\pm 2}$  split symmetrically [19], it is more consistent to use an alternative sum rule compared to Eq. (1.13c). First, the linear averages of the frequencies  $\nu_{2,\pm 1}$  and  $\nu_{2,\pm 2}$  are calculated before using a quadratic sum rule.

$$\tilde{\nu}_2^2 = \frac{1}{5} \left( \nu_{2,0}^2 + 2 \left( \frac{1}{2} (\nu_{2,-1} + \nu_{2,+1}) \right)^2 + 2 \left( \frac{1}{2} (\nu_{2,-2} + \nu_{2,+2}) \right)^2 \right). \quad (4.1)$$

In order to use Eq. (4.1), the assignment of the oscillation frequencies  $\nu_{2,m}$  is necessary. Figure 4.4 shows results for nickel specimens (measured in publication [2]). The evaluation according to Eq. (1.13c) (blue line) differs in average about  $25 \text{ mN m}^{-1}$  from the evaluation according to Eq. (4.1) (magenta line).

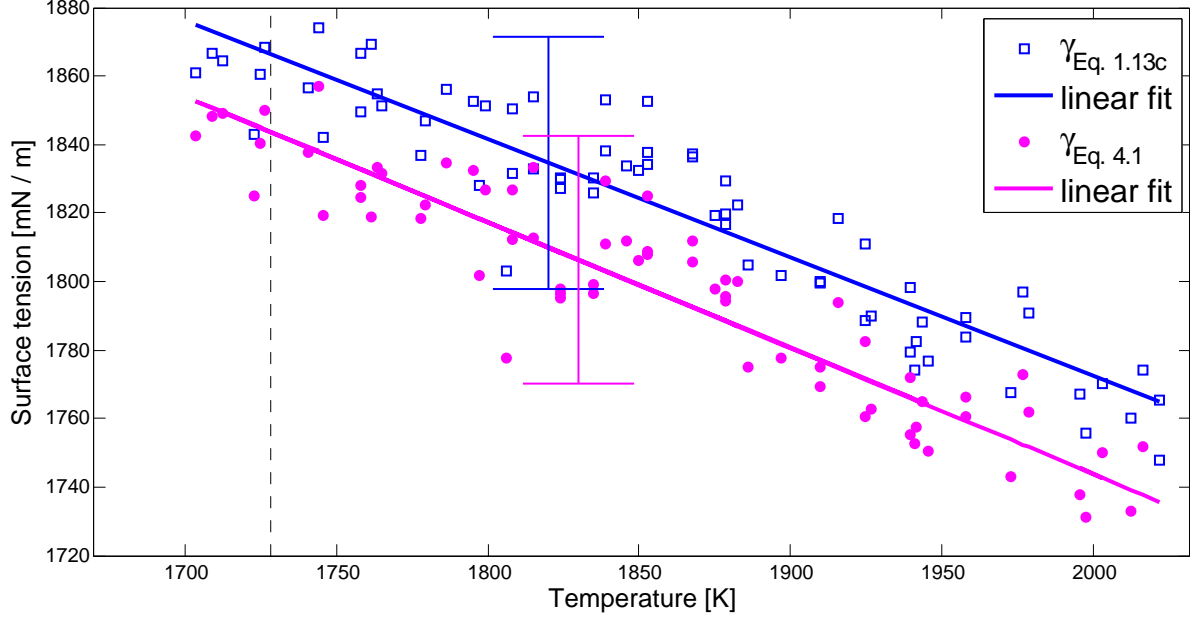


Figure 4.4: Different evaluation methods for nickel. The squared data points show the data evaluated according to Eq. (1.13c) and the circled data points show the data evaluated according to Eq. (4.1). Uncertainty bar is 2%.

Figure 4.5 shows the relative variance between the two evaluation methods. The data are normalized by the data evaluated according to Eq. (1.13c).

In the case of nickel specimens measured in [2], the relative variance is in average about 1.4% in the temperature range from 1700 K to 2020 K.

The absolute difference of surface tension measured according to Eq. (1.13c) and Eq. (4.1) is proportional to the mass  $M$  and the squared rotation frequency  $\Omega$  of the specimen, as shown in Eq. (4.2).

$$\begin{aligned}
 \gamma - \tilde{\gamma} &= \frac{3}{8}\pi M \left( v_2^2 - v_\tau^2 \left( 1.9 + 1.2 \frac{z_0^2}{R^2} \right) - \left( \tilde{v}_2^2 - v_\tau^2 \left( 1.9 + 1.2 \frac{z_0^2}{R^2} \right) \right) \right) \\
 &= \frac{3}{8}\pi M \left( v_2^2 - \tilde{v}_2^2 \right) \\
 &= \frac{3}{8}\pi M \frac{1}{10} \left( (v_{2,-1} - v_{2,+1})^2 + (v_{2,-2} - v_{2,+2})^2 \right) = \frac{6}{8}\pi M \Omega^2 \\
 &\propto M \Omega^2.
 \end{aligned} \tag{4.2}$$

The relative variance of surface tension measured according to Eq. (1.13c) and Eq. (4.1) is shown in Eq. (4.3).

$$\frac{\gamma - \tilde{\gamma}}{\gamma} = \frac{\frac{6}{8}\pi M \Omega^2}{\frac{3}{8}\pi M \left( v_2^2 - v_\tau^2 \left( 1.9 + 1.2 \frac{z_0^2}{R^2} \right) \right)} = \frac{2\Omega^2}{v_2^2 - v_\tau^2 \left( 1.9 + 1.2 \frac{z_0^2}{R^2} \right)} \approx 2 \frac{\Omega^2}{v_2^2}. \tag{4.3}$$

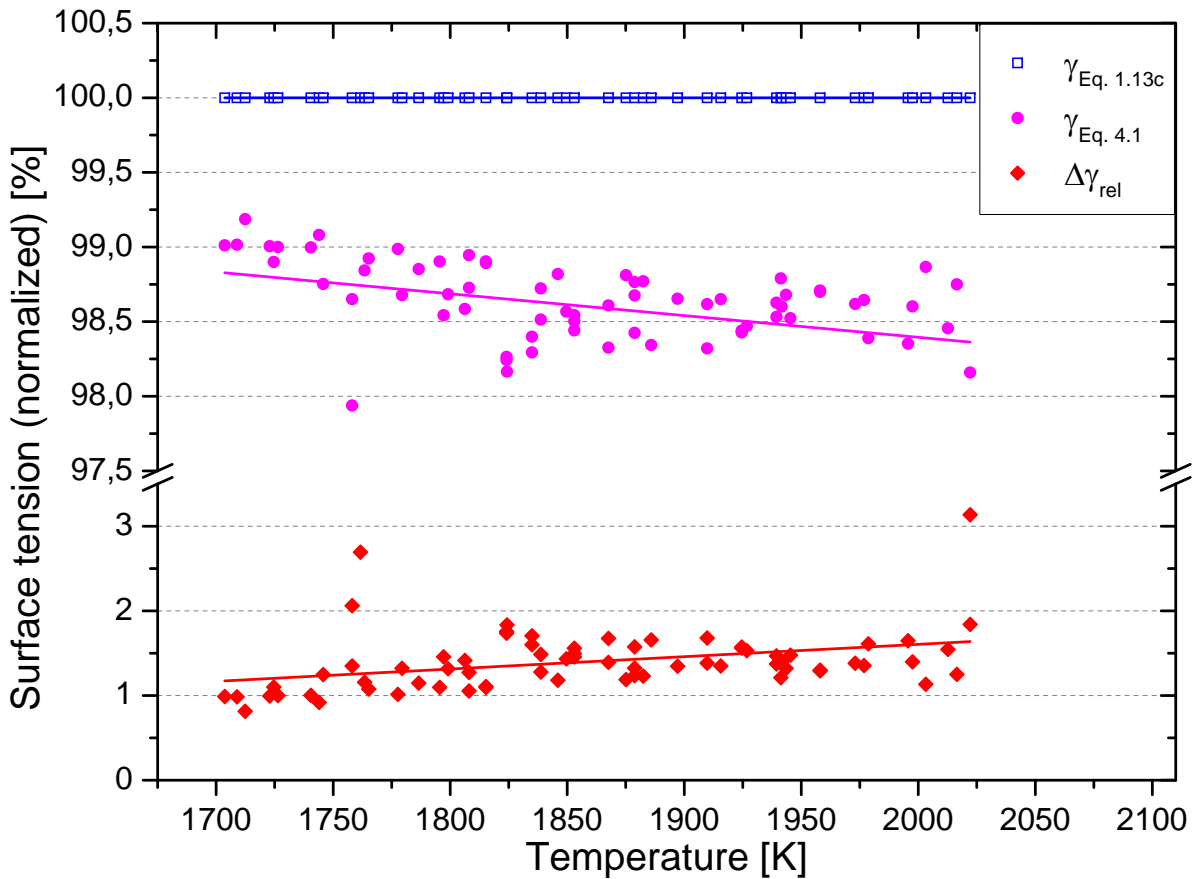


Figure 4.5: Different evaluation methods for nickel. The red line show the relative difference between the two evaluation methods Eq. (1.13c) and Eq. (4.1). Data are normalized by the data evaluated according to Eq. (1.13c).

In the case of nickel specimens measured in [2], the average rotation frequency was about 3 Hz. Eq. (4.2) and (4.3) deliver an absolute variance of  $26 \text{ mN m}^{-1}$  and a relative variance 1.4%.

The evaluation of Cu–5Sn data according to Eq. (1.13c) differ also clearly from the evaluation according to Eq. (4.1) in the temperature range from 1300 K to 1550 K (Figure 4.6). The different evaluation methods lead to an absolute variance of  $26 \text{ mN m}^{-1}$  and a relative variance of about 1.9% for Cu–5Sn, as shown in Figure 4.6 and 4.7. The average rotation frequency was about 4.7 Hz.

In the case of aluminium, the absolute variance of about  $3.7 \text{ mN m}^{-1}$  and the relative variance of 0.4% was observed for different evaluation methods in the temperature range from 1200 K to 1550 K (Figure 4.8 and 4.9). The average rotation frequency was about 3.6 Hz.

In summary, it can be stated that the sum rule quoted by Eq. (4.1) should be used and delivers in general clearly deviating values which cannot be neglected. By measuring the rotation frequency  $\Omega$  and the oscillation frequencies of the levitated specimen, the relative variance can be estimated.

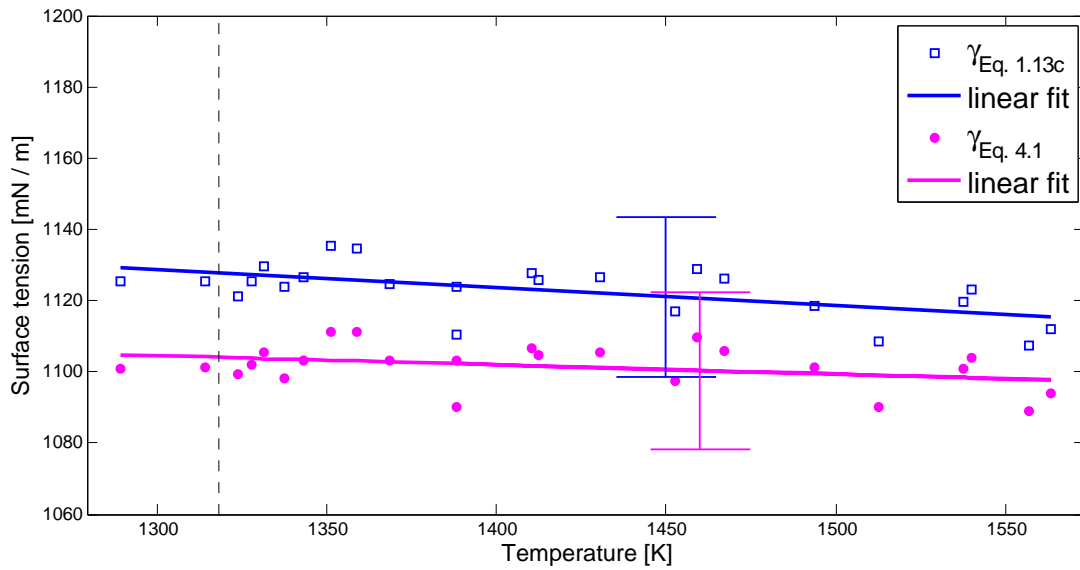


Figure 4.6: Different evaluation methods for Cu-5Sn. The squared data points show the data evaluated according to Eq. (1.13c) and the circled data points show the data evaluated according to Eq. (4.1). Uncertainty bar is 2%.

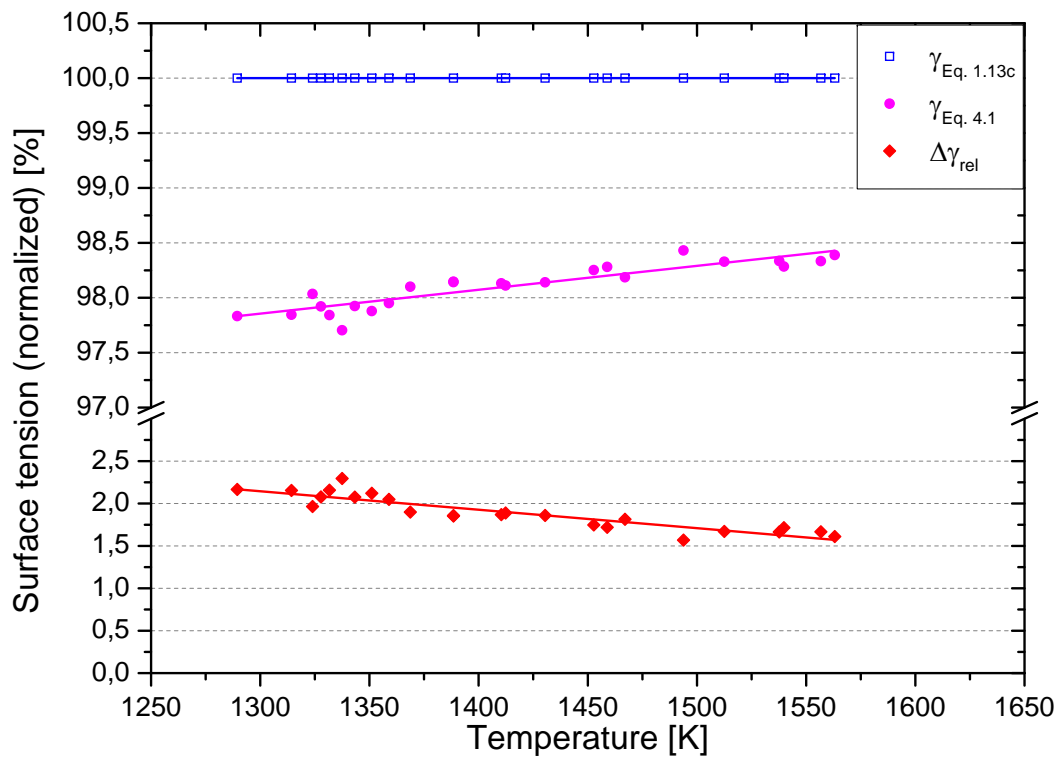


Figure 4.7: Different evaluation methods for Cu-5Sn. The red line show the relative difference between the two evaluation methods Eq. (1.13c) and Eq. (4.1). Data are normalized by the data evaluated according to Eq. (1.13c).

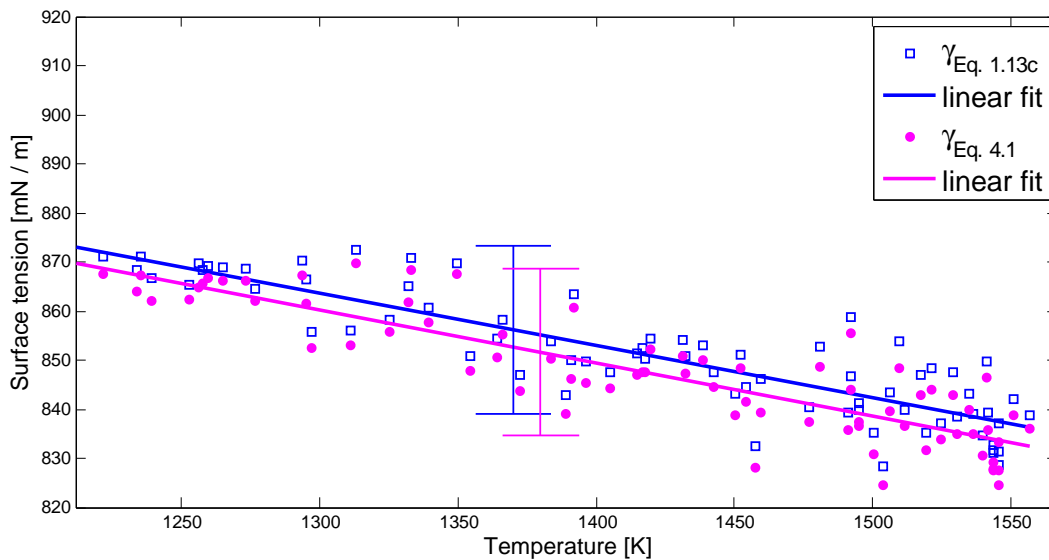


Figure 4.8: Different evaluation methods for aluminium. The squared data points show data evaluated according to Eq. (1.13c) and the circled data points show data evaluated according to Eq. (4.1). Uncertainty bar is 2 %.

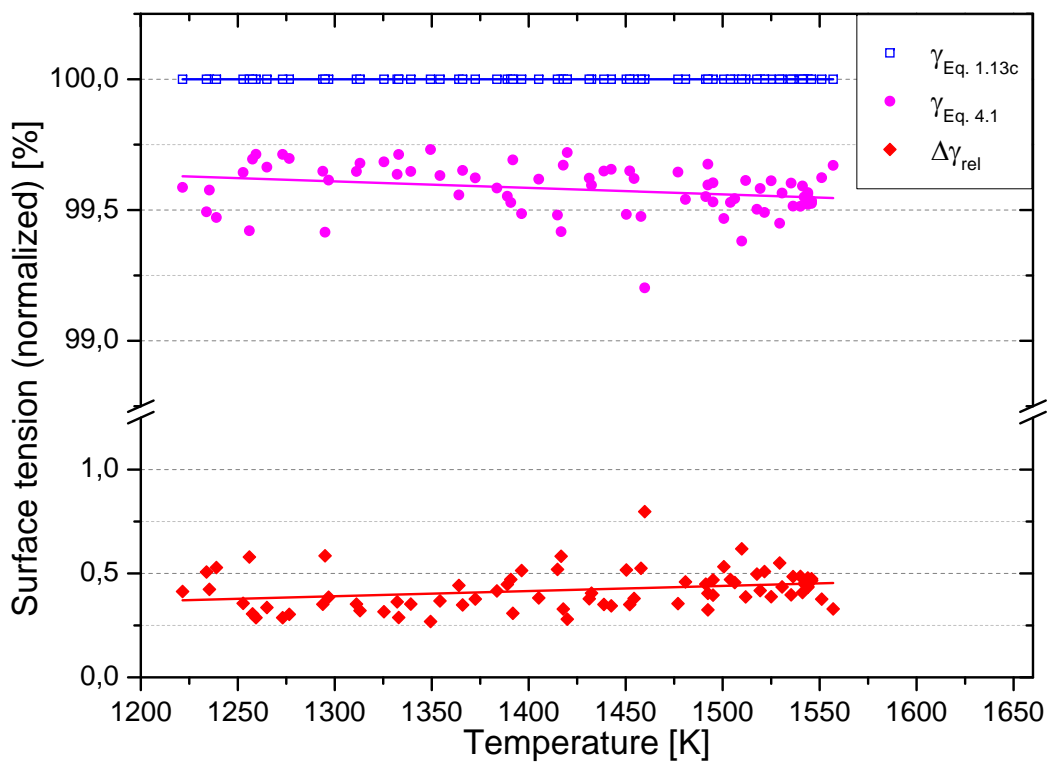


Figure 4.9: Different evaluation methods for aluminium. The red line show the relative difference between the two evaluation methods Eq. (1.13c) and Eq. (4.1). Data are normalized by data evaluated according to Eq. (1.13c).

## 4.4 Surface tension of nickel and its uncertainty

Figure 4.10 shows the surface tension of nickel as a function of temperature. The surface tension  $\gamma$  decreases with increasing temperature  $T$  in Kelvin and can be represented by a linear fit:

$$\gamma(T)[\text{mN} \cdot \text{m}^{-1}] = (1863 \pm 3) - (0.35 \pm 0.02) \cdot (T - 1728.15), \quad (4.4)$$

with a standard deviation of  $3 \text{ mN m}^{-1}$  of surface tension at melting temperature and a standard deviation of  $0.02 \text{ mN m}^{-1} \text{ K}^{-1}$  of the slope.

All data points are located in a range of  $\gamma \pm 2\%$ . The dispersion of the measurement values originates primarily from the inaccurate determination of oscillation frequencies, as is discussed in chapter 3.

Even if the uncertainty for nickel is approximately 2% (considering only uncertainties due to  $\nu_{1,m}$ ,  $\nu_{2,m}$ ,  $M$ , and  $\rho$ ), the comparison to data from literature shows a deviation of about 4% (Figure 4.11). Surface tension data with different measurement techniques have been compared.

Surface tension is determined by the microscopic structure of the surface and as a consequence, it is very sensitive to impurities. Small variation of the specimens' purity and the experimental environment can have a significant effect on the measurement.

Figure 4.10 shows three measurement series with different specimen masses, delivering the same results with an uncertainty of 2%.

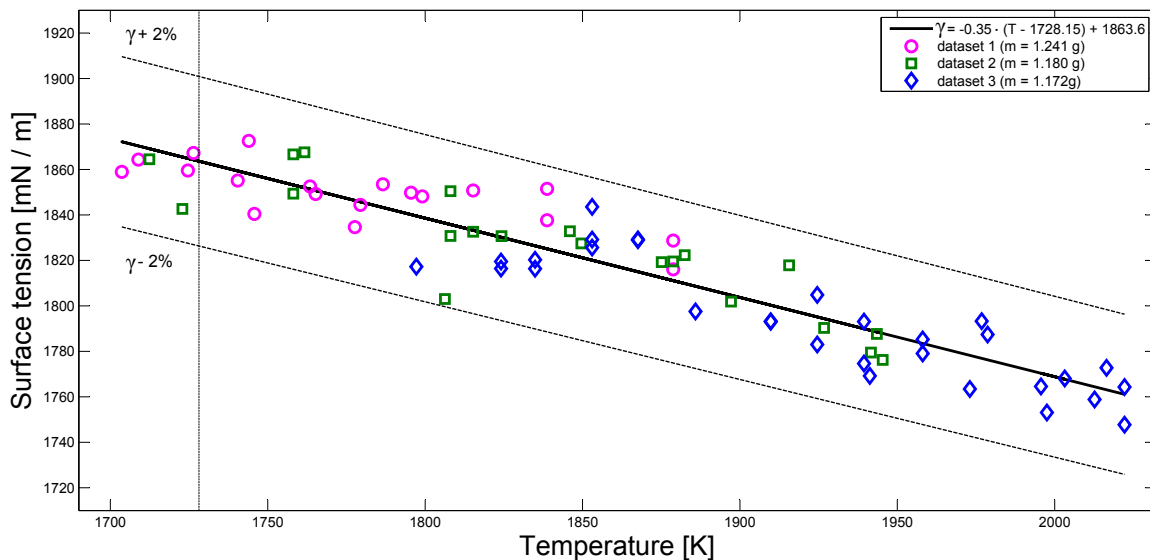


Figure 4.10: Surface tension of nickel as a function of temperature. Three specimens with different masses are investigated. Data are taken from [2] (see chapter 6.2).

Nevertheless, the results are only true for the specific experimental conditions realized in our electromagnetic levitation setup. Measurements carried out with other experimental setups delivered diverging results as shown in Figure 4.11. Therefore, using surface tension data from literature, an uncertainty of about 4 % should be assumed, as surface tension is very sensitive to impurities.

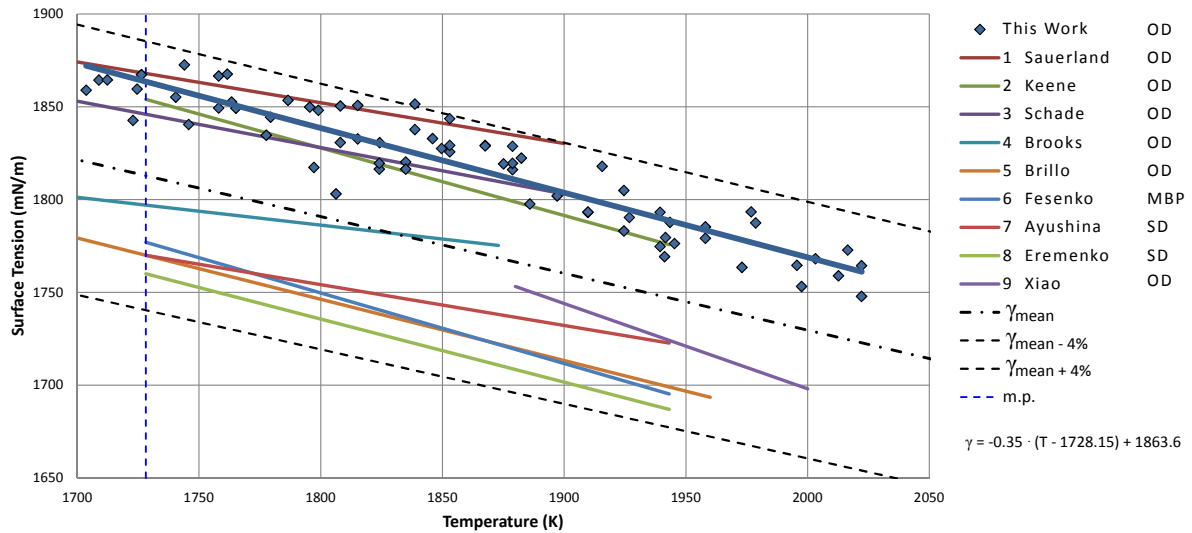


Figure 4.11: Surface tension of nickel as a function of temperature. Previously published data compared to the result of this study. Measuring techniques: Oscillating Drop (OD), Sessile Drop (SD), and Maximum Bubble Pressure (MBP). [2]

---

## 5 Outlook

---

### 5.1 Optimizations

#### Specimens' size:

During investigations conducted throughout the present work, a lot of experience could be gained. Thanks to the acquired knowledge optimizations have been carried out to achieve better results for surface tension measurements. Recent investigations of aluminium conducted by using smaller specimens showed improved results. Further analysis is required to determine the optimum size of the specimen.

#### Oscillation frequencies:

The accurate determination of the oscillation frequencies  $\nu_{2,m}$  is very important, as these frequencies contribute most to the uncertainty of the surface tension measurement. In the case of aluminium, the evaluation of the quantities  $R_x$  and  $R_y$  shows very low amplitudes for the oscillation frequencies  $\nu_{2,\pm 1}$ . The Fourier transform of the top view projection area  $A$  of the specimen showed the frequencies  $\nu_{2,\pm 1}$  clearly. Therefore, the Fourier transform of  $A$  should be reconsidered in future investigations. Further optimization (e.g. software optimization) for the accurate determination of the oscillation frequencies is recommended.

### 5.2 Oxygen detection and manipulating

Expanding the electromagnetic levitation setup via an oxygen detector is important, as such a detector allows to quantify the oxygen partial pressure inside the experimental chamber. Until now, only a low oxygen partial pressure has been ensured but not measured. Furthermore, an additional device for the manipulation of the

oxygen partial pressure enables to determine the correlation between surface tension and oxygen partial pressure.

### 5.3 Emissivity measurement

In the past, the thermophysics and metalphysics group at Graz University of Technology used a microsecond Division of Amplitude Polarymeter ( $\mu$ s-DOAP) together with the pulse-heating setup to measure normal spectral emissivity [25–29]. This quantity is of great interest, as it is needed for pyrometrical temperature measurement and is hard to determine.

Expanding the electromagnetic levitation setup by a  $\mu$ s-DOAP enables new opportunities as there is a lack of emissivity data in the literature.

In the case of pulse-heating, a thin wire with an diameter of about 0.5 mm is used as a specimen. Often it is not possible to prepare such samples (e.g. brittle metals). In these cases, the electromagnetic levitation setup can be used. Furthermore, it provides a non-destructive measurement and a larger measurement period.

Figure 5.1 shows the key elements of an emissivity measurement setup using a  $\mu$ s-DOAP. The  $\mu$ s-DOAP device consists of a polarization state generator (PSG) and a polarization state detector (PSD).

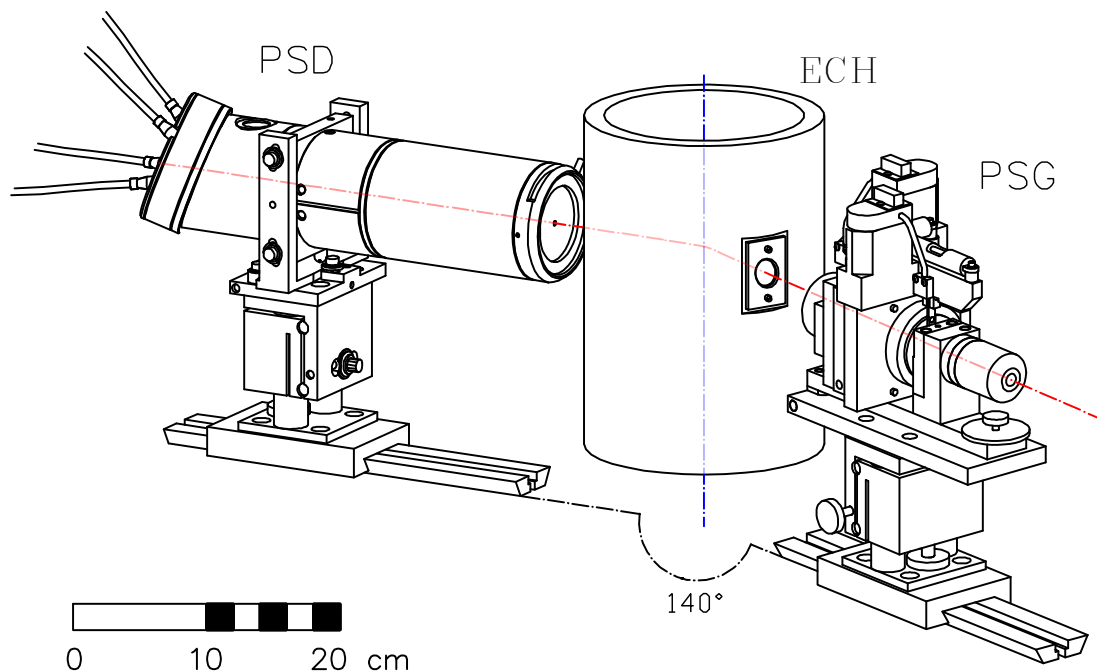


Figure 5.1: An illustration of a microsecond Division of Amplitude Polarymeter ( $\mu$ s-DOAP) together with pulse-heating setup to measure normal spectral emissivity. PSG: Polarization State Generator, PSD: Polarization State Detector, ECH: Experimental Chamber. Figure adapted from [30].

The PSG and PSD are slightly inclined towards each other and form an angle of  $140^\circ$ . To use the  $\mu$ s-DOAP with the electromagnetic levitation setup, the experimental chamber has to be adapted. Two additional windows are needed to allow a beam path as shown by the red line in Figure 5.1. A particular glass that does not change the polarization of the beam should be used. For instance, a BK-7 glass is found to meet the requirements.

---

## 6 Publications

---

- [1] K. Aziz, A. Schmon, E. Kaschnitz, J. Rattenberger, and G. Pottlacher. Measurement of surface tension of Cu–5Sn by an oscillating drop. *International Journal of Thermophysics*, 37(2), 2016.
- [2] K. Aziz, A. Schmon, and G. Pottlacher. Measurement of surface tension of liquid nickel by the oscillating drop technique. *High Temperatures-High Pressures*, 44:475–481, 2015.
- [3] K. Aziz, A. Schmon, and G. Pottlacher. Measurement of surface tension of liquid copper by means of electromagnetic levitation. *High Temperatures-High Pressures*, 43:193–200, 2014.
- [4] G. Pottlacher, K. Aziz, and A. Schmon. Thermophysical characteristics of liquid metals and alloys at TU Graz: a status report. *High Temperatures-High Pressures*, 41(5):377–394, 2012.
- [5] G. Pottlacher, A. Schmon, and K. Aziz. Investigation of liquid metallic elements and alloys by means of containerless techniques. *SF2M Annual Meeting 2012*, 2012.

## 6.1 Measurement of surface tension of Cu–5Sn by an oscillating drop technique

K. Aziz, A. Schmon, E. Kaschnitz, J. Rattenberger, and G. Pottlacher. Measurement of surface tension of Cu–5Sn by an oscillating drop. *International Journal of Thermophysics*, 37(2), 2016.

This publication discusses the surface tension measurement of the alloy Cu–5Sn. An electromagnetic levitation setup constructed by me at Graz University of Technology was used for the measurement.

### Comments:

The entire publication was written by me in cooperation with the coauthors. The surface tension of Cu–5Sn was measured by me. E. Kaschnitz provided the alloy that was investigated in this paper. He performed a chemical analysis by optical ICP emission spectroscopy as well. J. Rattenberger measured the chemical composition inside the sample by a scanning electron microscopy using energy dispersive x-ray spectroscopy. A. Schmon was my coworker and G. Pottlacher was my supervisor in this project. They were involved in all decisions, especially regarding the final text revisions.



## Measurement of Surface Tension of Cu–5Sn by an Oscillating Drop Technique

K. Aziz<sup>1</sup> · A. Schmon<sup>1</sup> · E. Kaschnitz<sup>2</sup> · J. Rattenberger<sup>3</sup> · G. Pottlacher<sup>1</sup>

Received: 21 September 2015 / Accepted: 27 November 2015  
© Springer Science+Business Media New York 2016

**Abstract** The surface tension of liquid Cu–5Sn (copper with 5 wt% tin) in the temperature range from 1290 K to 1560 K was measured by an oscillating drop technique combined with electromagnetic levitation. The levitation device uses an inhomogeneous radiofrequency electromagnetic field inside a levitation coil to position and to heat metallic material. Eddy currents are induced in a specimen to heat it to the liquid phase and to exert a Lorentz force, pushing it against gravity towards regions of lower field strength. The levitating liquid specimen takes the shape of a sphere, which is rotating and oscillating. The oscillations are recorded by a high-speed camera at 600 fps; the temperature of the specimen is measured by a fast near-infrared pyrometer. A linear fit to the measured surface tension  $\gamma$  of Cu–5Sn as a function of temperature  $T$  in Kelvin is given by:

$$\gamma(T)(\text{mN} \cdot \text{m}^{-1}) = 1195 - 0.052 \cdot (T - 1318).$$

**Keywords** Copper · Cu–5Sn · Electromagnetic levitation · Liquid alloy · Oscillating drop · Surface tension · Tin

---

✉ K. Aziz  
k.aziz@tugraz.at

<sup>1</sup> Institute of Experimental Physics, Graz University of Technology, NAWI Graz, Petersgasse 16, 8010 Graz, Austria

<sup>2</sup> Österreichisches Gießerei-Institut, Parkstraße 21, 8700 Leoben, Austria

<sup>3</sup> Institute of Electron Microscopy and Nanoanalysis, Steyrergasse 17, 8010 Graz, Austria

## 1 Introduction

The combination of the oscillating drop technique with levitation is a well-established method to measure the surface tension of electrically conducting materials. Specimens are usually levitated by either electromagnetic or electrostatic forces, or in close to zero-gravity conditions in space [1–3]. Levitation allows not only measurement in the equilibrium liquid condition, but can extend the liquid range to large undercooling [4]. As it is container and contact-less, contaminations of specimens during measurement are dramatically reduced.

Surface tension can be an important input parameter for the numerical simulation of castings. The motivation for the measurement of surface tension of Cu–5Sn (copper with 5 wt% tin) was the numerical description of metal flow in a brass furnace. When the melt volume running through a channel is relatively small, the surface tension (and the wetting) has a strong influence on the behavior of the melt stream and furthermore on the quality of the cast product.

## 2 Oscillating Drop Technique

The radius  $R(\vartheta, \varphi, t)$  of the oscillating sample as a function of  $\vartheta$  theta,  $\varphi$  phi, and time  $t$  is represented mathematically by the sum over the corresponding spherical harmonics  $Y_l^m$ :

$$R(\vartheta, \varphi, t) = \sum_l \sum_{m=-l}^{m=l} a_{l,m}(t) \cdot Y_l^m(\vartheta, \varphi), \quad (1)$$

where  $a_{l,m}$  is the time-dependent amplitude of disturbance and  $Y_l^m$  the real spherical harmonics defined by the Legendre polynomials  $P_l^m(\cos \vartheta)$  [5].

The surface tension as the restoring force determines the surface oscillations of a liquid drop around its equilibrium shape. The surface tension  $\gamma$  of non-rotating spherical specimens is calculated from the surface oscillation frequencies  $\nu_R$  and the mass  $M$  by:

$$\gamma = \frac{3}{8} \pi M \nu_R^2. \quad (2)$$

The degenerated five-folded Rayleigh frequency  $\nu_R$  splits in up to five separate frequencies  $\nu_{2,0}$ ,  $\nu_{2,\pm 1}$ , and  $\nu_{2,\pm 2}$  for rotating aspherical specimens, as observed under terrestrial conditions. The frequencies  $\nu_{2,\pm 1}$  and  $\nu_{2,\pm 2}$  depend on the rotation frequency  $\Omega$  and the index  $m$  and split up symmetrically [6]:

$$\nu_{2,\pm m}(\Omega) = \nu_{2,\pm m} \pm |m|\Omega. \quad (3)$$

Corrections for terrestrial conditions (gravity) are given by [7]:

$$\gamma = \frac{3}{8} \pi M \left( \nu_2^2 - \nu_\tau^2 \left( 1.9 + 1.2 \frac{z_0^2}{R^2} \right) \right), \quad (4)$$

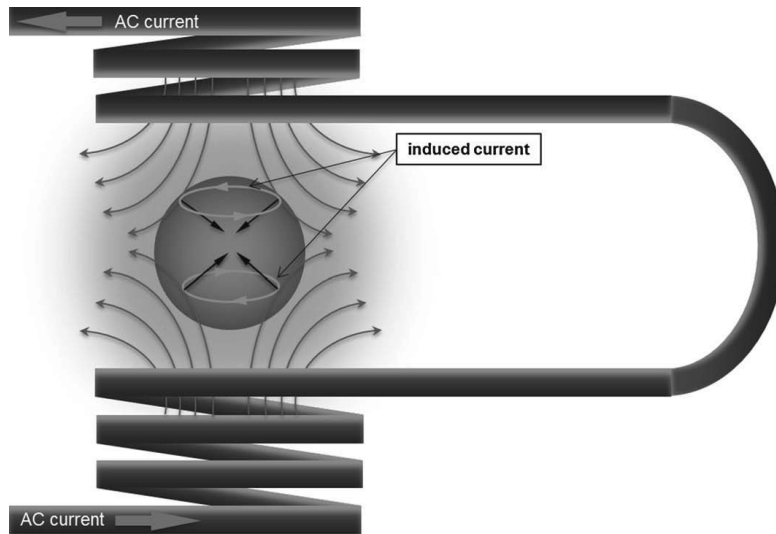


**Fig. 1** A sketch of the levitation coil, the AC and the eddy currents, and the magnetic field lines

with

$$z_0 = \frac{g}{2(2\pi\nu_\tau)^2}, \quad (5a)$$

$$\nu_\tau^2 = \frac{1}{3} \sum_{m=-1}^1 \nu_{1,m}^2, \quad (5b)$$

$$\nu_2^2 = \frac{1}{5} \sum_{m=-2}^2 \nu_{2,m}^2, \quad (5c)$$

where  $R$  is the radius of the specimen and  $g$  the gravitational acceleration. Egry et al. [2] have shown the validity of these correction terms comparing experiments in space and on earth.

### 3 Experimental

The setup consists of an experimental chamber with the levitation coil and optical windows, a radio frequency current generator, vacuum pumps and gas supply, a high-speed camera, and a near-infrared pyrometer. Figure 1 shows a sketch of the levitation coil. An AC current with a frequency of approximately 400 kHz is flowing through the water-cooled levitation coil; a high-frequency electromagnetic field builds up between top and bottom part of the coil. Due to the induced eddy current in the metallic specimen and the interaction with the electromagnetic field, the sample starts to levitate and to heat simultaneously.

The top-view projection of the levitating liquid specimen is recorded by a high-speed camera (EoSens CL, Mikrotron GmbH, Unterschleissheim, Germany) at a rate of 600 frames per second. The chosen spatial resolution is  $1024 \times 1024$ , and the

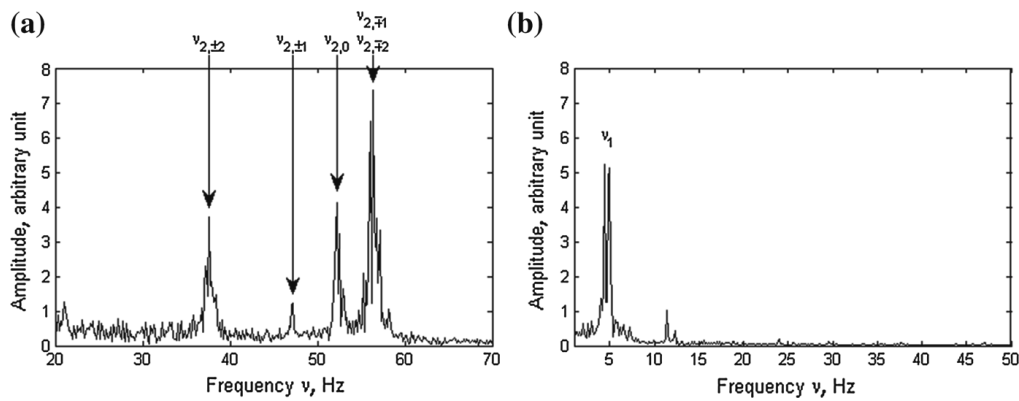


**Fig. 2** (a) spectrum of the oscillation frequencies with  $l = 2$  (Fourier transform of the radius at a fixed azimuthal angle as a function of time) and (b) spectrum of the translation frequencies  $l = 1$  (Fourier transform of the samples center of mass)

gray value dynamics is 8-bit. Temperature of the specimen is measured by a pyrometer (IMPAC IGA 6 ADVANCED, LumaSense Technologies GmbH, Frankfurt/Main, Germany) in the spectral range of  $1.45 \mu\text{m}$ – $1.8 \mu\text{m}$ . The liquidus temperature is measured by differential thermal analysis (DTA) and assigned to the melting plateau in the pyrometer signal. Temperature was determined with the assumption of a constant emissivity in the liquid phase.

The experimental chamber is evacuated to  $10^{-6}$  mbar and subsequently filled with a mixture of argon and 2.4 % hydrogen at a pressure of 400 mbar above atmospheric pressure. The radio frequency current generator is provided by TRUMPF Huettinger GmbH + Co. KG (Freiburg, Germany). A more detailed description of the measurement system is given in [8,9].

The sample material is industrial brass (Cu–5Sn–1Zn); the Zn was evaporated in advance of the measurements. A chemical analysis by optical ICP emission spectroscopy (apparatus: Vista-MPX, Varian, Palo Alto, CA, U.S.A.) after acid hydrolysis showed a mass content of 4.77 wt% Sn and 0.98 wt% Zn before levitation, and 4.63 wt% Sn and 0.03 wt% Zn after the experiment. Measurements were taken with two individual specimens with a mass of about 400 mg.

All individual recorded top-view projections of the specimen are analyzed the following way: (i) scanning of the image using a threshold gray value to distinguish between the specimen and the background, and so to determine the shape of the specimen; (ii) computing the center of mass; (iii) determination of the radii as a function of azimuthal angle. The variation of the radius at fixed azimuthal angles as a function of time undergoes a Fourier transform.

Figure 2a shows an example of a measured spectrum with the surface oscillation modes  $l = 2$  as obtained by Fourier transform of the measured specimen radius as function of time. In contrast to the expected five frequencies  $\nu_{2,0}$ ,  $\nu_{2,\pm 1}$ , and  $\nu_{2,\pm 2}$ , only four peaks are visible. Obviously, two peaks coincide; this requires a more detailed treatment of the spectrum for a correct designation, which is given below, following a similar procedure as in [1].

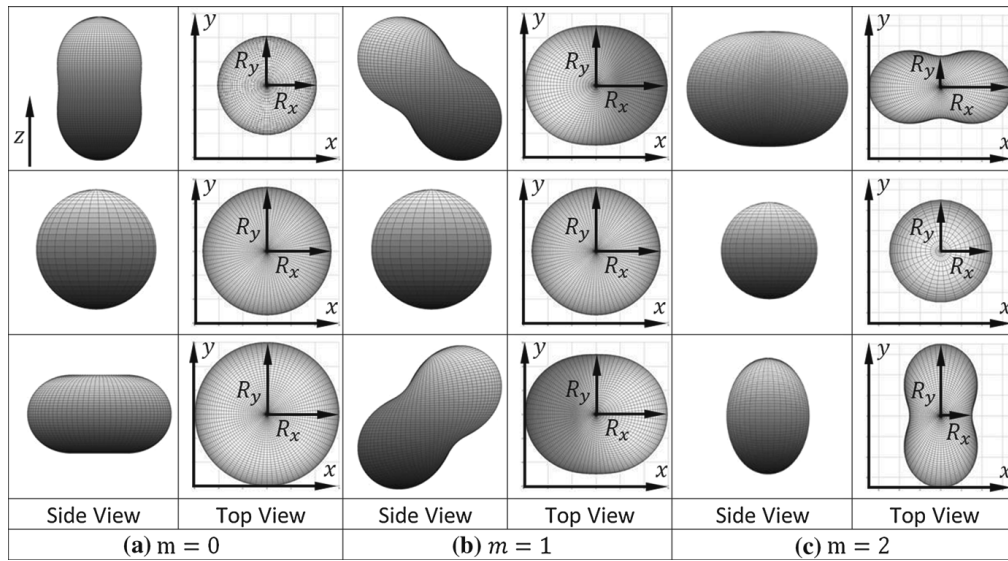


**Fig. 3** Oscillation modes with  $l = 2$  and (a)  $m = 0$ , (b)  $m = 1$ , (c)  $m = 2$

Figure 2a shows the translation frequencies used for the correction term in Eq. 4 obtained by Fourier transform of the determined center of mass of the measured specimen.

Figure 3 shows the oscillation modes with  $l = 2$  and  $m = 0, \pm 1, \pm 2$  ( $\nu_{2,0}$ ,  $\nu_{2,\pm 1}$ , and  $\nu_{2,\pm 2}$ ) in side and top view.  $R_x$  and  $R_y$  are two arbitrarily chosen orthogonal radii.

$R^+$  and  $R^-$  are defined as the sum and difference of two (arbitrary) orthogonal radii  $R_x$  and  $R_y$ :

$$R^+ = R_x + R_y, \tag{6a}$$

$$R^- = R_x - R_y. \tag{6b}$$

As the oscillation mode  $l = 2$  and  $m = 0$  is rotationally symmetric around the  $z$ -axis,  $R^-$  is equal to zero for this mode (see Fig. 3a). Therefore, the Fourier transform of  $R^-$  does not show the oscillation frequency  $\nu_{2,0}$ .

It can be shown that  $R^+$  is a constant value for the oscillation mode  $l = 2$  and  $m = \pm 2$ . By setting  $\vartheta$  equal to  $\pi/2$  in Eq. 1, the orthogonal projection on the  $XY$ -plane ( $R_{xy,l=2,m=\pm 2}$ ) for the oscillation modes with  $l = 2$  and  $m = \pm 2$  is obtained.  $R_{xy,l=2,m=2}$  is shown in Fig. 3c and described by:

$$R_{xy,l=2,m=2}(\varphi, t) = R_{l=2,m=2} \left( \frac{\pi}{2}, \varphi, t \right) = a_0 + 3a_{2,0}(t) \cos 2\varphi, \tag{7a}$$

$$R_{xy,l=2,m=-2}(\varphi, t) = R_{l=2,m=-2} \left( \frac{\pi}{2}, \varphi, t \right) = a_0 + 3a_{2,0}(t) \sin 2\varphi. \tag{7b}$$

From Eq. 7a, the sum of the two orthogonal radii is

$$\begin{aligned} R^+ &= R_{xy,l=2,m=2}(\varphi, t) + R_{xy,l=2,m=2}(\varphi + \pi/2, t) \\ &= a_0 + 3a_{2,0}(t) \cos(2\varphi) + a_0 + 3a_{2,0}(t) \cos(2\varphi + \pi) = 2a_0 = \text{const.} \end{aligned} \tag{8}$$

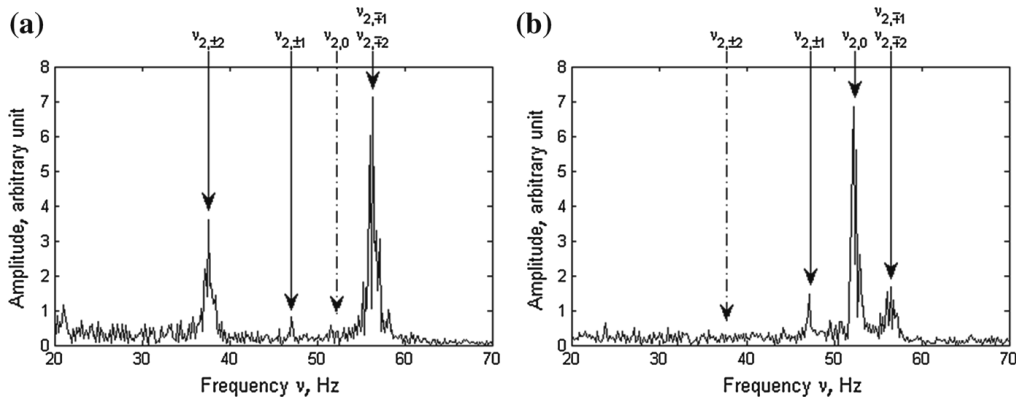


**Fig. 4** (a) Fourier transform of  $R^-$  showing the oscillation frequencies  $\nu_{2,\pm 1}$  and  $\nu_{2,\pm 2}$  and (b) Fourier transform of  $R^+$  showing the oscillation frequencies  $\nu_{2,0}$  and  $\nu_{2,\pm 1}$

Analogously  $R^+$  is also constant for  $R_{xy,l=2,m=-2}$ . Figure 4a shows the Fourier transformation of  $R^-$ . Four peaks ( $\nu_{2,\pm 1}$ ,  $\nu_{2,\pm 2}$ ) are expected to be present (one is equal to zero at frequency  $\nu_{2,0}$ ), but only three oscillation frequencies can be seen.

The Fourier transformation of  $R^+$  (Fig. 4b) shows all three expected peaks ( $\nu_{2,0}$  and  $\nu_{2,\pm 1}$ ). The oscillation frequency  $\nu_{2,0}$  is the missing peak of Fig. 4a. The oscillation frequencies  $\nu_{2,\pm 1}$  are now obtained from Fig. 4b. The disappearing frequency in Fig. 4b has to be one of the oscillating modes with  $l = 2$  and  $m = \pm 2$ .

Taking into account that the distance  $|\nu_{2,2} - \nu_{2,-2}|$  is twice the distance  $|\nu_{2,1} - \nu_{2,-1}|$ , (see Eq. 3), the second oscillating mode with  $l = 2$  and  $m = \pm 2$  overlaps with one of the oscillating modes with  $l = 2$  and  $m = \pm 1$  (Figs. 2a, 4a). All five frequencies are now clearly assigned and can be used to determine the surface tension of Cu–5Sn according to Eq. 4.

## 4 Results

The results of the surface tension of Cu–5Sn as a function of temperature are shown in Fig. 5 in comparison to results of pure copper [8], Cu–8Sn, and Cu–17Sn [10]. The measured values show a linear decrease of surface tension  $\gamma$  with increasing temperature  $T$ . This can be represented in the temperature range 1290 K to 1560 K by a linear fit

$$\gamma(T)(\text{mN}\cdot\text{m}^{-1}) = 1195 - 0.052 \cdot (T - 1318) \quad (9)$$

## 5 Uncertainties

The main contributions to the measurement uncertainty of surface tension are the measurement uncertainty of the oscillation frequencies and the mass. By estimating an uncertainty of 1.5% for the frequencies and 0.2% for the mass, the uncertainty of surface tension is approximately 2%. The measurement uncertainty of temperature is almost negligible due to the small slope of the surface tension versus temperature function.

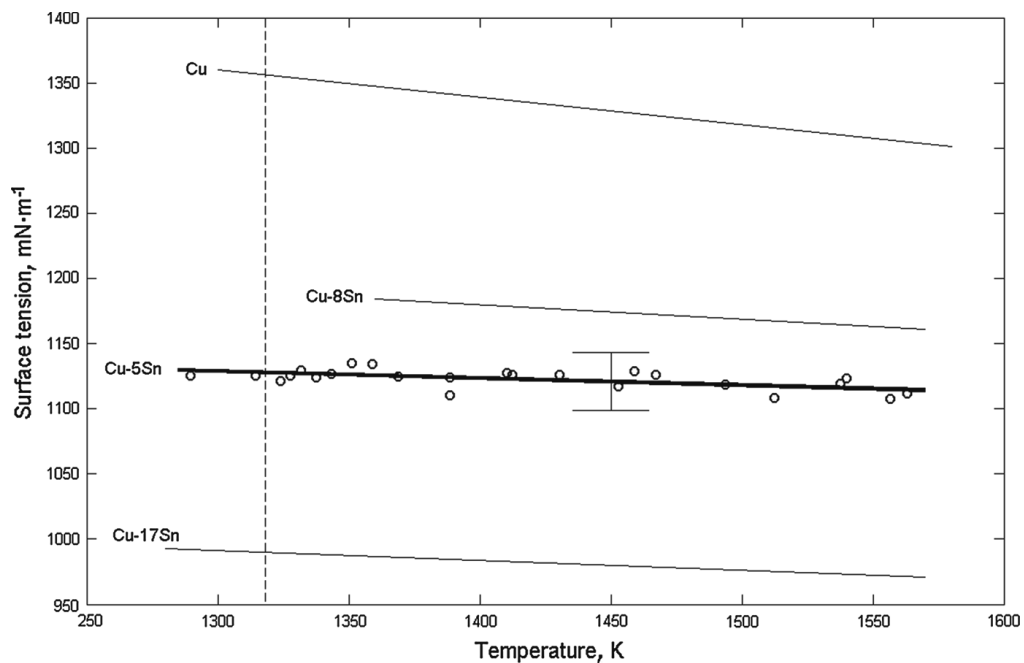


**Fig. 5** Surface tension of Cu–5Sn (copper with 5 wt% tin) as a function of temperature (this work) in comparison to pure copper [8], copper with 8 wt% and 17 wt% tin [10]. The *dashed line* shows the liquidus of Cu–5Sn

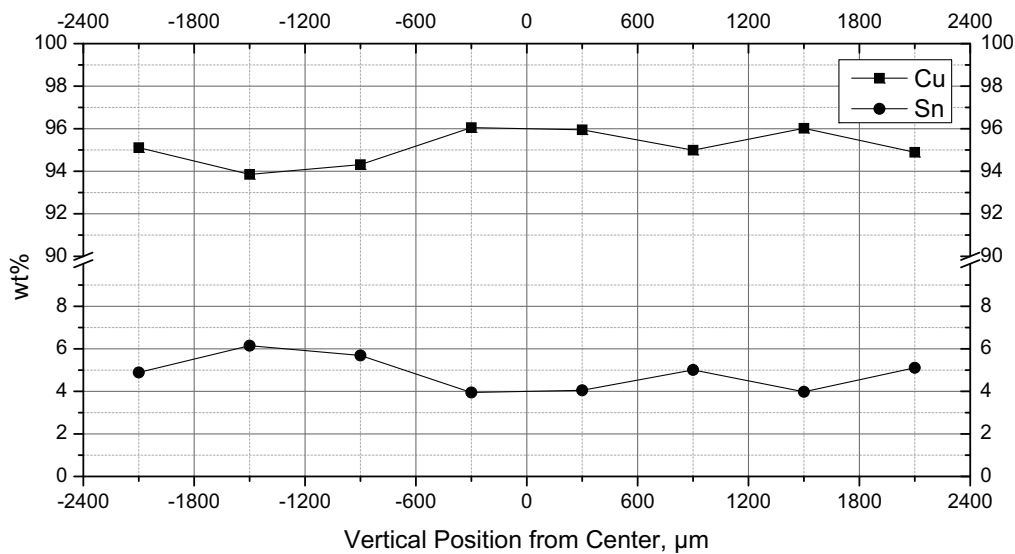


**Fig. 6** Distribution of the chemical composition of copper and tin as a function of radius inside a sample

## 6 Discussion

The surface tension of Cu–Sn alloys is decreasing with an increase of Sn-content. For the compositions Cu–5Sn, Cu–8Sn, and Cu–17Sn, the surface tension is decreasing with increasing temperature. Results of Amore et al. [10] show slightly higher results than our result for Cu–5Sn. This may be due to high sensitivity of the surface tension

to impurities and segregation. It should be noted that this work was performed with industrial brass, whereas [10] uses high purity melt. Furthermore no information on oxygen content is given in this work as well as in [10].

Large differences in surface tension, atom radius, and electron configuration between the individual substances can lead to segregation. As the surface tension of copper is significantly higher than the surface tension of tin (approximately three times higher), a lower concentration of tin in the center of the sample and a higher concentration at the surface could be expected. Fortunately, mixing occurs which is caused by the turbulent flow of the Cu–5Sn melt, due to the eddy currents. The radial distribution of the chemical composition inside the sample (Fig. 6) was measured by scanning electron microscopy using energy dispersive x-ray spectroscopy (SEM: Zeiss Ultra55, EDX: EDAX Pegasus, at 20 keV acceleration voltage). Within the measurement uncertainties, no segregation can be observed inside the sample.

**Acknowledgments** This work was supported by Austrian Science Fund (FWF), Vienna, Austria under Contract No. P23838-N20.

## References

1. S. Sauerland, K. Eckler, I. Egry, *J. Mater. Sci. Lett.* **11**, 330–333 (1992)
2. I. Egry, G. Lohoefer, G. Jacobs, *Phys. Rev. Lett.* **75**, 4043–4046 (1995)
3. W.K. Rhim, K. Ohsaka, *J. Chem. Thermodyn.* **32**, 123–133 (2000)
4. J. Brillo, I. Egry, *J. Mater. Sci.* **40**, 2213–2216 (2005)
5. I.N. Bronstein, K.A. Semendjajew, *Taschenbuch der Mathematik* (Wissenschaftlicher Verlag Harri Deutsch GmbH, Frankfurt am Main, 2008), p. 189
6. I. Egry, H. Giffard, S. Schneider, *Meas. Sci. Technol.* **16**, 426–431 (2005)
7. D.L. Cummings, D.A. Blackburn, *J. Fluid Mech.* **224**, 395–416 (1991)
8. K. Aziz, A. Schmon, G. Pottlacher, *High Temp. High Press.* **43**, 193–200 (2014)
9. K. Aziz, A. Schmon, G. Pottlacher, *High Temp. High Press.* (in press)
10. S. Amore, E. Ricci, T. Lanata, R. Novakovic, *J. Alloys Compd.* **452**, 161–166 (2008)

## 6.2 Measurement of surface tension of liquid nickel by the oscillating drop technique

K. Aziz, A. Schmon, and G. Pottlacher. Measurement of surface tension of liquid nickel by the oscillating drop technique. *High Temperatures-High Pressures*, 44:475–481, 2015.

This publication discusses the surface tension measurement of nickel. The surface tension of nickel was measured using an electromagnetic levitation setup constructed by me at Graz University of Technology. A comparison of data measured in this study and data from literature is given within this publication.

### Comments:

The entire publication was written by me. The surface tension of nickel was measured by me. The density of nickel in the liquid phase was measured by A. Schmon and me. A. Schmon was my coworker and G. Pottlacher was my supervisor in this project. They were involved in all decisions, especially regarding the final text revisions.

*High Temperatures-High Pressures*, Vol. 44, pp. 475–481  
Reprints available directly from the publisher  
Photocopying permitted by license only

©2015 Old City Publishing, Inc.  
Published by license under the OCP Science imprint,  
a member of the Old City Publishing Group

## Measurement of surface tension of liquid nickel by the oscillating drop technique

K. AZIZ\*, A. SCHMON AND G. POTTLACHER

*Institute of Experimental Physics, Graz University of Technology, NAWI Graz  
Petersgasse 16, 8010 Graz, Austria*

*Received: January 12, 2015. Accepted: March 17, 2015.*

The oscillating drop technique is a well-established method for the measurement of surface tension. In this work an electromagnetic levitation device is used to measure the surface tension of nickel by means of the oscillating drop technique.

An electromagnetic levitation device employs an inhomogeneous radio-frequency electromagnetic field inside a levitation coil to heat and position the specimen. Induced eddy currents heat up the material into the liquid phase and exert a Lorentz force, pushing it towards regions of lower field strength. The levitating specimen is investigated by optical setups to provide a contactless measurement.

Investigations of nickel have been carried out by the thermophysics and metalphysics group at TU Graz. The temperature dependence of the surface tension presented in this work is

$$\gamma(T) = 1864 - 0.35 \cdot (T - 1728) \text{ mN m}^{-1}$$

in the temperature range from 1700 K to 2020 K.

*Keywords:* Surface tension, liquid nickel, oscillating drop, electromagnetic levitation

### 1 INTRODUCTION

There are different methods to measure surface tension of liquid metals. In the current work the oscillating drop (OD) technique in combination with an electromagnetic levitation device is used to determine the surface tension of

---

\*Corresponding author: k.aziz@tugraz.at

nickel and is compared to previous publications [1–9]. As liquid metals are very reactive a container-less method, like electromagnetic or -static levitation, is preferred for investigation. Despite its limitation, resulting from a possible contamination of the specimen during the experiment, sessile drop (SD) and maximum bubble pressure (MBP) techniques are also quite common methods for surface tension measurements [6–10].

## 2 MEASUREMENT TECHNIQUES

### 2.1 Sessile Drop method (SD) and Maximum Bubble Pressure method (MBP)

As some of the references mentioned in this paper use the sessile drop and maximum bubble pressure method for investigating the surface tension of liquid nickel, the principle of these two methods are shortly mentioned here. Figure 1 shows an illustration of these setups. More detailed information is found in the literature [6–10].

Sessile Drop is a popular method to determine the surface tension of liquid metals. It is determined by measuring the geometry of the drop (Figure 1(a)). The experimental difficulty of SD is to ensure, that no contamination of the specimen by the substrate occurs during the investigation.

Figure 1(b) illustrates the maximum bubble pressure technique. A capillary tube of known radius is immersed in the fluid of interest. By increasing the gas pressure in the tube, a bubble is produced. This method allows to determine the surface tension by measuring the pressure inside the tube. A major advantage of this method is that for each measurement a new uncontaminated surface is created.

### 2.2 Oscillating Drop method (OD)

The oscillating drop method in combination with a levitation technique (like electromagnetic or electrostatic levitation) is an elegant method to determine the surface tension of liquid metals. The thermophysics and metalphysics

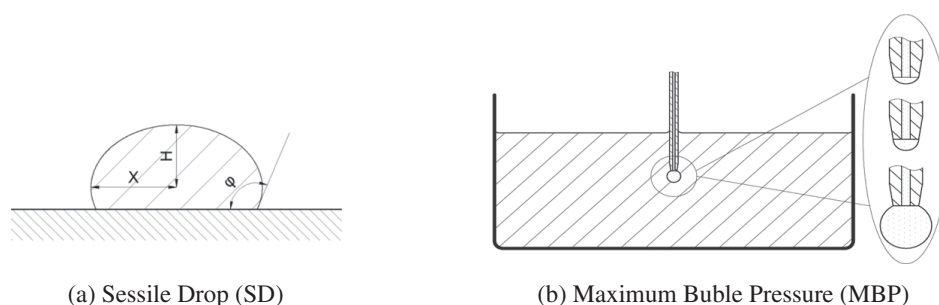


FIGURE 1  
Illustration of the sessile drop (a) and maximum bubble pressure technique (b).

group at TU Graz uses an electromagnetic levitation device setup for surface tension measurements. This technique is a container-less method guaranteeing contactless measurement of liquid metals. Hence contamination through a mechanical contact is avoided and the investigation of undercooled liquid metals is also possible. To reduce oxygen solved in the nickel specimen, surface tension measurements were carried out under a high-purity  $He/H_2$  atmosphere with 4 volume percent hydrogen. As the equilibrium constant for the reaction



is very large (equilibrium constant  $\gg 1$ ), the deoxidization of nickel is very effective.

Figure 2 shows an illustration of the setup. To determine the surface tension as a function of temperature, the specimen is investigated by a high-speed camera and a pyrometer. The high-speed camera takes up to 600 fps (frames per second) at a resolution of  $1024 \times 1024$ . The pyrometer performing the temperature measurements is the IMPAC IGA 6 ADVANCED by LumaSense Technologies, with measuring range of  $250^\circ\text{C} - 2500^\circ\text{C}$  and spectral range of  $1.45 \mu\text{m} - 1.8 \mu\text{m}$ . The geometry of the specimen is determined by edge detection algorithms.

The underlying concept of the oscillating drop technique is that the surface oscillations of the liquid drop around its equilibrium shape can be related to surface tension as the restoring force. Lord Rayleigh postulated a formula in 1879 [12] relating the surface tension  $\gamma$  of a non-rotating, forceless, spherical specimens to its surface oscillation frequencies  $\nu_R$  and its mass  $M$ :

$$\gamma = \frac{3}{8} \pi M \nu_R^2 \quad (2)$$

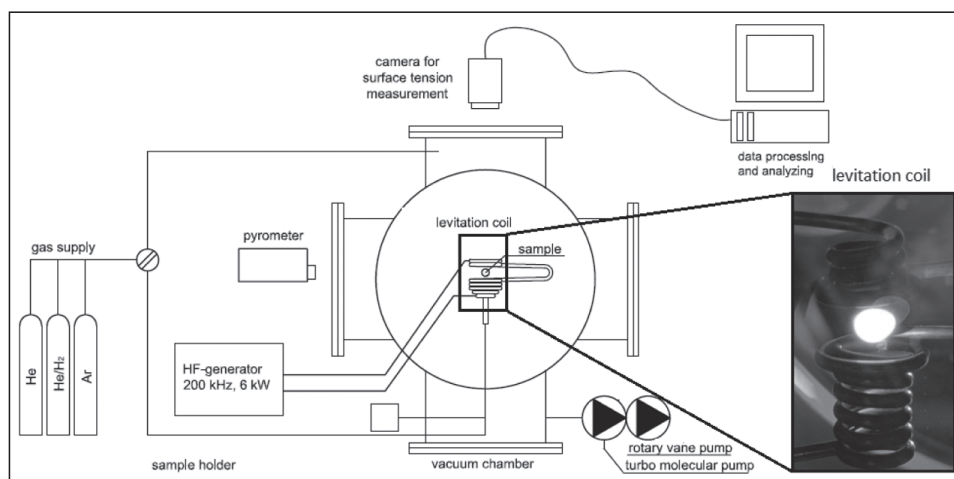


FIGURE 2  
An illustration of the setup used for this study [11].

Contrary to this forceless case, where all five possible fundamental surface oscillation modes of the liquid sample show the same Rayleigh frequency, the frequency of the modes for rotating, aspherical specimens, deformed in terrestrial levitation experiments by its own weight (Figure 3), splits in up to five different frequencies  $v_{2,0}$ ,  $v_{2,\pm 1}$  and  $v_{2,\pm 2}$  (Figure 4). In 1991 corrections for the Rayleigh frequency were suggested by Cummings and Blackburn [13] to achieve the same results for terrestrial levitation experiments and experiments in microgravity:

$$v_R^2 = v_2^2 - v_\tau^2 \left( 1.9 + 1.2 \frac{z_0^2}{R^2} \right), \quad (3)$$

with

$$z_0 = \frac{g}{2 (2\pi v_\tau)^2} \quad (4)$$

$$v_\tau^2 = \sum_{m=-1}^1 v_{1,m}^2 \quad (5)$$

$$v_2^2 = \frac{1}{5} \sum_{m=-2}^2 v_{2,m}^2 \quad (6)$$

where  $R$  is the radius of the specimen and  $g$  the gravitational acceleration.

By performing the Fourier transformation of the center of mass  $CM$  and the Radius  $R_x$  or  $R_y$  (Figure 3) we get the translation (Figure 4 (a)) and oscillation frequencies (Figure 4 (b)).

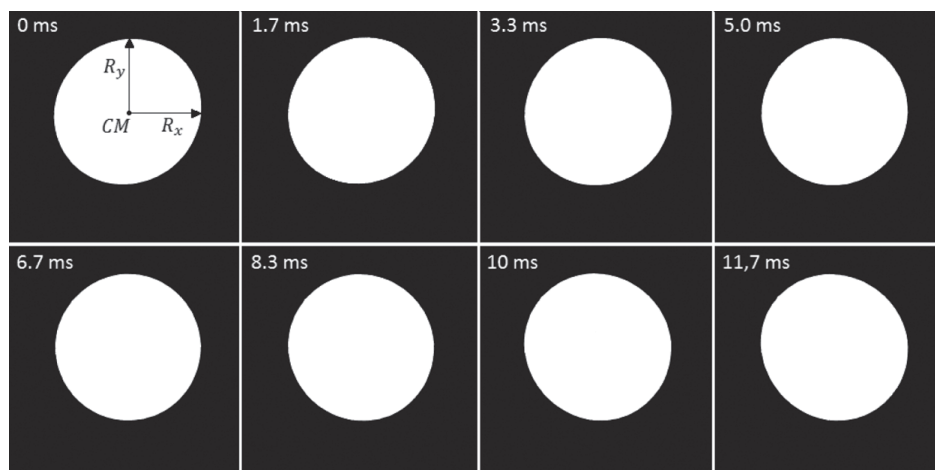


FIGURE 3

Pictures of the levitating specimen taken with a high-speed camera (600 fps).  $CM$  is the center of mass. The radius  $R_x$  and  $R_y$  are orthogonal to each other.

## MEASUREMENT OF SURFACE TENSION OF LIQUID NICKEL

479

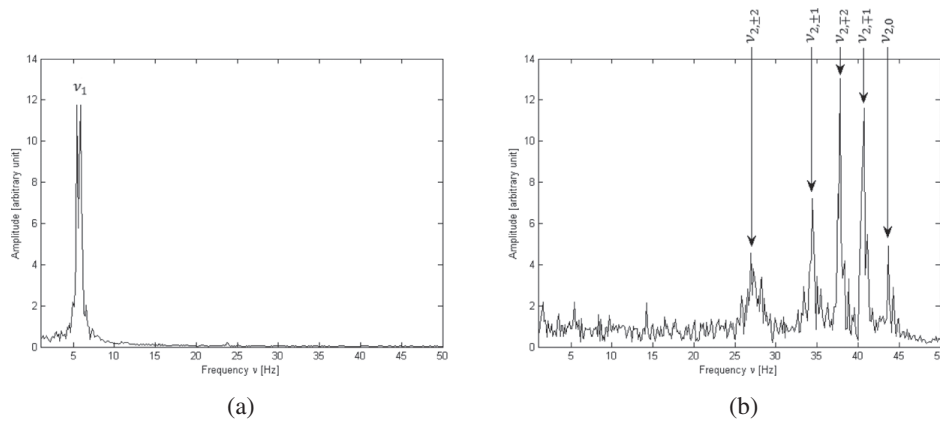


FIGURE 4  
 (a) Translation frequencies (oscillation modes with  $l = 1$ ) and (b) oscillation frequencies with  $l = 2$  of liquid nickel.

## 3 RESULTS AND DISCUSSION

In this study nickel specimens with a purity of 99.995% (Alfa Aesar, LOT: L29x008) and masses (1.241 g, 1.180 g and 1.172 g) were investigated between 1700 K and 2020 K. Our experimental results are shown in Figure 5 and compared to literature values. The measuring points in Figure 5 deliver a

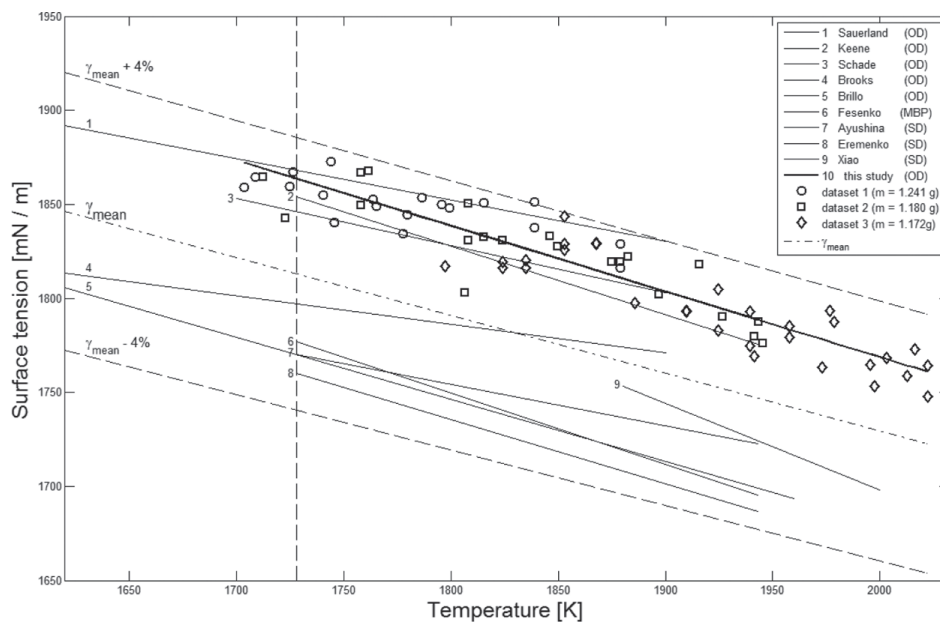


FIGURE 5  
 Surface tension of nickel. Previously published data and the result of this study.  $\gamma_{mean}$  is the mean of the measurements listed in Table 1 and plotted in this Figure. Measuring techniques: Oscillating Drop (OD), Sessile Drop (SD), and Maximum Bubble Pressure (MBP).

480

K. AZIZ *et al.*

TABLE 1

Surface tension of nickel  $\gamma(T) = \gamma(T_m) + \frac{\Delta\gamma}{\Delta T} \cdot (T - T_m)$  with  $T_m = 1728\text{ K}$  as melting temperature of nickel [14]. Measuring techniques: Oscillating Drop (OD), Sessile Drop (SD), and Maximum Bubble Pressure (MBP).

#	$\gamma(T_m)$ [ $mN\ m^{-1}$ ]	$\frac{\Delta\gamma}{\Delta T}$ [ $mN\ m^{-1}\ K^{-1}$ ]	Method	Reference
1	1868	-0.22	OD	[1]
2	1854	-0.36	OD	[2]
3	1846	-0.25	OD	[3]
4	1797	-0.15	OD	[4]
5	1770	-0.33	OD	[5]
6	1777	-0.38	MBP	[6]
7	1770	-0.22	SD	[7]
8	1760	-0.34	SD	[8]
9	1823	-0.46	SD	[9]
10	1864	-0.35	OD	this study

linear decrease of the surface tension with temperature. In the temperature range from 1700 K to 2020 K the linear fit is:

$$\gamma(T) = 1864 - 0.35 \cdot (T - 1728)\ mN\ m^{-1}$$

Surface tension is very sensitive regarding to impurities, especially to surface active elements as oxygen. Even small amounts of impurity lead to a contamination of the specimen. Nevertheless the data plotted in Figure 5 fit quite well within a deviation of 4%.  $\gamma_{mean}$  is the mean of the measurements listed in Table 1. To get more accurate measurements, one has to provide a clean environment.

#### 4 UNCERTAINTIES

The uncertainty of temperature is estimated to be about  $\pm 10\text{ K}$  originating from inaccurate determination of the liquidus temperature and the temperature dependence of emissivity. The uncertainty of surface tension is due to the inaccurate measurement of oscillation frequency.  $\Delta\gamma$  is about 2%.

The standard deviation of surface tension at melting temperature is  $3\ mN\ m^{-1}$  and for the slope  $0.02\ mN\ m^{-1}\ K^{-1}$ :

$$\gamma(T) = (1864 \pm 3) - (0.35 \pm 0.02) \cdot (T - 1728)\ mN\ m^{-1}$$

## ACKNOWLEDGEMENT

We are very grateful for the exchange of scientific equipment and know-how between Institute of Materials Physics in Space, German Aerospace Center (DLR), Linder Höhe, 51147 Köln, Germany and Institute of Experimental Physics, Graz University of Technology, NAWI Graz Petersgasse 16, 8010 Graz.

This research is funded by the Austrian Science Fund (FWF): FWF Project P 23838-N20.

## REFERENCES

- [1] Sauerland, S.; Eckler, K. & Egry, I., *High-precision surface tension measurements on levitated aspherical liquid nickel droplets by digital image processing*, Journal of materials science letters, Springer, 1992, 11, 330–333.
- [2] Keene, B.; Mills, K. & Brooks, R., *Surface properties of liquid metals and their effects on weldability*, Materials science and technology, Maney Publishing Suite 1C, Joseph's Well, Hanover Walk, Leeds LS3 1AB, UK, 1985, 1, 559–567.
- [3] Schade, J.; McLean, A. & Miller, W., *Surface tension measurements on oscillating droplets of undercooled liquid metals and alloys*, Undercooled Alloy Phases, 1986, 233–248.
- [4] Brooks, R. F. & Mills, K. C., *Measurement of the thermophysical properties of melts by a levitated-drop method*, High Temperatures-High Pressures, Pion, 1993, 25, 657–664.
- [5] Brillo, J. & Egry, I., *Surface tension of nickel, copper, iron and their binary alloys*, Journal of materials science, Springer, 2005, 40, 2213–2216.
- [6] Fesenko, V. & Vasiliu, M., *Temperature dependence of the surface tension of cobalt and nickel*, Poroshkovaya Metallurgiya, 1961, 25–27.
- [7] Ayushina, G.; Levin, E. & GELD, P., *Density and surface energy of liquid alloys of aluminium with cobalt and nickel*, Russian Journal of physical chemistry, USSR, Interperiodica PO BOX 1831, Birmingham, AL 35201–1831, 1969, 43, 1548.
- [8] Eremenko, V. & Nizhenko, V., *Surface properties of liquid alloys Ni-Au-Al 2 O 3*, Zh. Neorg. Khim, 1963, 8, 2124–2127.
- [9] Xiao, F.; Liu, L.-X.; Yang, R.-H.; Zhao, H.-K.; Fang, L. & Zhang, C., *Surface tension of molten Ni-(Cr, Co, W) alloys and segregation of elements*, Transactions of Nonferrous Metals Society of China, Elsevier, 2008, 18, 1184–1188.
- [10] A. W. Adams & A P. Gast, *Physical chemistry of surfaces 6<sup>th</sup> Edition*, Wiley-Interscience Publication, New York, 1997.
- [11] Aziz, K.; Schmon, A. & Pottlacher, G., *Measurement of surface tension of liquid copper by means of electromagnetic levitation*, High Temperatures-High Pressures, 2014, 43.
- [12] Lord Rayleigh, *On the capillary phenomena of jets*, Proceedings of the Royal Society of London, Vol. 29, p. 71–97, 1879.
- [13] D. L. Cummings & D. A. Blackburn, *Oscillations of magnetically levitated aspherical droplets*, J. Fluid Mech. 224, p. 395–416, 1991.
- [14] D. R. Lide, *CRC Handbook of Chemistry and Physics*, CRC Press, 88<sup>th</sup> edition, 2007.

### 6.3 Measurement of surface tension of liquid copper by means of electromagnetic levitation

K. Aziz, A. Schmon, and G. Pottlacher. Measurement of surface tension of liquid copper by means of electromagnetic levitation. *High Temperatures-High Pressures*, 43:193–200, 2014.

This publication discusses the first results for surface tension using the electromagnetic levitation setup constructed by me at Graz University of Technology. A comparison of data measured in this study and data from literature is given within this publication, confirming the good agreement of our data with data from literature.

#### Comments:

The entire publication was written by me. The surface tension of copper was measured by me. The density of copper in the liquid phase was measured by A. Schmon and me. A. Schmon was my coworker and G. Pottlacher was my supervisor in this project. They were involved in all decisions, especially regarding the final text revisions.

*High Temperatures-High Pressures*, Vol. 43, pp. 193–200  
Reprints available directly from the publisher  
Photocopying permitted by license only

©2014 Old City Publishing, Inc.  
Published by license under the OCP Science imprint,  
a member of the Old City Publishing Group

## Measurement of surface tension of liquid copper by means of electromagnetic levitation

K. AZIZ\*, A. SCHMON AND G. POTTLAGHER

*Institute of Experimental Physics, Graz University of Technology,  
Petersgasse 16, 8010 Graz, Austria*

*Received: September 26, 2013. Accepted: October 30, 2013.*

An electromagnetic levitation device has been recently constructed by the thermophysics and metalphysics group at TU Graz, Austria and first investigations of copper in the liquid phase have been carried out. Data for temperature dependence of surface tension will be presented in this work and compared to results from literature.

The value obtained for surface tension in this work is:

$$\gamma = (1633 - 0.21 \cdot T) \text{ mN m}^{-1}$$

With temperature  $T$  between  $1400 \text{ K} \leq T \leq 1750 \text{ K}$ .

*Keywords:* Surface tension, Liquid copper, Oscillating drop, Electromagnetic levitation.

### 1 INTRODUCTION

As liquid metals are very reactive, a contact-free measurement technique is necessary. Electromagnetic levitation provides a containerless method for surface tension measurement of metallic melts. Currently such an apparatus has been constructed by the thermophysics and metalphysics group at TU Graz, Austria.

In an electromagnetic levitation device an inhomogeneous high-frequency electromagnetic field is built up inside the levitation coil (Fig. 1) to heat and position the sample. Induced eddy currents heat the material into the liquid phase and exert a Lorentz force, pushing it towards regions of lower field

---

\*Corresponding author: k.aziz@tugraz.at



FIGURE 1  
The levitation coil and a levitated sample.

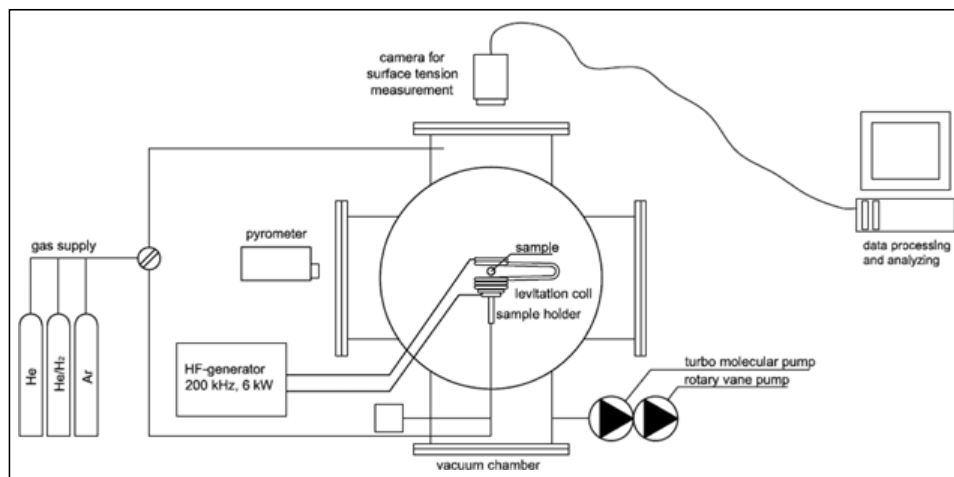


FIGURE 2  
Illustration of the set-up used for this study.

strength and so the sample begins to levitate. The sample is investigated by a high-speed camera and a pyrometer to determine surface tension as a function of temperature. The high-speed camera used takes up to 600 fps (frames per second) at a resolution of  $1024 \times 1024$ . The pyrometer used is IMPAC IGA 6 ADVANCED by LumaSense Technologies, with measuring range of  $250^{\circ}\text{C} - 2500^{\circ}\text{C}$  and spectral range of  $1.45 \mu\text{m} - 1.8 \mu\text{m}$ .

The sample is levitated in a special self-designed levitation coil (Fig. 1), as suggested by German Aerospace Center (DLR). The design has to be adapted, depending on the investigated material. A high frequent current, which is supplied by a HF-generator, runs through the levitation coil. The coil is water-cooled to protect it from melting. Fig. 2 shows an illustration of the set-up. The levitated sample is placed in the levitation coil inside a vacuum chamber

with glass windows for various types of optical diagnostics such as a high-speed camera to monitor the sample shape and a pyrometer for temperature measurements. So thermophysical properties like surface tension can be obtained contactless as a function of temperature for metals in the liquid phase. The mass of the sample is measured at the beginning and at the end of the experiment and is interpolated for the determination of the surface tension.

## 2 MEASUREMENT PRINCIPLES

As the gravitational force is canceled out only for certain regions, the liquid sample would melt away, if it weren't the surface tension as a restoring force. This leads to an oscillating drop. That's why the electromagnetic levitation technique is also called oscillating drop method.

The shape of the oscillating sample as a function of time can be described by the spherical harmonics  $Y_l^m$ . The Radius  $R(\vartheta, \varphi, t)$  is represented mathematically by the sum over the corresponding spherical harmonics [1]:

$$R(\vartheta, \varphi, t) = \sum_l \sum_{m=-l}^{m=l} \alpha_{l,m}(t) \cdot Y_l^m(\vartheta, \varphi) \quad (1)$$

where  $\alpha_{l,m}$  is the time dependent amplitude of disturbance and  $Y_l^m$  the real spherical harmonics defined by the Legendre polynomials  $P_l^m(\cos\vartheta)$  [2]:

$$Y_l^m(\vartheta, \varphi) = P_l^m(\cos\vartheta) \cos(m\varphi) \quad \text{for } m \geq 0 \quad (2a)$$

$$Y_l^m(\vartheta, \varphi) = P_l^{-m}(\cos\vartheta) \cos(-m\varphi) \quad \text{for } m < 0 \quad (2b)$$

The oscillation mode with the index  $l = 0$  corresponds to an expansion and contraction of the sample. As we assume to deal with non-compressible fluids, no deformation with  $l = 0$  will occur.

For  $l = 1$  it can be shown mathematically, that for small amplitudes it leads only to translation of the sample and practically no deformation is observed.

The oscillation modes with  $l = 2$  are shown in Fig. 3. These oscillations are interesting for the determination of the surface tension.

Oscillation modes with  $l \geq 3$  deliver small amplitudes and are neglected here.

As surface tension is the restoring force and therefore the origin of these oscillations, one can assume the existence of a model describing the relation between surface tension and surface oscillation. As a matter of fact Lord Rayleigh postulated a formula in 1879 [4] relating surface tension  $\gamma$  to surface oscillation frequencies  $v_{l,m}$  for non-rotating spherical samples:

$$v_{l,m}^2 = l \cdot (l+2) \cdot (l-1) \frac{8}{3\pi} \frac{\gamma}{M} \quad (3)$$

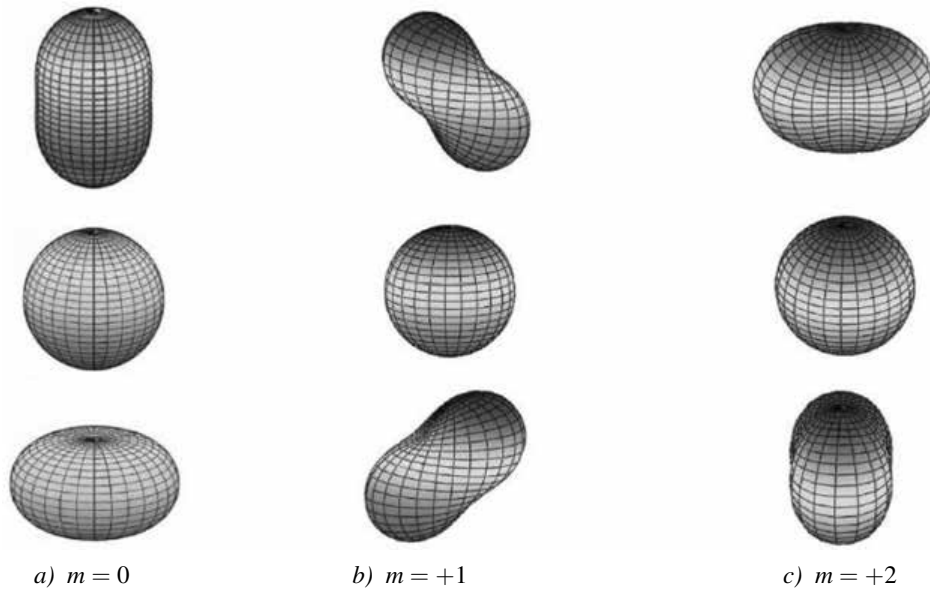


FIGURE 3  
Deformation of the levitated drop for oscillation modes with  $l = 2$  and *a)*  $m = 0$ , *b)*  $m = +1$ , *c)*  $m = +2$ . Figure plotted according to [3, 1].

where  $l$  and  $m$  are the indices of the spherical harmonics and  $M$  is the mass of the sample. Equation 3 does not depend on the index  $m$  and thus the frequencies are degenerated for non-rotating samples in a symmetric force field, causing a spherical equilibrium shape.

The frequency corresponding to  $l = 2$  is called Rayleigh frequency and is five-fold degenerated:

$$v_R^2 = \frac{8}{3\pi} \frac{\gamma}{M} \quad (4)$$

So surface tension is determined by solving the equation (4) for  $\gamma$

$$\gamma = \frac{3}{8} \pi M v_R^2 \quad (5)$$

In Fig. 3 the geometry of the oscillation modes for  $l = 2$  is shown. As mentioned before, the actual shape is described by the sum over the corresponding spherical harmonics (Eq. 1) and in consequence given by the superposition of all oscillation modes.

In terrestrial levitation experiments, gravitational force acts on the liquid sample, leading to distortion of the otherwise spherical equilibrium shape. Because of the broken symmetry and rotation of the sample the degeneracy of surface oscillations split up into maximum  $(2l + 1)$  frequencies.

An inhomogeneous magnetic field is used to realize the levitation of the sample on earth, which leads to a magnetic pressure and to a shift of the frequencies.

In 1991 corrections for the Rayleigh frequency were suggested by Cummings and Blackburn [5] to achieve same results for terrestrial levitation and microgravity experiments. The Rayleigh frequency is determined as follows:

$$v_R^2 = \frac{1}{5} \sum_{m=-2}^2 v_{2,m}^2 - v_\tau^2 \left( 1.9 + 1.2 \frac{z_0^2}{R^2} \right) \quad (6)$$

with

$$z_0 = \frac{g}{2v_\tau^2}$$

and

$$v_\tau^2 = \sum_{m=-1}^1 v_{1,m}^2$$

where  $R$  is the radius of the sample and  $g$  the gravitational acceleration.

The center of mass and the shape of the observed samples are calculated by means of image processing algorithms. The translation and surface oscillation frequencies of the sample are determined by applying a Fast-Fourier-Transformation on the computed data.

The spectrum for the oscillation frequencies of liquid copper is shown in Fig. 4. A peak for the translation mode is observed at the frequency of about 6 Hz. Fig. 4b) shows the interesting oscillation modes for  $l = 2$  in the range of 27 Hz to 40 Hz.

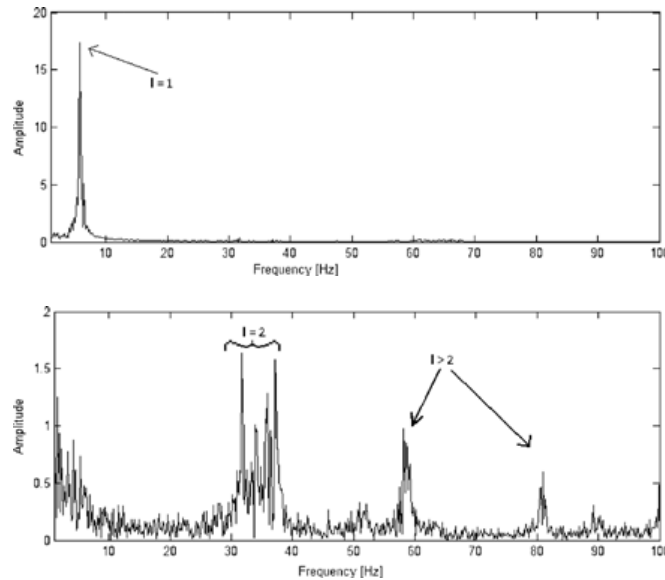


FIGURE 4

(a) Translation frequency and (b) oscillation frequencies with  $l \geq 2$  of liquid copper.

(a) Fourier transformation of the center of mass.

Translation of the sample (oscillation modes with  $l = 1$ ).

(b) Oscillation modes with  $l = 2$  and  $l > 2$ .

### 3 RESULTS AND DISCUSSION

In this section our results on surface tension of copper are presented and compared to previously published data (Fig. 5). Fig. 5 shows the investigations of copper, which are carried out with three different measuring techniques. These are the oscillating drop [6,7,9,10,11], the sessile drop [9,12,13] and the maximum bubble pressure method [8].

For this study copper samples with a purity of 99.9999% and masses between 1 g and 1.3 g were measured. The uncertainty for surface tension is estimated to be  $\pm 4\%$  originating from the resolution of temperature measurement, determined frequencies and sample mass. This estimation is in good agreement with the distribution of the measured values.

In our experiments we get the following dependence of surface tension on temperature for copper:

$$\gamma = (1633 - 0,21 \cdot T) \text{ mN m}^{-1} \quad (7)$$

for the temperature interval  $1400 \text{ K} \leq T \leq 1750 \text{ K}$ .

Our results match well with the result of Keene [7], Nogi (SD) [9], Matsumoto [10], Egry [11] and Morita [12] within the uncertainty of the measurements. The other literature data don't fit with our measurements. They are either too low [13] or the surface tension decreases too fast with temperature [6,8] and Nogi (OD) [9].

There are two main reasons for these deviations. First the degree of impurity of the measured copper samples varies from each other and secondly in

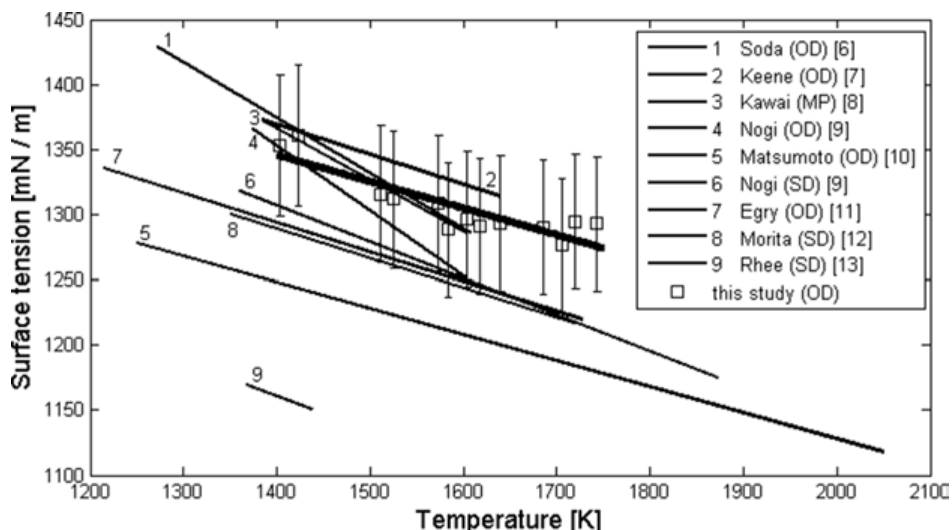


FIGURE 5

Data previously published and the result of this study. Measuring techniques: Oscillating Drop (OD), Sessile Drop (SD), and Maximum bubble pressure (MP).

some experiments the discussed corrections by Cummings and Blackburn were not applied.

As surface tension is very sensitive regarding to impurity, one has to provide a pure raw material and guarantee a clean environment during levitation. Especially oxygen has a huge influence on the measurement and contaminates the raw material [12,14,15]. Although the results of the experiments shown in Fig. 5 were performed under different conditions and surface tension is a very sensible parameter, the results match quite well. To get comparable data, oxygen partial pressure should be measured or at least ensured to be low and the same raw material should be used.

## ACKNOWLEDGEMENT

We are very grateful for the exchange of scientific equipment between Institute of Materials Physics in Space, German Aerospace Center (DLR), Linder Höhe, 51147 Köln, Germany and Institute of Experimental Physics, Graz University of Technology, Petersgasse 16, 8010 Graz.

This research is funded by the Austrian Science Fund (FWF): FWF Project P 23838-N20.

## REFERENCES

- [1] J. Brillo, G. Lohöfer, F. Schmidt-Hohagen, S. Schneider and I. Egry, *Thermophysical property measurements of liquid metals by electromagnetic levitation*, Int. J. Materials and Product Technology, Vol. 26, Nos. 3/4, 2006.
- [2] I. N. Bronstein and K. A. Semendjajew, *Taschenbuch der Mathematik*, Wissenschaftlicher Verlag Harri Deutsch GmbH, Frankfurt am Main, ISBN 978-3-8171-2007-9, 2008.
- [3] H. Fujii, T. Matsumoto and K. Nogi, *Analysis of surface oscillation of droplet under micro-gravity for the determination of its surface tension*, Acta Materialia, Vol. 48, Issue 11, p. 2933–2939, 2000.
- [4] Lord Rayleigh, *On the capillary phenomena of jets*, Proceedings of the Royal Society of London, Vol. 29, p. 71–97, 1879.
- [5] D. L. Cummings and D. A. Blackburn, *Oscillations of magnetically levitated aspherical droplets*, J. Fluid Mech. 224, p. 395–416, 1991.
- [6] H. Soda, A. McLean and W. A. Miller, *Surface tension measurements of liquid copper droplets in the temperature range 1000 to 1330°C*, Trans JIM 18, p. 445–54, 1977.
- [7] B. J. Keene, K. C. Mills, A. Kasama, A. McLean and W. A. Miller, *Parison of surface tension measurements using levitated droplet method*, Metall Trans. B 17, p. 159–62, 1986.
- [8] Y. Kawai, M. Kishimoto and H. Tsuru, *Surface tension and density of liquid Cu–Sn alloys*, J. Japan Inst. Met. 37, p. 668–72, 1973.
- [9] K. Nogi, K. Ogino, A. Mclean and W. A. Miller, *The temperature coefficient of the surface tension of pure liquid metals*, Metall. Trans. B 17, p. 163–70, 1986.
- [10] T. Matsumoto, H. Fujii, T. Ueda, M. Kamai and K. Nogi, *Measurement of surface tension of molten copper using the free-fall oscillating drop method*, Meas. Sci. Technol. 16, p. 432–437, 2005.
- [11] I. Egry, S. Sauerland and G. Jacobs, *Surface tension of levitated liquid noble metals*, High Temp. High Press. 26, p. 217–23, 1994.

200

K. Aziz *et al.*

- [12] Z. Morita and A. Kasama, *Surface tension of liquid copper in dilute oxygen concentrations*, J. Japan Inst. Met. 40, p. 787–95, 1976.
- [13] S. K. Rhee, *Wetting of AlN and TiC by liquid Ag and liquid Cu*, J. Am. Ceram. Soc. 53, p. 639–41, 1970.
- [14] T. E. O'Brien and A. C. D. Chaklader, *Effect of oxygen on the reaction between copper and sapphire*, J. Am. Ceram. Soc. 57, p. 329–332, 1974.
- [15] B. Gallois and C. H. P. Lupis, *Effect of oxygen on the surface tension of liquid copper*, Metall. Trans. B 12, p. 549–557, 1981.

## 6.4 Thermophysical characteristics of liquid metals and alloys at TU Graz: a status report

G. Pottlacher, K. Aziz, and A. Schmon. Thermophysical characteristics of liquid metals and alloys at TU Graz: a status report. *High Temperatures-High Pressures*, 41(5):377–394, 2012.

This publication gives a vast overview of the current facilities used by the thermophysics and metalphysics group at Graz University of Technology to determine thermophysical characteristics of liquid metals and alloys. The thermophysical properties measured with our setups are listed here as well.

### Comments:

Chapter 2.5 about electromagnetic levitation was written by me. The other chapters were written by G. Pottlacher and A. Schmon.

*High Temperatures-High Pressures*, Vol. 00, pp. 00–00  
Reprints available directly from the publisher  
Photocopying permitted by license only

©2012 Old City Publishing, Inc.  
Published by license under the OCP Science imprint,  
a member of the Old City Publishing Group

## Thermophysical characteristics of liquid metals and alloys at TU Graz: a status report<sup>†</sup>

G. POTTLAGHER\*, K. AZIZ AND A. SCHMON

*Institute of Experimental Physics, Graz University of  
Technology, Petersgasse 16, 8010 Graz, Austria*

*Received: October 10, 2011. Accepted: November 30, 2011.*

Our work group has rendered outstanding services in the field of dynamic pulse calorimetry within the last thirty years to obtain thermophysical properties of liquid metals and alloys. Today, only few more experiments on pure metals are to be expected, because almost all metallic elements, which are suitable for our pulse-heating system so far, have been investigated. These elements are: C, Co, Cu, Al, Au, Hf, In, Ir, Fe, Pb, Mo, Ni, Nb, Pd, Pt, Re, Rh, Ag, Ta, Ti, W, V, Zn, and Zr. A summary of these results is given in [1]. The investigations of different alloys will continue. To extend the range of thermophysical properties obtained in the liquid phase a levitation facility is set up right now within Austrian Science Fund (FWF) Project P 23838-N20 using parts of equipment obtained from DLR, Cologne, Germany. To access accurate data also in the solid phase we added a four point probe apparatus, and further a DSC as well as a DTA to our equipment.

*Keywords:* electromagnetic levitation; ellipsometry; four point probe; high temperatures; liquid metal; thermophysical properties; photopolarimeter, pulse heating.

### 1 INTRODUCTION

Even though the term ‘thermophysical properties’ is commonly used in scientific and metallurgical circles and some books, summaries, and articles [2–5],

---

\*Corresponding author: pottlacher@TU Graz.at

<sup>†</sup>Paper presented at 19<sup>th</sup> European Conference on Thermophysical Properties, August 28 - September 1, 2011, Thessaloniki, Greece.

no distinct definitions can be found. We define thermophysical properties as a selection of mechanical, electrical, optical, and thermal material properties of metals and alloys and the thermal dependencies thereof, with a certain relevance to industrial, scientific, and metallurgical applications.

This definition still covers a wide range of different material properties obtained by numerous different measurement techniques and approaches for the solid and the liquid phase.

With the development of tools and techniques for computer assisted calculations and simulations, knowledge of thermophysical properties at elevated temperatures up into the liquid phase became increasingly important for the metalworking industry and related fields. Advances in computer-based simulations allow modeling of casting, heat transport, solidification shrinkage, residual stress, heat treatment, welding, forging, rolling and cutting or even predictions of microstructures.

According to the list of thermophysical properties mentioned before (see Tab. 1), some properties are of greater importance for use in industrial applications while others are of more scientific interest. The most relevant

TABLE 1  
Thermophysical properties of solid and liquid metals

property	symbol	identifier
specific enthalpy	$H$	
heat of fusion	$\Delta H$	
isobaric/isochoric heat capacity	$c_p/c_v$	
density	$d$	
electrical resistivity	$\rho$	thermal, electrical, and mechanical properties
thermal conductivity	$\lambda_E$	
thermal diffusivity	$a$	
phase transition temperatures	<i>various</i>	
melting temperature (pure metals)	$T_m$	
solidus/liquidus temperature (alloys)	$T_s/T_l$	
refractive index	$n$	
extinction coefficient	$k$	optical properties
normal spectral emittance	$\varepsilon_\lambda$	
hemispherical total emittance	$\varepsilon_h$	
critical pressure	$p_c$	critical parameters
critical volume	$V_c$	
critical temperature	$T_c$	
equation-of-state (EOS) parameters	<i>various</i>	EOS
speed of sound	$c_s$	
viscosity	$\gamma$	levitation
surface tension	$\eta$	

properties to i.e. casting simulations are heat of fusion and heat capacity, and for the liquid phase electrical resistivity, density, thermal conductivity and thermal diffusivity, thermal expansion, hemispherical emittance, viscosity and surface tension [6,7]. We assume here, that the melting temperature or solidus/liquidus temperature for alloys is already known.

## 2 CURRENT FACILITIES AT TU GRAZ

### 2.1 Pulse-heating

A dynamic calorimetric pulse experiment utilizes resistive self-heating of an electric conductor - typically wire shaped samples (with diameters ranging from some hundred micrometers up to a few millimeters), rectangular shaped samples (if the material cannot be drawn into wires and test samples have to be cut), foils, or tubes - by passing a large current pulse over the sample. As a result of the materials' resistivity, the test specimen can be heated from room temperature up to melting, further through the liquid phase and finally up to the boiling point in a split second. At TU Graz properties of conducting materials can be obtained from temperatures of about 1200 K, at which most metals are in the solid state, up to about 5000 K in the liquid state. The following parts are common for all pulse heating experiments: energy storage (typically battery banks or capacitor banks) with charging unit, main switching unit (i.e. high-voltage mercury vapor ignition tubes), experimental chamber with windows for optical diagnostics and the ability to maintain a controlled ambient atmosphere. Quite often data recording equipment is placed in a shielded room (see Figure 1). Pulse heating experiments are commonly performed under inert ambient atmosphere, e.g., nitrogen or argon at ambient pressure or in

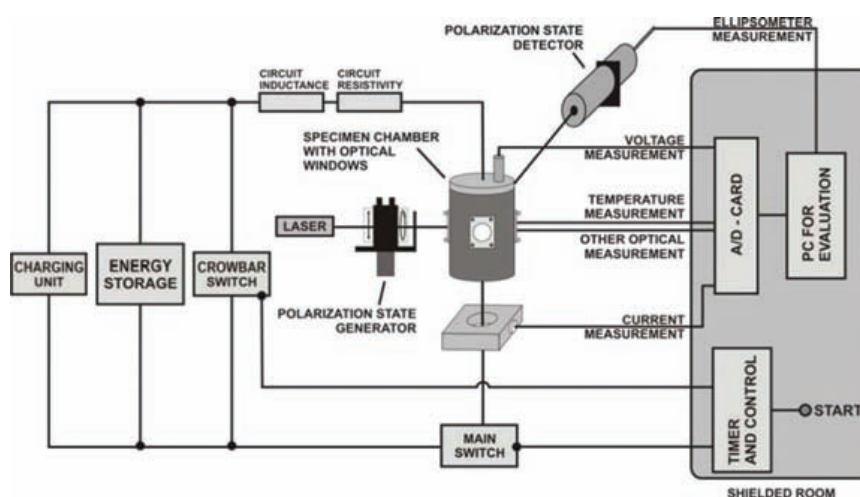


FIGURE 1  
Schematic plot of components in a typical pulse-heating experiment at TU Graz.

vacuum. At TU Graz furthermore experiments under water can be performed up to ambient pressures of 7000 bar to obtain critical point data [8].

The quantities typically recorded as a function of experimental duration,  $t$  during such an experiment at TU Graz are:

- The initial diameter  $D$  of the specimen is measured by a high accuracy laser micrometer KEYENCE LS - 7001 before the experiment.
- The current through the sample,  $I(t)$ . For monitoring the current an induction coil (PEARSON-Probe) is used.
- The voltage drop across the sample,  $U(t)$ . Two knife-edge probes pick up the voltage drop among a defined part of the wire-samples.

Optical quantities measured are:

- The surface radiation for optical thermometry,  $J(t)$ . To enable a fast and accurate temperature measurement over such a vast range, at pyrometric temperature detection based on Planck's radiation law is employed. Millisecond experiments might measure temperature not only by radiation thermometry but also sometimes by contact thermometry. For more details see chapter 2.1.1.
- The thermal expansion of the sample,  $r(t)$  which is measured by means of a coupled fast MCP/CCD-array. Within these fast pulse heating experiments, no longitudinal expansion is observed and therefore not considered in equation (3). For more details see chapter 2.1.2.
- And finally polarization information for optical properties measurements, Stokes parameter ( $S_0$ - $S_3$ ) are obtained by means of a microsecond-resolution ellipsometric device with no moving parts, called  $\mu$ s-DOAP (Division-of-Amplitude-Photopolarimeter) which is applied to measure normal spectral emissivity close to the wavelength of the pyrometer (650 nm). For more details see chapter 2.1.3.

Sound velocity measurements,  $c_s$  are not performed at TU Graz.

Based on these initially measured quantities, all thermophysical properties (with the exception of viscosity and surface tension) listed at the beginning in Table 1 can be deduced assuming that the mass,  $m$ , of the sample at room temperature is known. These data are useful as input parameters in numerical simulations and it is a major purpose of our ongoing research to provide data for simulations performed by the metal working industry. Moreover, surface tension, viscosity and density are important parameters for casting and welding processes, which are needed for simulation calculations [9]. A flow diagram showing how the thermophysical properties are related to each other is given in Figure 2.

As seen in Figure 2 from the measured data of voltage, current, surface radiance and Stokes vectors, which all are processed by digital data acquisition cards

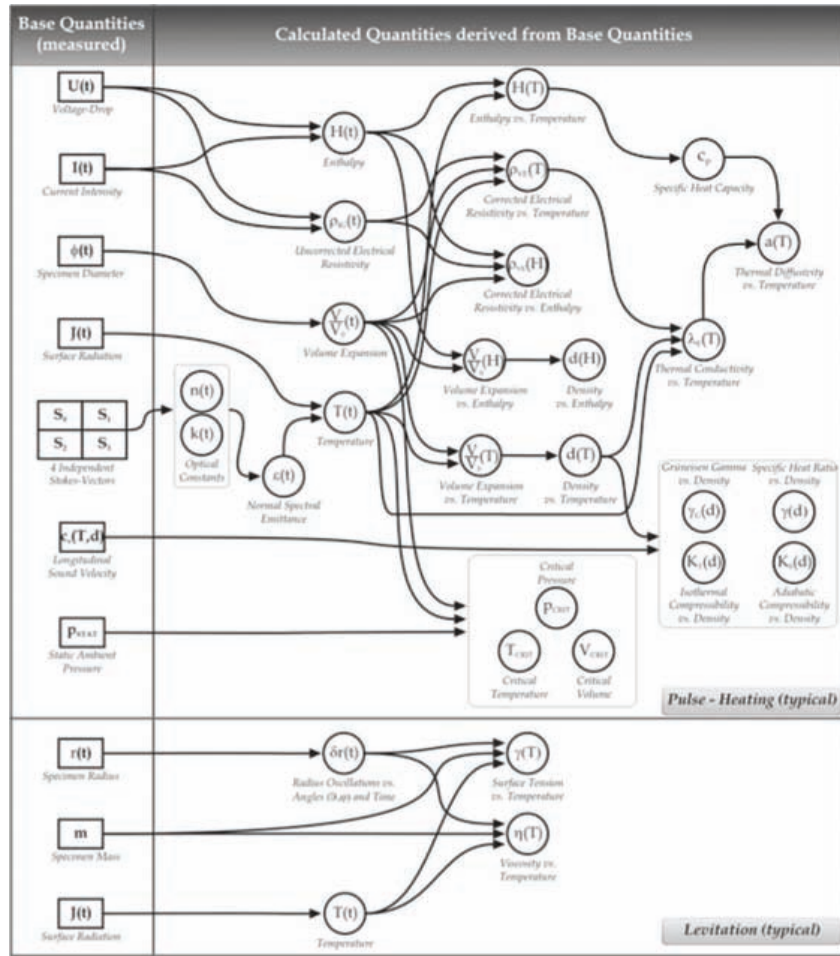


FIGURE 2  
Flow diagram to identify how the different properties are related to each other.

(IMTEC type T1012, 14 bit D/A converter) values for enthalpy, temperature, electrical resistivity, and density as a function of time are obtained. The corresponding formulas are given in Equations (1–6).

Specific enthalpy  $H$  as a function of time  $t$  is calculated using

$$H(t) = \frac{1}{m} \int_0^t I(t) U(t) dt \tag{1}$$

where  $m$  is the mass of the sample,  $I$  is the current, and  $U$  is the voltage drop. Enthalpy is calculated starting from room temperature.

Electrical resistivity corresponding to the initial geometry at room temperature  $\rho_{IG}$  is calculated using

$$\rho_{IG}(t) = \frac{U(t) \pi r_0^2}{I(t) l} \tag{2}$$

where  $r_0$  is the sample radius at room temperature and  $l$  is the length between the two knife edge probes. Due to thermal volume expansion, the sample radius changes during the heating process. This is considered by

$$\rho(T) = \rho_{IG}(T) \frac{D(T)^2}{D_0^2} \quad (3)$$

where  $D_0^2$  is the diameter at room temperature squared and  $D(T)$  is the diameter at elevated temperature (description of expansion measurement in chapter 2.1.2). Taking into account the sample expansion  $D(T)$  during heating one obtains the change of density versus temperature according to the following relation

$$d(T) = d_o \frac{D_0^2}{D(T)^2} \quad (4)$$

Where  $d(T)$  is actual density at high temperature and  $d_o$  is the density at room temperature.

Thermal conductivity  $\lambda_E$  is estimated from temperature dependent electrical resistivity  $\rho(T)$  with the help of the Wiedemann-Franz law

$$\lambda_E(T) = \frac{L T}{\rho(T)} \quad (5)$$

Where  $T$  is the temperature and  $L$  the Lorenz number ( $L = 2.45 \times 10^{-8} \text{V}^2/\text{K}^2$ ) assuming that it is invariant within the region of interest [10, 11].

Thermal diffusivity  $a$  is estimated from thermal conductivity, specific heat capacity at constant pressure  $c_p$  and temperature dependent density  $d(T)$  using again the Wiedemann-Franz law

$$a(T) = \frac{\lambda(T)}{c_p(T) \cdot d(T)} \quad (6)$$

### 2.1.1 Temperature

Temperatures are measured by means of optical radiation thermometry evaluating the thermal radiance emitted from the sample's surface. Four different pyrometers can be used, which operate depending on the material investigated, on a centre wavelength of 650 nm (FWHM 37 nm), 902 nm (FWHM 18 nm), 1570 nm (FWHM 84 nm) and 2322 nm (FWHM 450 nm) selected by interference filters. The optics of the pyrometer views an area of  $0.2 \text{ mm} \times 10 \text{ mm}$  of the pulse-heated sample surface (sample dimensions: 50 mm length, 0.5 mm diameter) with a 1:1 magnification onto the rectangular entry slit of an optical waveguide. The interference filter is in front of the entry slit of the waveguide. The light delivered by this waveguide is detected by a Si-photodiode and

amplified with a fast amplifier (bandwidth 1 MHz). The intensity signal  $J$  can be expressed as

$$J(\lambda, T) = g \sigma(\lambda) \tau(\lambda) \varepsilon_{\lambda}(\lambda, T) \frac{c_1}{\lambda^5 \left[ \exp\left(\frac{c_2}{\lambda T}\right) - 1 \right]} \quad (7)$$

with the symbols:  $g$ , geometry factor;  $\sigma$ , sensitivity of electronics and diode;  $\lambda$ , wavelength;  $\tau$ , transmission of optic and optical waveguide;  $\varepsilon_{\lambda}$ , normal spectral emissivity,  $c_1$  and  $c_2$ , first and second radiation constant; and  $T$ , temperature.

By forming ratios of the measured radiance intensity at melting  $J(T_m)$  and the measured radiance intensity  $J(T)$  at temperature  $T$ , one obtains the unknown temperature  $T$  with the melting temperature of the investigated element as the calibration point, or for alloys the arithmetic mean of the solidus- and liquidus temperatures:

$$T = \frac{c_2}{\lambda \ln \left\{ 1 + \frac{J_m(T_m) \varepsilon(\lambda, T)}{J(T) \varepsilon(\lambda, T_m)} \left[ \exp\left(\frac{c_2}{\lambda T_m}\right) - 1 \right] \right\}} \quad (8)$$

where  $\varepsilon(\lambda, T)$  is the emissivity of the liquid sample and  $\varepsilon(\lambda, T_m)$  is the emissivity at the melting temperature. There are two ways to treat the emissivity problem: If no information regarding emissivity is available, one is assuming a temperature invariant emissivity in the liquid phase, which is very often done when applying pulse heating techniques. The second, but much more difficult way is to determine normal spectral emissivity. For several elements normal spectral emissivity at 684.5 nm as a function of temperature has been measured (see chapter 2.1.3) and used to obtain true temperatures. For emissivity dependences of liquid metals, see [12].

### 2.1.2 Expansion measurement

The sample's thermal expansion during pulse-heating measurements is optically monitored by a fast CCD-camera system. Basically, a strongly magnified shadow-graph image of a small section of the specimen is focused onto a multichannel-plate (MCP) - CCD - chip combination. The MCP sets the pre-defined exposure time and the amplification, the CCD records and stores the images. For being able to record several images of the expanding sample during one single experiment the CCD-chip is masked and thus separated into an exposure- and a storage-zone. 32 or 16 or 8 out of total 576 lines can be exposed, the rest is used as storage. As shifting of exposed lines is several times faster than reading the entire chip's content, these first 32 or 16 or 8 lines are shifted to the storage area and automatically cleared. This procedure can

be repeated until completion of the storage area which can be slowly read-out after the experiment, the different results can be seen in Figure 3. The camera system has been strongly improved recently and images the radial expansion of the sample about every  $5\ \mu\text{s}$  (or  $2,5\ \mu\text{s}$ ) depending on the actual exposure time. The obtained CCD pictures can be related to the overall thermal expansion, see Figure 3. The evaluation of the wire diameter is done by calculating full-width-half-maximum (FWHM) from the intensity profiles.

This technique can solely measure radial expansion, as only a small fraction of the respective specimen is monitored. However, experiments with another camera capable of imaging the entire (but only one single picture during one experiment) specimen proofed that the samples only expand radially and do not show any longitudinal expansion above a sufficiently high heating rate, which has to be determined in pre-experiments, in the currently used set-up. To our understanding, this finding does not negate the existence of longitudinal expansion, but merely states that it can't be observed at the used time-scale due to effects like inertia of mass or extremely high heating rates. Therefore the actual sample volume only increases with the radial expansion (in 2 dimensions) which is measured by the camera system (see Figure 4) and used in the

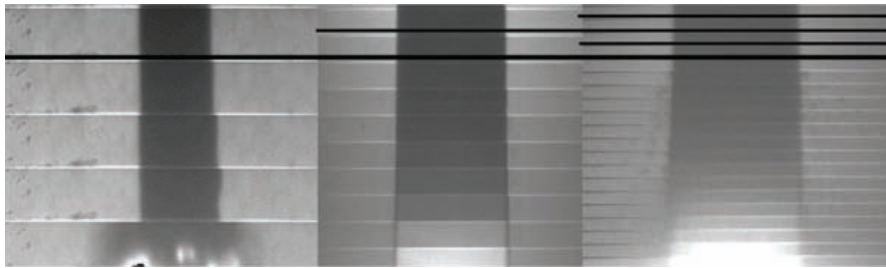


FIGURE 3  
CCD-camera pictures, time axis from top to bottom, left: 32 lines shifted, middle: 16 lines shifted, right: 8 lines shifted.

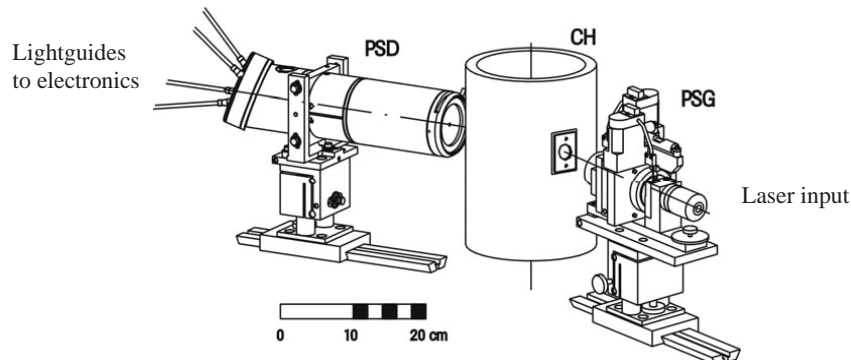


FIGURE 4  
The Division of Amplitude Photopolarimeter. PSG: polarization state generator, PSD: polarization state detector, CH: experimental chamber.

calculation of electrical resistivity in Eq. (3). A summary of techniques and the development of different systems for expansion measurements is given in [13].

### 2.1.3 Division of amplitude photopolarimeter - polarimetry:

Knowledge of emissivity and its behaviour is of great importance, especially if one is dealing with optical (pyrometrical) temperature determination by means of Planck's law of radiation. The  $\mu$ s-DOAP (Division-Of-Amplitude-Polarimeter), which is embedded in the pulse-heating setup, enables us to determine normal spectral emissivity as well as the optical constants refractive index and extinction coefficient at a wavelength of 684.5 nm as a function of temperature from melting up into the liquid state of the specimen material.

The Division of Amplitude Photopolarimeter ( $\mu$ -DOAP) [14] consists of the following components (from [15]): the source of light, the Polarization State Generator (PSG), the Polarization State Detector (PSD) as well as the electronics to record and amplify the measurement signals (Fig. 4). As source of light a laser diode capable of modulation with up to 8 MHz serves, the emitted light has a wavelength of 684.5 nm. The PSG module consists basically of a rotative mounted linear polarizer and an also rotative mounted quarter wave retarder. Each arbitrary polarization state can be generated by suitable angular position of these two components. The change of the position of the two optical components occurs with servo - motors which can be controlled by the electronics of the polarimeter by means of the DOAP software.

The PSD module is the main part of the polarimeter. In this detector the reflected light first of all is transformed into a parallel bundle by means of a pair of lenses, and split afterwards into two partial beams by a coated beam splitter. The two obtained beams are splitted again by two GLANN-THOMPSON prisms. The four resulting beams are focused on four light guides which transport the light into the shielded room, where the light is detected by four silicon photo detectors and amplified by LOCK - IN technique. The wavelength selection of 684.5 nm occurs with the interference filter behind the first lens of the PSD, this filter is used mainly to suppress the background radiation which is emitted by the hot sample surface.

From the four measured intensities  $\vec{I} = (I_0, I_1, I_2, I_3)$  the STOKES' vector of the reflected light can be calculated by means of the  $4 \times 4$  instrument matrix  $\vec{A}$ :

$$\vec{S} = \vec{A}^{-1} \cdot \vec{I} \quad (9)$$

The instrument matrix  $\vec{A}$  is received by a calibration of the DOAP. For calibration the PSG module is mounted opposite to the PSD and 36 linearly polarized as well as 18 left and right hand circular polarized states are generated. From the intensities measured in this case the instrument matrix can be determined by the use of statistical methods [16–18]. Since the laser beam is

already polarized before the entry into the PSG module the intensity of the beam after the PSG depends on the generated state of polarization. To correct this effect the intensity after the PSG module is measured by a special detector which does not change the state of polarization. The measured signals then are normalized by the signal of this detector. To verify the result of the calibration and to realize the angle of  $140^\circ$ , the laser is reflected on a prism made of BK7 glass. For a correct calibration the index of refraction as well as the extinction coefficient of the glass prism are determined within an accuracy of 0.5 %.

If the polarization state before the reflection at the sample is chosen to be +45 linear polarized and the angle of incidence is  $70^\circ$ , the ellipsometric parameters can be calculated from the STOKES's components of the reflected beam as follows:

$$\tan \Delta = -\frac{S'_3}{S'_2} \quad (10)$$

$$\tan 2\Psi = -\frac{\sqrt{S'_2 + S'_3}}{S'_1} \quad (11)$$

The normal spectral emissivity  $\varepsilon_\perp$  is obtained from the law of the conservation of energy  $R + A + T = 1$  (where R is the reflectivity, A is the absorptivity and T is the transmittance) and Kirchhoff's law for normal incidence  $\varepsilon_\perp + A_\perp$  one arrives at:

$$\varepsilon_\perp = 1 - \mathfrak{R}_\perp = \frac{4n_1n_2}{(n_1^2 + n_2^2) + k_2^2} \quad (12)$$

for the normal spectral emissivity at the laser wavelength, where  $R_\perp$  is the reflectivity of the sample for normal incidence, n is the real part of the complex index of refraction; and k is the extinction coefficient, subscript 1, 2 means first and second medium – air and sample. Eq. 12 is only valid for opaque materials, where the transmittance T is zero. For a more detailed derivation see [15].

## 2.2 DSC

A differential scanning calorimeter (DSC) is used primarily for measurements of the heat capacity of the sample in the solid phase as well as for the investigation of phase transitions. The samples are typically 5.2 mm in diameter and 0.5 mm in height, the temperature range investigated from 400 K to 1700 K. See the measuring head in Figure 5. Typical heating rates are 20 K/min, with argon as the ambient medium. We employ a DSC 404 and a STA 449 C Jupiter, both from Netzsch.

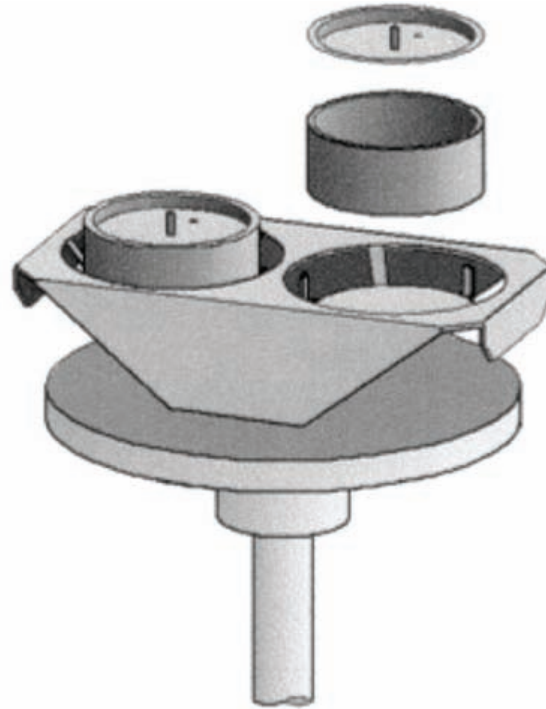


FIGURE 5  
Measuring head of the DSC with two pans.

The difference in heat flow from furnace to sample and furnace to reference material results in a difference of temperature between sample and reference material.

The temperature of the sample is measured relative to a second, inert sample with approximately the same heat capacity. One experiment consists usually of three separate runs: a scan with two empty pans, a scan with one pan containing a sapphire reference sample, and finally a scan with the sample in the same pan where the reference sample was previously.

With known specific heat capacity of the reference and known masses the specific heat capacity of the sample is calculated using

$$c_{p \text{ Probe}} = c_{p \text{ Re ferenz}} \frac{m_{\text{Re ferenz}} \Delta V_{\text{Pr obe}}}{m_{\text{Pr obe}} \Delta V_{\text{Re ferenz}}} \quad (13)$$

Where  $c_p$  is specific heat capacity,  $m$  the mass and  $\Delta V$  the measured voltage, all according to their index.

The onset temperature of the pyrometers used for pulse heating (between 1000 K and 1500 K) limits the possibility to report thermophysical properties versus temperature to the range above the pyrometer onset, which is, in fact, a strong limitation.

To overcome this limitation and to obtain temperature dependences for these quantities below the onset temperature of the pyrometers, a differential scanning calorimeter was added to our setup and incorporated into the basic measurement routines. The DSC is able to perform accurate specific heat capacity measurements in the above mentioned temperature range. The results are combined with those of the pulse-heating experiments by using the enthalpy versus temperature dependence of the DSC to expand the temperature range of the pulse-heating data. Thus, temperature dependences of all thermophysical properties can now be extended down to the DSC onset temperature of about 500 K. For more details see [19].

### 2.3 DTA

A differential thermal analysis (DTA) is used at TU Graz in the temperature range from 400 K to 1700 K to measure melting temperatures, as well as solidus and liquidus temperatures. Similar to the DSC the temperature difference between sample and an inert reference is recorded during the heating cycle. Endothermic and exothermic changes in the sample result in peaks in the measured data plotted against temperature.

See the measuring head in Figure 6. Typical heating rates are 10 K/min, with argon as the ambient medium. We employ a STA 449 C Jupiter from Netzsch. Thermogravimetric measurements and investigation of corrosion processes are also possible with this device.

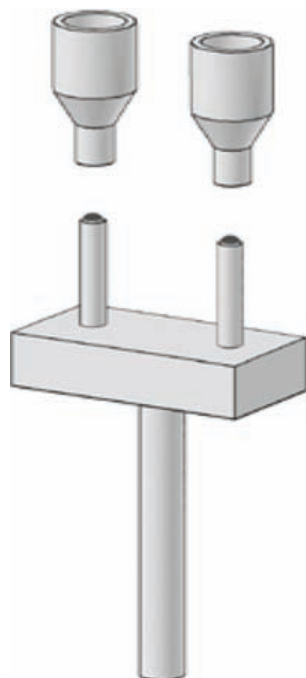


FIGURE 6  
Measuring head of the DTA with two pans.

## 2.4 4-Point-Probe

The four-point probe method is the most common way to measure a semiconductor material's resistivity, but also can be applied to all other conducting materials. Two of the probes are used to source current and the other two probes are used to measure voltage. See the schematic scetch in of the four probes in Figure 7. Using four probes eliminates measurement errors due to the probe resistance, the spreading resistance under each probe, and the contact resistance between each metal probe and the specimen material. This technique involves bringing four probes at known distance and geometry into contact with the material of unknown resistance.

Within our laboratory the four point probe is employed to measure the temperature-dependent electrical resistivity of conducting materials. Two of the electrical contacts supply the sample with a current of 300 mA, coming from a custom designed constant-current source; the second pair of contacts is used to detect the voltage drop across a certain distance of the sample. All electrical measurements are performed with the aid of measuring modules from Gantner, which can be controlled by a bus system. From these data electrical resistivity can be calculated directly by Ohm's law. Furthermore, the entire measuring system, which is housed inside a ceramic  $\text{Al}_2\text{O}_3$  tube and a second special quartz glass tube (trade mark Philips PH-300), can be operated inside a tube furnace (Heraeus, RO 4/50, maximum heating rate 14 K/min), which allows the determination of temperature-dependent resistivity from room temperature to about 1350 K, provided that the sample dimensions and its thermal expansion are known. To create and maintain a non-oxidative ambient atmosphere during the measurements, the tube with the sample holder, the four electrical contacts and two type K thermoelements for temperature

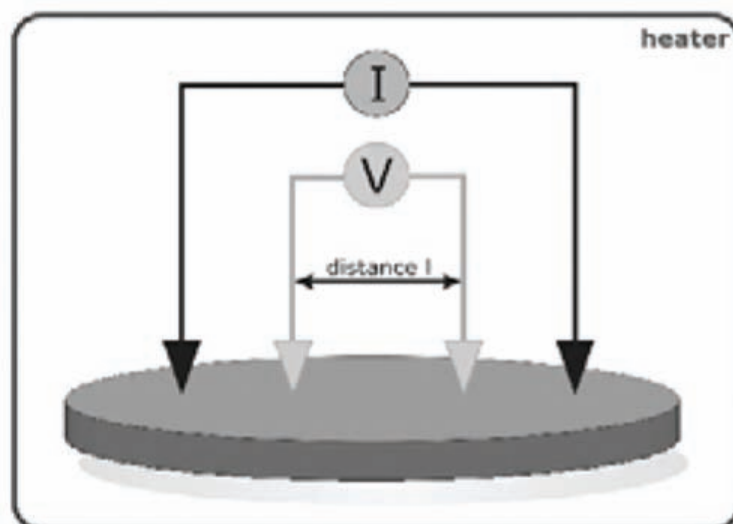


FIGURE 7  
Schematic sketch of the four point probe.

determination first are evacuated by means of a rotary vane pump and then flushed with argon during the experiment.

## 2.5 Levitation

For metallic melts electromagnetic levitation provides an elegant method of noncontact containerless measurement, eliminating most interactions between the sample and its environment. The sample, assuming a nearly spherical shape, is contained in a clean environment and can be studied over a large temperature range [20,21]. Again temperatures are measured with a pyrometer. An electromagnetic levitation device employs inhomogeneous radio-frequency electromagnetic fields to heat and position the samples. Such a field has two effects on a conducting body. First, it induces eddy currents within the material, which, due to ohmic losses heat up the sample by inductive heating, and second, it exerts a Lorentz force on the body, pushing it towards regions of lower field strength. The latter effect can be used to compensate the gravitational force.

The thermophysics and metalphysics group at TU Graz obtained from DLR Cologne several parts of experimental equipment and is recently building up a levitation device, which should deliver first results at the end of the year 2011. For generating alternating electromagnetic fields a generator (Hüttinger, type IG 5/200HY, maximum power 6 kW) with an induction coil is available. It can generate fields with a frequency up to 200 kHz. A thin copper tube will be the starting material for levitation coils.

Two optical pyrometers for measuring the sample temperature will be used (Kleiber IR - pyrometer Type 270A und Type 270B + CCD-camera). The pyrometers will be positioned on the side of the vacuum-chamber. The vacuum-pump-system includes a rotary vane pump and a turbo molecular pump. Before starting an experiment, the sample chamber must be evacuated to an absolute pressure of approximately  $10^{-6}$  mbar. After evacuation the chamber is connected to the gas supply system and filled with working gas up to pressures of 0.7 bar (Ar, He, traces of H). These process gases are used for cooling and with some restriction also for positioning of the drop inside the levitation coil. Cooling is controlled by choosing the appropriate mixture of Helium and Argon, while positioning is realized by the velocity of the gas stream. A schematic sketch of the apparatus is given in Figure 8.

The sample chamber is a 6-way cross vacuum-part made of high-grade steel with glass windows on the front and on the back, thus the droplet can be observed during the experiment. Fast cameras are needed to measure the density of the sample and the surface oscillations which then will be used to calculate the surface tension of the sample. These surface oscillations have an expected frequency in a range between 30 Hz to 70 Hz. Therefore this camera must be able to record data using a frame rate of at least 200 frames per second.

At the beginning of an experiment the sample inside the chamber is positioned on a specimen holder, which is a tube made of ceramic ( $\text{Al}_2\text{O}_3$ ). This

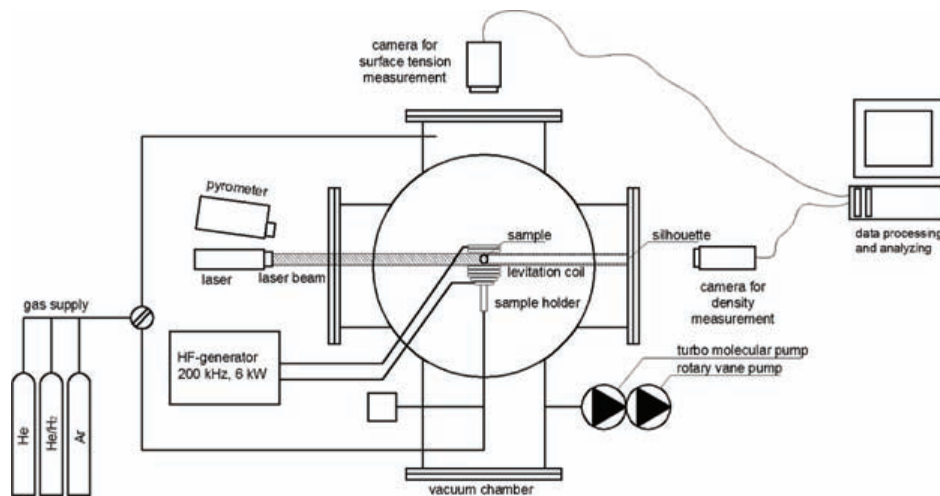


FIGURE 8  
Schematic drawing of the levitation device being established recently at TU Graz.

tube is kept moveable, as the sample holder has to be lowered when the droplet is floating because of electromagnetic forces. The  $\text{Al}_2\text{O}_3$ -tube is connected with the gas supply system and it is possible to flush the vacuum chamber with argon and helium during the experiment. This has two reasons: First, gas is needed for cooling the droplet, as this is one way to control its temperature during the experiment, besides adjusting the power of the generator. Without cooling the droplet, the material would be heated until it evaporates, assuming that the power of the generator is high enough. Second, the gas stream could be used to position the sample inside the coil. By regulating the stream of gas, the sample can be lowered or lifted. Thus the droplet can be moved a little bit upward or downward to get an optimal recording position.

### 2.5.1 Surface tension

Because of its own mass the liquid sample extends into the direction of the gravitational center. Furthermore the, so-called magnetic pressure influences the shape of the droplet. For levitation-experiments very strong magnetic fields with huge gradient towards the coil axis are necessary. Thus there are stronger magnetic forces on the bottom side of the sample than on the upper side of it. Therefore the sample will be compressed on the bottom as a consequence of the magnetic pressure. These two facts mentioned before lead to the effect, that the droplet has no ideal spherical shape. As a result not only a single, well defined frequency for the oscillation of the surface will be measured. Additionally the sample rotates during the experiment. Thus a correction term or correction function is needed to compensate all these influences.

The oscillation of a spherical liquid droplet, which has no interaction with its environment, consists generally of a superposition of several modes ( $l = 2, 3, \dots$ ). However, since the higher modes are strongly damped, only the

lowest mode ( $l = 2$ ) is observed in general. For this mode the correlation between surface tension and surface vibrations [21] is given by the following formula:

$$\omega_R^2 = 8 \cdot \frac{\gamma}{\rho \cdot R^3} = \frac{32 \cdot \pi \cdot \gamma}{3 \cdot M} \quad (14)$$

Where  $M$  is the mass of the sample,  $\omega_R^2$  describes the angular (Rayleigh) frequency in dependency of the mode  $l$  of the oscillations,  $\gamma$  is surface tension,  $\rho$  is density and  $R$  the radius of the droplet. When looking at all the effects, that influence standard levitation experiments on earth, it appears that gravity and Lorentz forces deform the sample shape. As a consequence up to five different frequencies can be measured for surface oscillations. Moreover a frequency shift because of the magnetic pressure has to be taken into account.

Cummings and Blackburn developed a correction function [22] to cope with all those influences:

$$\omega_R^2 = \bar{\Omega}_2^2 - 1,9 \cdot \omega_{tr}^2 - 0,3 \cdot \omega_{tr}^{-2} \cdot \left( \frac{g}{R} \right)^2 \quad (15)$$

$\bar{\Omega}_2^2$  is the mean value of the square of the split angular frequencies of the five observed surface oscillations of mode  $l=2$ ,  $\omega_{tr}^2$  is the mean value of translational frequencies, given by the oscillations of the samples center of mass and  $g$  is the acceleration of gravity.

As discussed above during an experiment, the surface of the liquid sample will start oscillating and these oscillations of the sample-surface are recorded with a fast camera. Data obtained are transmitted to a computer, where they are analyzed electronically in sequences of single images. A computer - program determines the following parameters depending on the Cartesian coordinate system:

- coordinates of the center of gravity  $C_m$  (x,y)
- radius  $R$  ( $0^\circ$ ) measured from the center of gravity to the border line in y-direction
- radius  $R$  ( $90^\circ$ ) measured from the center of gravity to the border line in x-direction
- the visible cross-sectional area  $A$

After evaluation of experimental data according to Eq. 14 and 15 surface tension can be calculated.

### 2.5.2 Density measurement

This experimental setup also will determine the density of levitated liquid metal and alloy samples. As it is almost impossible to determine an exact

borderline when observing a glowing droplet, it is much better to record the silhouette of the sample. For this purpose, a laser system will be integrated (see Figure 8). The laser beam crosses the sample chamber in horizontal direction and the camera records the silhouette of the sample. The images taken are analyzed and evaluated in terms of their geometrical features. The exact dimensions of the droplet have to be known for calculating the temperature dependent density, when its weight at room temperature has been determined. Quite a lot of metals are not available in the shape of wire or rectangular shaped specimens, thus we are not able to determine their density by means of pulse-heating. This levitation apparatus extends the range of thermophysical properties that can be determined for liquid metals and elements at TU Graz.

### 3 CONCLUSIONS

Within this paper the experimental equipment used by the thermophysics and metalphysics group at the Institut für Experimentalphysik at TU Graz such as electric pulse heating, DSC, DTA, 4 point probe and levitation facility is described detailed.

### ACKNOWLEDGMENTS

We are very grateful for the exchange of scientific equipment between Institut für Materialphysik im Weltraum, Deutsches Zentrum für Luft- und Raumfahrt (DLR) Linder Höhe, 51147 Köln, Germany and Institut für Experimentalphysik, TU Graz, Petersgasse 16, 8010 Graz.

Parts of this research were funded by the Austrian Science Fund (FWF): FWF Project P 23838-N20.

### REFERENCES

- [1] G. Pottlacher, High temperature thermophysical properties of 22 pure metals, Edition Keiper, Graz, ISBN No. 978-3-9502761-6-9 (2010).
- [2] A. Goldsmith, T. E. Waterman, and H. J. Hirschhorn, Handbook of Thermophysical Properties of Solid Materials, Volume I- Elements, Pergamon Press, Oxford, (1961).
- [3] G. R. Gathers, Rep. Prog. Phys. **49**, 341-396 (1986).
- [4] A. Cezairliyan, Int. J. Thermophys. Vol. **5** (2), 177-193 (1984).
- [5] R. S. Hixson and M. A. Winkler, Int. J. Thermophys. **14**, **3**, 409-416 (1993).
- [6] C. D. Brown, Dictionary of Metallurgy, John Wiley & Sons, Cichester (1998).
- [7] E. Kaschnitz and G. Pottlacher, Giesserei-Praxis, **1**, 1-6 (2002).
- [8] G. Pottlacher and H. Jäger, Journal of Non-Crystalline Solids, **205-207**, 265-269 (1996).
- [9] E. Kaschnitz and P. Supancic, Int. J. Thermophys. Vol. **26**, **4**, 957-967 (2005).
- [10] Mills K C, Monaghan B Jand Keene B J, NPL Report CMMT (A), p. 53 (1997)
- [11] G. Pottlacher, H. Hosaeus, A. Seifert, and E. Kaschnitz, Scandinavian Journal of Metallurgy, **31**, 61-168 (2002).

- [12] G. Pottlacher, K. Boboridis C. Cagran, T. Hüpf , A. Seiffter, and B. Wilthan, Normal Spectral Emissivity Near 680 nm at Melting and in the Liquid Phase for 18 Metallic Elements, to be published in the Proceedings of TEMPERATURE 2012, Los Angeles, USA
- [13] T. Hüpf, C. Cagran, G. Pottlacher, Thermal conductivity 30 Thermal expansion 18, editor Daniela D. Gaal DEStech Publications, Inc, ISBN No. 978-1-60595-015-0, 805-813 (2010).
- [14] R. M. A. Azzam, *Opt. Acta* **29**, 685-689 (1982).
- [15] A. Seiffter, F. Sachsenhofer and G. Pottlacher, *International Journal of Thermophysics* Vol. **23**, 1267-1280 (2002).
- [16] R. M. A. Azzam, E. Masetti M. Elminyawi, A. M. El-Saba, *Rev. Sci. Instrum.* **59**, 84-88 (1988).
- [17] R. M. A. Azzam, A. G. Lopez, *J. Opt. Soc. Am.* **A6**, 1513-1521 (1989).
- [18] S. Krishnan, *J. Opt. Soc. Am.*, **A9**: 1615-1622 (1992).
- [19] B. Wilthan, C. Cagran and G. Pottlacher, *Int. J. Thermophys*, Vol. **26** 1017-1029 (2005).
- [20] I. Egry, Containerless Processing for Thermophysical Property Measurements of Liquid Metals: Review and Outlook, Proceedings of 9<sup>th</sup> Workshop on Subsecond thermophysics. HTHP (2011).
- [21] J. Brillo, D. Chatain, and I. Egry, *Int. J. Mater. Res.* **100**, 53-58 (2009).
- [22] I. Egry, G. Lohöfer, G. Jacobs, *Physical review letters*, **75**, **22**, 4043-4046 (1995).

## 6.5 Investigation of liquid metallic elements and alloys by means of containerless techniques

G. Pottlacher, A. Schmon, and K. Aziz. Investigation of liquid metallic elements and alloys by means of containerless techniques. *SF2M Annual Meeting 2012*, 2012.

This publication gives an overview of container-less techniques used by the thermo-physics and metalphysics group at Graz University of Technology to determine thermophysical properties of liquid metals and alloys. The container-less techniques used by our group are an Ohmic pulse heating experiment and an electromagnetic levitation setup.

### Comments:

The chapters about electromagnetic levitation and surface tension were written by me. The other chapters were written by G. Pottlacher and A. Schmon.

## Investigation of Liquid Metallic Elements and Alloys by Means of Containerless Techniques

G. Pottlacher<sup>a</sup>, A. Schmon<sup>a</sup> and K. Aziz<sup>a</sup>

<sup>a</sup> Institute of Experimental Physics, Graz University of Technology, 8010 Graz, Austria.

### Abstract

Metallic samples have been investigated by an ohmic pulse heating technique as well as by an electromagnetic levitation technique. The main goal of these investigations was to obtain data in the liquid phase.

Pulse heating delivers thermophysical properties of electrically conducting materials far into the liquid phase. The measurements allow the calculation of specific heat capacity and the temperature dependencies of electrical resistivity, enthalpy and density of the samples in the solid and liquid phase. Further measurements of normal spectral emissivity at 684.5 nm are performed to increase the accuracy of the pyrometric temperature measurements. Thermal conductivity and thermal diffusivity as a function of temperature are estimated from resistivity data using the Wiedemann-Franz-law.

Electromagnetic levitation, as the second experimental approach used, delivers data for surface tension (this quantity is not available by means of pulse heating technique) and for density of liquid metals under investigation as a function of temperature.

### Introduction

High temperature experimentation with solid and especially liquid specimens faces numerous difficulties. Traditional static steady state techniques for the measurement of thermophysical properties are generally limited to temperatures of about 2300 K. This limitation is a result of chemical interaction of the specimens with the containers, the loss of mechanical strength, problems with heat transfer, evaporation and electrical insulation while the sample and its environment are kept for times up to hours at high temperatures.

Containerless investigation methods have been developed to avoid these difficulties and to permit the extension of the measurements to higher temperatures. These methods are on the one hand levitation techniques such as: electromagnetic levitation, aerodynamic levitation, acoustic levitation, electrostatic levitation or microgravity levitation in space as well as drop-towers. On the other hand pulse heating techniques such ohmic pulse heating and laser pulse heating also can be called containerless techniques. Other techniques for property measurements at very high temperatures, such as chemical flames, shockwaves, solar heating, fission/fusion, and high energy electron or neutron heating will not be taken into consideration here.

Properties of matter at high temperatures are useful for high-temperature technologies such as aerospace, nuclear energy and the establishment of temperature reference

points, including applications which are subjected to high temperature - high pressure conditions, as well as input data for modeling, which got very popular recently in steel working industry to simulate casting and welding processes and in jewellery industry to reduce reject due to defects.

### Measurement principles

#### Ohmic pulse heating

The ohmic pulse heating experiment performs the entire measurement within 40 – 60 microseconds. The required energy is stored in a capacitor bank of 500  $\mu\text{F}$ , charged up to 5000 – 10000 Volts. When the capacitor bank is discharged through the wire shaped sample, a current pulse of several thousand Ampere heats the sample from room temperature up to the end of the liquid phase due to ohmic heating. The heating rates applied within these investigation are  $10^8 \text{ K}\cdot\text{s}^{-1}$  and require recording equipment with quick response time. Such a short timescale enables the extension of the measurements to extremely high temperatures. Since most metals and their alloys can be produced in wire shaped form of appropriate dimensions (usually 0.5 mm diameter and 70 mm length), the pulse heating technique is found to be an experimental method of general importance for the investigation of thermophysical properties of electrically conducting solids and fluids.

The quantities which are typically recorded as a function of experimental duration throughout such an experiment in the solid and in the liquid phase are: The current through the sample, the voltage drop across the sample, the temperature by surface radiation for optical thermometry and other quantities such as thermal expansion of the sample and polarization information for optical properties measurements such as normal spectral emissivity. Based on the initially measured quantities, thermophysical properties like enthalpy, specific heat capacity, electrical resistivity, volumetric expansion, thermal conductivity and thermal diffusivity as a function of temperature can be obtained for the material under investigation up to the end of the liquid phase, assuming that the mass of the sample at room temperature is known. For more experimental details see [1], thermophysical data in the solid and in the liquid phase for 22 metallic elements can be found in [2].

#### Electromagnetic Levitation

For metallic melts, containerless processing by electromagnetic levitation is also an elegant method for non-contact measurements. Electromagnetic levitation is a

containerless technique that can be used for the study of highly reactive melts at high temperatures. The sample with a nearly spherical shape is contained in a clean environment and can be studied over a large temperature range. An electromagnetic levitator employs inhomogeneous radio-frequency electromagnetic fields to heat and levitate the sample. Such a field has two effects on a conducting, diamagnetic body. First, it induces eddy currents within the material, which, due to ohmic losses, heat up the sample by inductive heating, and second, it exerts a Lorentz force on the body, pushing it towards regions of lower field strength. The latter effect can be used to compensate the gravitational force. On earth, strong magnetic fields are needed to compensate the gravitational force [3].

The sample is levitated in a special designed high frequency coil, which is supplied by an RF - generator. The levitation coil is water-cooled. The levitated sample is placed in a vacuum chamber with glass windows for various types of optical diagnostics such as a high-speed camera to monitor the sample shape and a pyrometer for temperature measurements. Based on the initially measured quantities, thermophysical properties like density as well as surface tension can be obtained as a function of temperature for the material under investigation in the liquid phase, assuming that the mass of the sample at the beginning and at the end of the experiment is known.

## Density

Density determinations by pulse heating technique or electromagnetic levitation technique used at TU Graz both are based on thermal expansion measurements by optical imaging methods.

In the pulse heating setup thermal expansion of the specimen-wire has to be monitored within a timescale of about 60 microseconds. Recording several images in this time duration demands a purpose-built detection system. A multi-channel-plate for amplification is combined with a CCD-array (384 pixels horizontal x 576 pixels vertical) for recording and storage. To avoid time-consuming readout time the array is masked and thereby partitioned into an exposure-area and a storage-area. 16 out of 576 pixel-lines can be exposed to record an image. The remaining lines are used as fast storage to cache the information of the exposed area. For picture acquisition these 16 unmasked lines of the CCD-array are exposed (duration about 0.6  $\mu$ s), this content is shifted to the storage area and the unmasked lines are cleared. A fast succession of this procedure enables an image recording about every 5  $\mu$ s. The CCD-array is read out when the storage-area is full (36 pictures; after the experiment).

To monitor the radial thermal expansion of the wire-specimen during pulse heating the wire is backlit by a photoflash and a magnified shadowgraph image of a section of the wire is focused on the detection system. Figure 1 depicts an illustration of the storage-area read out after a pulse-heating experiment. The streaks in the

illustration represent the 16 pixel-lines of the exposure-area used for picturing.

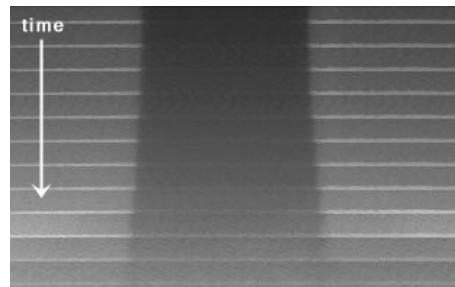


Figure 1. Illustration of the image-information of the storage-area of the CCD-array read out after a pulse-heating experiment. The observable streaks represent the recorded images (exposure time 0.6  $\mu$ s) at time intervals of about 5  $\mu$ s

The recorded images are displayed as intensity profiles and evaluated by calculating full-width-half-maximum (FWHM), depicted in Figure 2.

Experiments in the past have proven that as a result of the boundary conditions of the experimental setup no longitudinal expansion of the specimens can be observed above a sufficiently high heating rate [4]. Hence the radial expansion measurement (assuming a cylindrical shaped specimen) is used to calculate thermal volume expansion of the specimen.

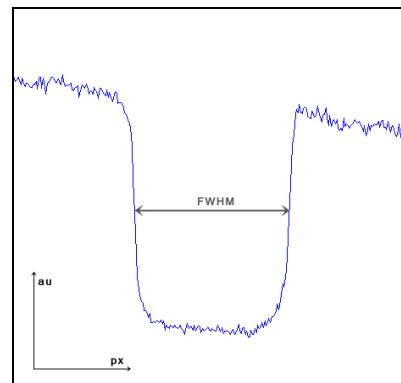


Figure 2. Intensity profile of one recorded image. Radial expansion is determined by calculating full-width-half-maximum (FWHM)

With the known density at room temperature and the relation to the pyrometric temperature measurement performed simultaneously during pulse heating the density as a function of temperature is obtained.

For thermal expansion measurements in the levitation setup a high-speed CCD-camera (1024 x 1024 pixels, frame rate of 120 fps) is used. Requirement for recording is an unobstructed line of vision on the sample from the horizontal sight, provided by an appropriate design of the

levitation coil. The lifted and heated sample is backlit by a LED-panel (100 W at about 520 nm), equipped with a diffuser to obtain a homogeneous background illumination. A shadowgraph image is recorded by the CCD-camera (Figure 3). An interference filter removes contributions due to the thermal self-radiation of the sample and improves the contrast of the shadowgraph images. The images are evaluated by using edge detection algorithms calculating the spatial derivation combined with a threshold as criterion of assignment

The volume of the sample finally is calculated by averaging several 1000 recorded frames and with the known mass of the sample, density is obtained. To obtain temperature-dependent densities, temperature again is measured using pyrometers with the assumption of a constant normal spectral emissivity in the liquid phase using the melting plateau as the reference point.

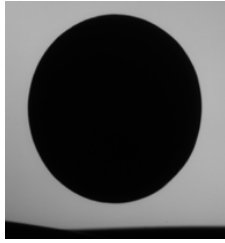


Figure 3. Shadowgraph image of a levitated steel sample

## Surface tension

Within pulse heating experiments it isn't possible to obtain data for surface tension, but electromagnetic levitation is an elegant method for containerless investigation of surface tension of liquid metals. During levitation surface oscillations occur due to surface tension as a restoring force. The deformation of the sample's shape as a function of time can be described by the spherical harmonics  $Y_l^m$ . So the Radius  $R(\vartheta, \varphi, t)$  can be written mathematically as the sum over the corresponding spherical harmonics [5]:

$$R(\vartheta, \varphi, t) = \sum_l \sum_{m=-l}^{m=l} a_{l,m}(t) \cdot Y_l^m(\vartheta, \varphi) \quad (1)$$

where  $a_{l,m}$  is the time dependence amplitude of disturbance and  $Y_l^m$  the real spherical harmonics defined by the Legendre polynomials  $P_l^m(\cos \vartheta)$  [6]:

$$Y_l^m(\vartheta, \varphi) = P_l^m(\cos \vartheta) \cos(m\varphi) \quad \text{for } m \geq 0 \quad (2a)$$

$$Y_l^m(\vartheta, \varphi) = P_l^{-m}(\cos \vartheta) \cos(-m\varphi) \quad \text{for } m < 0 \quad (2b)$$

The oscillation mode with the index  $l=0$  corresponds to an expansion and contraction of the sample a so called breathing-mode. As we assume to deal with non-compressible fluids, practically no deformation with  $l=0$  will occur.

Also for  $l=1$  practically no deformation occurs if the amplitudes are small. Only translation of the sphere will be observed.

The interesting oscillation modes are for  $l=2$  (Figure 4).

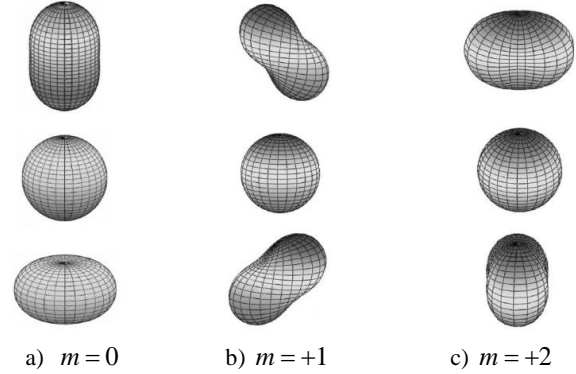


Figure 4. Deformation of the levitated drop for oscillation modes with  $l=2$  and a)  $m=0$ , b)  $m=+1$ , c)  $m=+2$ . Figure plotted according to [5, 7]

Oscillation modes with  $l \geq 3$  deliver small amplitudes and are neglected here.

As surface tension is the restoring force and therefore the origin of these oscillations, one can assume the existence of a model describing the relation between surface tension and surface oscillation. As a matter of fact Lord Rayleigh postulated a formula in 1879 [8] relating surface tension  $\gamma$  to surface oscillation frequencies  $\omega_{l,m}$  for non-rotating spherical samples:

$$\omega_{l,m}^2 = l \cdot (l+2) \cdot (l-1) \cdot \frac{\gamma}{M} \quad (3)$$

where  $l$  and  $m$  are the indices of the spherical harmonics and  $M$  is the mass of the sample. The frequencies do not depend on the index  $m$  and thus are degenerated for non-rotating samples in a symmetric force field, causing a spherical equilibrium shape.

The frequency corresponding to  $l=2$  is called Rayleigh frequency and is five-fold degenerated:

$$\omega_R^2 = \frac{32\pi}{3} \frac{\gamma}{M} \quad (4)$$

On earth different forces are acting on the liquid sample, leading to an aspheric equilibrium shape and a rotating sample. Hence the degeneracy of surface oscillations split up into maximum  $(2l+1)$  frequencies.

In Figure 4 the geometry of the oscillation mode  $l=2$  is shown. As mentioned before, the actual shape is described by the sum over the corresponding spherical harmonics (Equation 1) and in consequence given by the superposition of all oscillation modes. Figure 5 depicts typical images taken by the electromagnetic levitation setup at Graz University of Technology when investigating a steel sample. These pictures have been taken from a horizontal sight by means of a high-speed CCD-camera (Fa. Basler, Germany) with a frame rate of 120 fps. For more experimental details see [1].

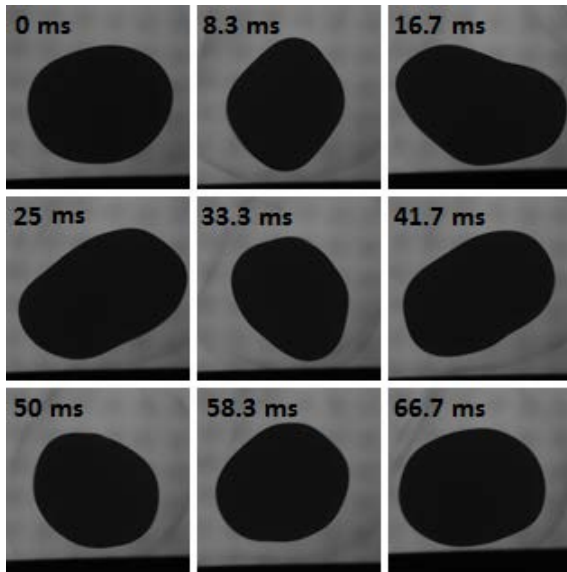


Figure 5. Images of liquid steel taken by a high-speed vision system with a frame rate of 120 fps

By image processing algorithms the center of mass as well as the shape of the observed samples is determined. After applying a Fast Fourier Transformation on the computed data, the translation and surface oscillation frequencies of the sample is received.

First results for the oscillation frequencies of a liquid steel sample are presented in Figure 6. At the frequency of 6 Hz a peak corresponding to the translation modes is observed, whereas the oscillation modes with deliver peaks in the range of 35 Hz to 55 Hz.

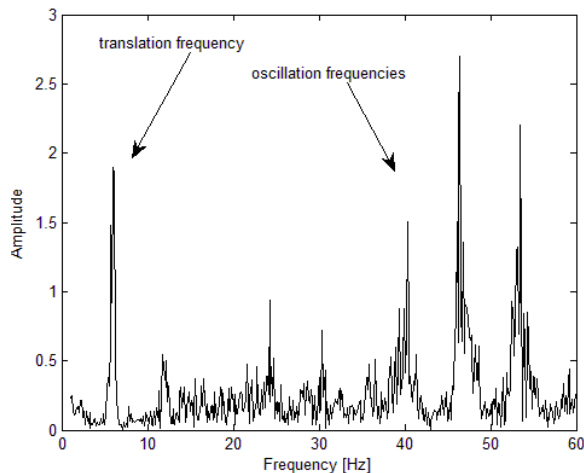


Figure 6. Translation frequency and oscillation frequencies of a steel sample

As the levitation apparatus at Graz University of Technology still is in the stage of assembling, no final results for density and surface tension as a function of time of the investigated steel sample will be presented here.

## Acknowledgments

We are very grateful for the exchange of scientific equipment between Institut für Materialphysik im Weltraum, Deutsches Zentrum für Luft- und Raumfahrt (DLR) Linder Höhe, 51147 Köln, Germany and Institut für Experimentalphysik, TU Graz, Petersgasse 16, 8010 Graz.

Parts of this research were funded by the Austrian Science Fund (FWF): FWF Project P 23838-N20.

## References

- [1] G. Pottlacher, K. Aziz and A. Schmon, Thermophysical characteristics of liquid metals and alloys at TU Graz – a status report. Accepted in *High Temperatures-High Pressures*, 2012.
- [2] G. Pottlacher, High temperature thermophysical properties of 22 pure metals, *Edition Keiper, Graz*, ISBN No. 978-3-9502761-6-9, 2010.
- [3] I. Egry, G. Lohöfer and G. Jacobs, *Phys. Rev. Letters* **75**, 4043, 1995.
- [4] C. Cagran, T. Hüpf, B. Wilthan and G. Pottlacher, Selected thermophysical properties of Hf-3%Zr from 2200 K to 3500 K obtained by a fast pulse-heating technique, *High Temperatures-High Pressures*, Vol. 37, pp. 205-219, 2008.
- [5] J. Brillo, G. Lohöfer, F. Schmidt-Hohagen, S. Schneider and I. Egry, Thermophysical property measurements of liquid metals by electromagnetic levitation, *Int. J. Materials and Product Technology*, Vol. 26, Nos. 3/4, 2006.
- [6] I. N. Bronstein and K. A. Semendjajew, *Taschenbuch der Mathematik*, Wissenschaftlicher Verlag Harri Deutsch GmbH, Frankfurt am Main, ISBN 978-3-8171-2007-9, 2008.
- [7] H. Fujii, T. Matsumoto and K. Nogi, *Analysis of surface oscillation of droplet under microgravity for the determination of its surface tension*, *Acta Materialia*, Vol. 48, Issue 11, pp. 2933-2939, 2000.
- [8] Lord Rayleigh, On the capillary phenomena of jets, *Proceedings of the Royal Society of London*, Vol. 29, pp.71-97, 1879.

# Bibliography

- [1] K. Aziz, A. Schmon, E. Kaschnitz, J. Rattenberger, and G. Pottlacher. Measurement of Surface Tension of Cu-5Sn by an Oscillating Drop. *International Journal of Thermophysics*, 37(2), 2016.
- [2] K. Aziz, A. Schmon, and G. Pottlacher. Measurement of surface tension of liquid nickel by the oscillating drop technique. *High Temperatures-High Pressures*, 44:475–481, 2015.
- [3] K. Aziz, A. Schmon, and G. Pottlacher. Measurement of surface tension of liquid copper by means of electromagnetic levitation. *High Temperatures-High Pressures*, 43:193–200, 2014.
- [4] G. Pottlacher, K. Aziz, and A. Schmon. Thermophysical characteristics of liquid metals and alloys at TU Graz: a status report. *High Temperatures-High Pressures*, 41(5):377–394, 2012.
- [5] G. Pottlacher, A. Schmon, and K. Aziz. Investigation of Liquid Metallic Elements and Alloys by Means of Containerless Techniques. *SF2M Annual Meeting 2012*, 2012.
- [6] W. D. Kingery and M. Humenik Jr. Surface tension at elevated temperatures. I. Furnace and method for use of the sessile drop method; surface tension of silicon, iron and nickel. *The Journal of Physical Chemistry*, 57(3):359–363, 1953.
- [7] I. Egry, E. Ricci, R. Novakovic, and S. Ozawa. Surface tension of liquid metals and alloys - recent developments. *Advances in colloid and interface science*, 159(2):198–212, 2010.
- [8] J. M. Andreas, E. A. Hauser, and W. B. Tucker. Boundary tension by pendant drops. *The Journal of Physical Chemistry*, 42(8):1001–1019, 1938.
- [9] C. E. Stauffer. The measurement of surface tension by the pendant drop technique. *The journal of physical chemistry*, 69(6):1933–1938, 1965.
- [10] B. Song and J. Springer. Determination of interfacial tension from the profile of a pendant drop using computer-aided image processing: 1. theoretical. *Journal of colloid and interface science*, 184(1):64–76, 1996.

- [11] B. Song and J. Springer. Determination of interfacial tension from the profile of a pendant drop using computer-aided image processing: 2. experimental. *Journal of colloid and interface science*, 184(1):77–91, 1996.
- [12] F. Bashforth and J. C. Adams. *An attempt to test the theories of capillary action: by comparing the theoretical and measured forms of drops of fluid*. University Press, 1883.
- [13] N. Sobczak, R. Nowak, W. Radziwill, J. Budzioch, and A. Glenz. Experimental complex for investigations of high temperature capillarity phenomena. *Materials Science and Engineering: A*, 495(1):43–49, 2008.
- [14] R. Nowak, T. Lanata, N. Sobczak, E. Ricci, D. Giuranno, R. Novakovic, D. Holland-Moritz, and I. Egry. Surface tension of  $\gamma$ -TiAl-based alloys. *Journal of materials science*, 45(8):1993–2001, 2010.
- [15] I. j. N. Bronštejn and K. A. Semendjaev. *Handbook of mathematics*. Springer, 2013.
- [16] Lord Rayleigh. On the capillary phenomena of jets. *Proceedings of the Royal Society of London*, 29(196-199):71–97, 1879.
- [17] D. Cummings and D. Blackburn. Oscillations of magnetically levitated aspherical droplets. *Journal of Fluid Mechanics*, 224:395–416, 1991.
- [18] A. Schmon, K. Aziz, and G. Pottlacher. Density determination of liquid copper and liquid nickel by means of fast resistive pulse heating and electromagnetic levitation. *Metallurgical and Materials Transactions A*, 46(6):2674–2679, 2015.
- [19] I. Egry, H. Giffard, and S. Schneider. The oscillating drop technique revisited. *Measurement science and technology*, 16(2):426, 2005.
- [20] Metrodata GmbH. *GUM Workbench – User Manual for Version 1.3, 2.3 and 2.4*. Metrodata GmbH, 2011.
- [21] BIPM/ISO. *Evaluation of measurement data – Guide to the expression of uncertainty in measurement*. JCGM - Joint Committee for Guides in Metrology, 2008.
- [22] D. R. Lide. *CRC Handbook of Chemistry and Physics*. CRC Press, 2004.
- [23] J. Lee and D. M. Matson. Prediction of Mass Evaporation of Fe<sub>50</sub>Co<sub>50</sub> During Measurements of Thermophysical Properties Using an Electrostatic Levitator. *Int J Thermophys*, 35(9-10):1697–1704, Jul 2014.
- [24] C. B. Alcock, V. P. Itkin, and M. K. Horrigan. Vapour pressure equations for the metallic elements: 298–2500 K. *Canadian Metallurgical Quarterly*, 23(3):309–313, 1984.

- [25] A. Seiffter, F. Sachsenhofer, S. Krishnan, and G. Pottlacher. Microsecond laser polarimetry for emissivity measurements on liquid metals at high temperatures - application to niobium. *International journal of thermophysics*, 22(5):1537–1547, 2001.
- [26] A. Seiffter, F. Sachsenhofer, and G. Pottlacher. A fast laser polarimeter improving a microsecond pulse heating system. *International journal of thermophysics*, 23(5):1267–1280, 2002.
- [27] C. Cagran, C. Brunner, A. Seiffter, and G. Pottlacher. Liquid-phase behaviour of normal spectral emissivity at 684.5 nm of some selected metals. *High Temperatures-High Pressures*, 34(6):669–679, 2002.
- [28] C. Cagran and G. Pottlacher. Normal spectral emissivity of liquid copper and liquid silver at 684.5 nm. *Temperature: Its Measurement and Control in Science and Industry*, 7:765–770, 2003.
- [29] C. Cagran, B. Wilthan, and G. Pottlacher. Normal spectral emissivities (at 684.5 nm) of liquid gold, rhenium, titanium and vanadium. *Tempmeko*, pages 1313–1318, 2004.
- [30] Achim Seiffter. *Bestimmung des normalen spektralen Emissionskoeffizienten von flüssigen pulsgelheizten Metallen mittels eines schnellen Photopolarimeters*. PhD thesis, Graz University of Technology, Mai 2001.

# List of Figures

1.1	An illustration of a sessile drop, a pendant drop, and a large drop . . .	3
1.2	An illustration of the maximum bubble pressure technique . . . . .	4
2.1	The electromagnetic levitation setup at TU Graz . . . . .	9
2.2	An illustration of an electromagnetic levitation setup . . . . .	10
2.3	A sketch of the levitation coil, the AC and eddy currents, and the mag- netic field lines . . . . .	11
2.4	Fabrication drawing of the levitation coil used . . . . .	12
2.5	Levitation Coil, sample holder and specimen . . . . .	15
2.6	Pictures of a levitating nickel specimen taken with a high-speed camera (600 fps) . . . . .	18
2.7	Spectrum of the oscillation frequencies with $l = 2$ for aluminium ob- tained by the Fourier transform of $R_x$ and $R_y$ . . . . .	21
2.8	Oscillation modes with $l = 1$ and $m = 0$ . . . . .	21
2.9	Oscillation modes with $l = 2$ and (a) $m = 0$ , (b) $m = 1$ , (c) $m = 2$ . . . .	22
2.10	Fourier transform of $R^-$ and $R^+$ . . . . .	23
4.1	Vapor pressure of copper, tin, zinc . . . . .	30
4.2	Spectrum of the oscillation frequencies with $l = 2$ for aluminium ob- tained by the Fourier transform of the area $A$ . . . . .	31
4.3	Distribution of the chemical composition of copper and tin as a func- tion of radius inside a sample . . . . .	32
4.4	Different evaluation methods for nickel . . . . .	33
4.5	Different evaluation methods for nickel (relative) . . . . .	34
4.6	Different evaluation methods for Cu-5Sn . . . . .	35
4.7	Different evaluation methods for Cu-5Sn (relative) . . . . .	35
4.8	Different evaluation methods for aluminium . . . . .	36
4.9	Different evaluation methods for aluminium (relative) . . . . .	36
4.10	Surface tension of nickel as a function of temperature . . . . .	37
4.11	Surface tension of nickel compared to literature values . . . . .	38
5.1	An Illustration of a DOAP . . . . .	40

# List of Tables

2.1	The purity of specimens measured in this work. . . . .	13
2.2	Inert gases used to provide a clean environment. . . . .	14
2.3	Specifications of the <b>PYROMETER</b> <i>IMPAC IGA 6 ADVANCED</i> . . . . .	16
2.4	Specifications of the <b>HIGH-SPEED CAMERA</b> <i>Mikrotron EoSens<sup>®</sup> CL</i> . . .	17
2.5	Specifications of the <b>CAMERA LENS</b> <i>AF Micro-Nikkor ED 200 mm f/4 D IF</i> . 17	
2.6	Specifications of the <b>FRAMEGRABBER</b> <i>Matrox Radient eCL</i> . . . . .	17
3.1	Uncertainty contribution of $\nu_{1,m}$ , $\nu_{2,m}$ , $M$ , and $\rho$ to the uncertainty of surface tension for Cu–5Sn at the temperature of 1388 K. . . . .	26
3.2	Uncertainty contribution of $\nu_{1,m}$ , $\nu_{2,m}$ , $M$ , and $\rho$ to the uncertainty of surface tension for nickel at the temperature of 1758 K. . . . .	27
3.3	The surface tension of nickel at the temperature of 1758 K for different density values and its variance from the correct value. . . . .	27
3.4	Relative uncertainty $\frac{\Delta\gamma}{\gamma}$ for the surface tension of copper, nickel, aluminium, and Cu–5Sn due to inaccurate temperature measurement ( $\Delta T = 10$ K). . . . .	28

## Acknowledgements

First, I would like to thank my doctoral advisor Prof. Gernot Pottlacher of the Institute of Experimental Physics for his guidance and the opportunity to write this thesis in his workgroup *Thermophysics and Metalphysics*. He always provided a pleasant working environment and offered me his support whenever I asked for it.

In addition, I would like to thank my colleagues for all scientific discussions and interesting conversations about everything and anything. I always felt to be in best company. A special thanks goes to my coworker Alexander, who started his PhD at the same time as myself. Besides the enriching scientific debates, my work would have been less enjoyable without him.

I would like to express my gratitude to the colleagues Dr. Georg Lohöfer and Dr. Jürgen Brillo from the Institute of Materials Physics in Space at the German Aerospace Center (DLR) for all the exciting and stimulating discussions. A special thanks goes to Prof. Ivan Egry for the exchange of scientific equipment between DLR and TU Graz.

I want to thank Martina not only for proof-reading of my thesis, but also for her help with whatever I needed.

Last but not least, this thesis would not have been possible without the help of my parents and family in so many ways. At this point, I would like to use the opportunity to thank them. This thesis is dedicated to them.

This work was financially supported by Austrian Science Fund (FWF), Vienna, Austria under Contract No. P23838-N20.

Graz, 16.02.2016

Kirmanj AZIZ